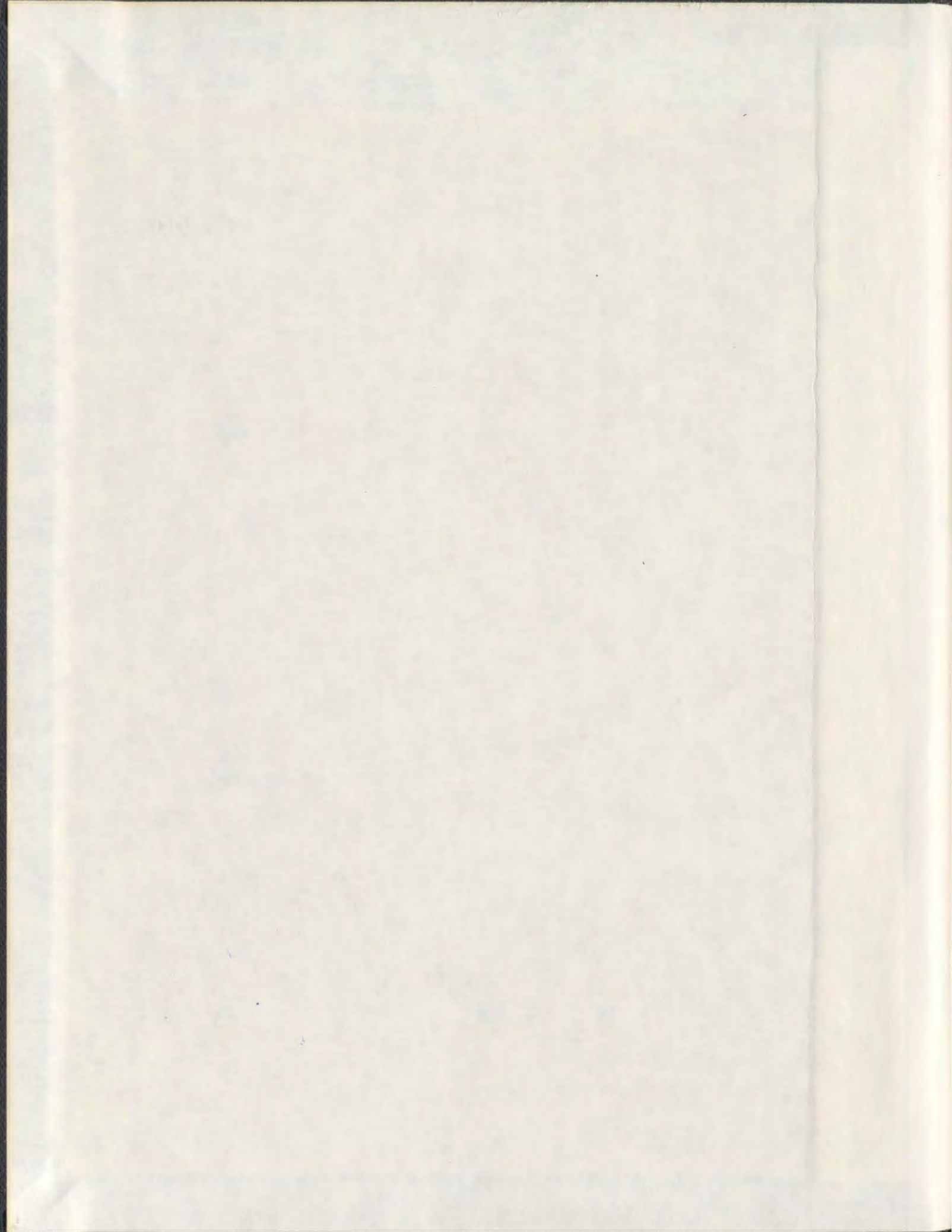


LOCATING HYDRATE DEPOSITION IN MULTIPHASE  
COMPRESSED NATURAL GAS FLOW LINES USING  
COMPUTATIONAL FLUID DYNAMICS TECHNIQUES

ESAM ISMAEEL JASSIM



001311





**Locating Hydrate Deposition in Multiphase Compressed Natural Gas  
Flow Lines Using Computational Fluid Dynamics Techniques**

By

Esam Ismaeel Jassim  
(B.Sc., M.Sc.)

Submitted to the School of Graduate Studies in partial  
fulfillment of the requirements for the degree of Doctoral  
Philosophy

Faculty of Engineering and Applied Science  
Memorial University of Newfoundland  
St. John's, NL  
Canada, A1B 3X5  
2008

## ABSTRACT

The main aim of this research is to develop a comprehensive flow model capable of predicting the nucleation process, the growth rate, and the deposition potential of hydrate particles. The model is developed for applications in two-phase fluid flow through flow lines with flow restriction geometries using Computational Fluid Dynamic (CFD) approach.

The primary objective of the research is to predict the risk hazards involved in the marine transportation of compressed natural gas. However the proposed model can be equally used for other applications including production and transportation of natural gas in any high pressure flow line.

The influence of the major parameters affecting the hydrate formation rate and deposition are addressed. The background knowledge concerning the development of the proposed model has been reviewed through literature survey. From the existing literature, it was found that the fundamental concepts related to the nucleation phenomena and growth theory are well established and ready to be integrated. A number of comprehensive models have also been successfully developed to predict hydrate formation and accumulation. These models however were not specifically developed to predict the most probable location for hydrate deposition under conditions where natural gas flows through restrictions in pipeline systems.

The proposed model employs the following three main components to approach the problem: (a) computational fluid dynamics (CFD) technique is used to configure the flow field; (b) nucleation and growth are incorporated in the simulation to predict the

incipient hydrate particles size and growth rate; and finally(c) the novel approach of the migration and deposition of the particle is used to determine how particles deposit and adhere to the flow conduit wall. These components are integrated in the proposed model to locate the hydrate deposition in flow lines. Experimental tests are also established to assess the agreement of the proposed model. Further, the influence of pipe size and flow rate on the distance of deposition is also studied.

The results predicted by the model simulation show that the distance of the deposition decreases as the particle size increases. However, after certain size of particle, there is no effect on the distance of deposition. Such size has been called “deposition critical size”. This behaviour can be returned to the fact that small particles are influenced by the main fluid velocity but for relatively large particles such effect diminishes as a result of the high particle inertia.

The experimental tests that performed in the Centre for Marine Compressed natural Gas Inc. are shown to be in good agreement with the model prediction in term of the following criteria: 1) Formation of hydrate particles are observed to be polydisperse since different sizes of particles are formed. This observation is matched with the analytical correlation of the Particle Growth and Distribution proposed in the study; 2) Studying the influence of flow Reynolds number and pipe diameter, the deposition distance is found to be linearly responded to the Reynolds number and pipe size.

## ACKNOWLEDGMENTS

This work would not have been possible without the enormous help from many people. I would like to thank:

Dr. Majid A. Abdi and Dr. Yuri Muzychka for their inspiration, advice and never-ending support during my research work. The members of my committee – Dr. Kelly Hawboldt and Dr. Faisal Khan.

The financial support of this work – The Centre for Marine Compressed Natural Gas (CMCNG) Inc., Atlantic Innovation Fund (AIF) through Atlantic Canada Opportunities Agency (ACOA), and Natural Racecourses Canada (NRCan).

The Centre for Marine Compressed Natural Gas (CMCNG) Inc. for helping me with setting up the flow loop experiments of hydrate. The Fluid Lab. in Faculty of Engineering, Memorial University of Newfoundland for their permitting to use the Cooling Chamber for my preliminary tests.

My wife, Sons and lovely daughter for being extremely patient and believing in me through the past 3 years. Words cannot express what they have gone through and their love for me.

My family in Iraq for cheering me up all the time, and being a constant support despite the hard life they live in.

I would also like to thank the faculty members and students of Faculty of Engineering at MUN for all the help and a pleasant working environment.

## TABLE OF CONTENT

<b>ABSTRACT</b> .....	i
<b>ACKNOWLEDGMENTS</b> .....	iii
<b>TABLE OF CONTENTS</b> .....	iv
<b>LIST OF TABLES</b> .....	vii
<b>LIST OF FIGURES</b> .....	viii
<b>NOMENCLATURE</b> .....	x
<b>1. INTRODUCTION</b> .....	1
1.1 General.....	1
1.2 What is Clathrate Hydrate.....	2
1.3 Why Hydrates are of Interest.....	5
1.3.1 Hydrate as an Energy sources.....	7
1.3.2 Storage and Transportation .....	8
1.3.3 Safety.....	8
1.3.4 Pipeline Plugging.....	8
1.4 Objectives of Proposed Research.....	12
1.5 Outline of Thesis.....	13
<b>2. LITRUTURE SURVEY</b> .....	15
2.1 General.....	15
2.2 Hydrate Structures.....	15
2.3 Hydrate Properties.....	17
2.4 Hydrate Formation.....	19
2.4.1 Induction Time.....	19
2.4.2 Growth Rate.....	22
2.5 Preventing Hydrate Formation.....	28
2.6 How This Work Helps the Hydrate Community .....	30
<b>3. MATHEMATICAL MODELLING OF GAS SOLID FLOW</b> .....	32
3.1 Equation of Motion.....	32
3.1.1 Continuum Equation for Conservation of Mass.....	33
3.1.2 Disperse Phase Number Continuity.....	33
3.1.3 Continuum Equation for Conservation of Momentum.....	34
3.1.4 Disperse Phase Momentum Equation.....	35
3.1.5 Velocity Relaxation Time.....	36
3.1.6 Equation for Conservation of Energy.....	36
3.1.7 Temperature Relaxation Time.....	38
3.2 Technique of Solving Transport Equations (CFD).....	40

<b>4. HYDRATE NUCLEATION, GROWTH AND DISTRIBUTION.....</b>	<b>42</b>
4.1 Review.....	42
4.2 Theory.....	44
4.2.1 Mass Transfer.....	44
4.2.2 Model of Homogenous Nucleation and Droplet Growth (Model I)	45
4.2.3 Model of Reaction Kinetics combined with Mass Transfer (Model II)	47
4.3 Size Distribution Model.....	49
4.3.1 Solution of Mass Transfer Model.....	50
4.3.2 Solution of Model of Reaction Kinetics with Mass Transfer.....	51
4.4 Analysis and Discussion.....	52
4.4.1 Growth of particle radii (Model I).....	52
4.4.2 Growth of particle radii (Model II).....	55
4.4.3 Effect of Saturation.....	57
4.4.4 Effect of Relative Velocity.....	59
4.4.5 Size Distribution.....	63
4.5 Conclusion.....	66
<b>5. FORCES APPLIED TO A SINGLE PARTICLE .....</b>	<b>68</b>
5.1 Pressure Gradient Force .....	69
5.2 Buoyancy Force.....	70
5.3 Drag Force.....	70
5.3.1 Slip Correction Factor.....	72
5.4 Gravitational Settling .....	73
5.4.1 Low Reynolds Number $Re_p < 1$ .....	73
5.4.2 Other $Re_p > 1$ .....	74
5.5 Lift Force .....	76
5.6 Adhesive Force .....	80
5.7 Model of Adhesion.....	83
5.7.1 Particle-Wall Attraction.....	83
5.7.2 Particle-Particle Attraction.....	85
5.8 Conclusion.....	87
<b>6. DEPOSITION MECHANISM.....</b>	<b>89</b>
6.1 Brownian Motion .....	89
6.2 Impaction Effect.....	92
6.3 Correlations of the Deposition Velocity .....	93
6.3.1 Model of Wells and Friendlander.....	95
6.3.2 Wood Model.....	97
6.3.3 The model of Fan and Ahmadi.....	98
6.3.4 Comparison of models.....	98
6.4 Number of Deposited Particles .....	101
6.5 Sublayer Region .....	103
6.6 Behaviour of particles in near-wall regime .....	106
6.7 Particle-Wall Distance.....	110
6.8 Bouncing Model.....	114

6.9 Summary.....	117
6.10 Conclusion.....	119
<b>7. EXPERIMENT SETUP</b> .....	120
7.1 Preliminary Experiment Setup .....	120
7.1.1 Apparatus and Procedures.....	120
7.2 Improved Experiment Apparatus .....	124
7.2.1 Flow Circuit.....	124
<b>8. MODELLING OF HYDRATE DEPOSITION LOCATION FOR SINGLE PARTICLE</b> .....	129
<b>A. WATER-AIR SYSTEM</b> .....	129
8.1 Flow Simulation-CFD results .....	129
8.2 Nucleation and Growth of Ice Particles .....	134
8.3 Calculating the distance of the deposition .....	138
8.3.1 Trajectory of a single particle ( $d_p < \delta$ ).....	139
8.3.2 Trajectory of single particle ( $d_p > \delta$ ) .....	140
8.4 Bouncing distance .....	143
8.5 Experimental results and preliminary model validation .....	144
8.6 Uncertainty analysis of saturated air experiments .....	149
<b>B. PROPANE-HYDRATE</b> .....	153
8.7 Experiment apparatus.....	153
8.7.1 Test procedure .....	153
8.7.2 Observations.....	157
8.8 CFD and simulation- results.....	157
8.9 Nucleation and growth of hydrate particles.....	159
8.10 The deposition distance.....	162
8.11 Uncertainty Analysis.....	163
<b>9. CONCLUSIONS AND RECOMMENDATIONS</b> .....	165
<b>REFERENCES</b> .....	169
<b>APPENDICIES</b> .....	207

## List of Tables

Table 6.1	Experimental Results of Yung <i>et al</i> (1989)
Table 8.1	Boundary Conditions for saturated air simulation
Table 8.2	Parameters used in calculating $\beta_1$ and critical radius for ice
Table 8.3a	Percent error of deposition distance observed in experimental tests and predicted by simulation for $Re=32\ 800$ (Figure 8.11)
Table 8.3b	Percent error of deposition distance observed in experimental tests and predicted by simulation for 1/4" pipe (Figure 8.12)
Table 8.4	Ice and water comparison of the deposition distance observed in the tests and predicted by the simulation for $Re= 32\ 800$
Table 8.5	Sensitivity analysis of parameters measured in experimental tests
Table 8.6	Uncertainty values for saturated air tests
Table 8.7	The percent of the uncertainty error for the saturated air tests
Table 8.8	Data recorded from a typical propane test
Table 8.9	Boundary conditions for typical saturated propane simulations
Table 8.10	Parameters used in calculating $\beta_1$ , $\beta_2$ and critical radius for propane hydrate
Table 8.11	Measured deposition distance and model prediction for various $Re$
Table 8.12	Uncertainty in parameters and total uncertainty for test no. (1)
Table 8.13	Uncertainty in parameters and total uncertainty for test no. (2)
Table 8.14	Uncertainty in parameters and total uncertainty for test no. (3)

## List of Figures

- Figure 1.1 Precipitation phase boundary for gas hydrate showing the metastable zone, heterogeneous nucleation, homogenous nucleation, and the domains of crystallite formation and dendrite formation (Osegovic, *et al*, 2005)
- Figure 1.2 Pressure and temperature along a typical pipeline (Notz, 1994)
- Figure 2.1 The three common hydrate structures
- Figure 4.1 Growth of particles (Model I)
- Figure 4.2 Development Speed of the Particle (Model I)
- Figure 4.3 The Growth rate vs. particle radius (Model I)
- Figure 4.4 Effect of Kinetic Reaction on Particle Growth rate
- Figure 4.5 Percentage of participating in particle growth with the size of the particle
- Figure 4.6 Delay in size growth due to kinetic reaction process
- Figure 4.7 Influence of saturation on size growth
- Figure 4.8 Effect of saturation on the growth development: a) with time, b) with particle radius
- Figure 4.9 Influence of relative velocity on size growth
- Figure 4.10 Effect of relative velocity on growth rate speed verses time
- Figure 4.11 Effect of relative velocity on growth rate speed verses particle size
- Figure 4.12 Particle distribution of various sizes
- Figure 4.13 Distribution of particles vs. time
- Figure 4.14 Number of particles appearance with the time for different radius
- Figure 5.1 Correction coefficient for non-continuum flow
- Figure 5.2 Deviation in settling velocity as a function of Reynolds number
- Figure 5.3 Lift force on particle near the wall
- Figure 5.4 Lift force on Particle touches the wall
- Figure 5.5 Lift force as a function of particle-wall distance
- Figure 5.6 Adhesive force in particle-wall system
- Figure 5.7 Particle-Particle Adhesion force
- Figure 6.1 Diffusivity and Schmidt Number as a function of particle size
- Figure 6.2 Brownian to settling ratio for various particle sizes
- Figure 6.3 Comparison of non-dimensional deposition velocity as predicted by earlier experiments and models in horizontal pipe
- Figure 6.4 Comparison of deposition factor as predicted by current model and earlier results in horizontal pipe
- Figure 6.5 Decrease of particle number in time due to deposition
- Figure 6.6 Forces acting on a particle within the sublayer region
- Figure 6.7 Variation of external forces for Brownian particles
- Figure 6.8 Variation of external forces for inertia particles
- Figure 6.9 Influence of particle-wall distance on lift force

Figure 6.10	Influence of particle-wall distance on adhesive force
Figure 6.11	Lift force as a function of particle diameter at various distances
Figure 6.12	Adhesive force as a function of particle diameter at various distances
Figure 6.13	Lift-Adhesion Balance Point
Figure 6.14	Flowchart of deposition model
Figure 7.1	Schematic of deposition apparatus using saturated air
Figure 7.2	Numerical prediction of temperature variation through an orifice
Figure 7.3	Schematic of Actual System using propane
Figure 8.1	Schematic of the saturated air case study (identical dimensions of the experiment)
Figure 8.2	Velocity vector and temperature contours generated by CFD simulation: (a) Velocity vector in the orifice region; (b) Enlargement to show circulation; (c) Temperature contours inside the orifice
Figure 8.3	Growing speed for ice particle as a function of time
Figure 8.4	Diameter for ice particle as a function of time
Figure 8.5	Particle distribution as a function of its size
Figure 8.6	Deposition distance of a 10- $\mu\text{m}$ particle calculated based on influence of flow motion and force balance
Figure 8.7	Deposition distance of particles ( $d_p > \delta$ ) calculated based on influence of flow motion and bouncing
Figure 8.8	Deposition distance as a function of particle size initially located at the pipe centerline
Figure 8.9	Influence of Reynolds number on particle deposition location
Figure 8.10	Distance traveled by ice particles due to bouncing as a function of particle diameter for different pipes
Figure 8.11	Deposition distance predicted by simulation and measured during tests as a function of pipe size
Figure 8.12	Comparison of influence of Reynolds number predicted by proposed model and experimental data on deposition distance
Figure 8.13	Comparison of deposition distance predicted by simulation for different types of particles (assumption of particles remaining in ice or liquid forms when reaching wall) with experimental data as a function of the pipe size
Figure 8.14	Hydrate loci for several components found in natural gas (Carroll J.J., 2003)
Figure 8.15	Location of measuring points in the system
Figure 8.16	Hydrate particles deposit on the pipe wall
Figure 8.17a	Propane hydrate growth rate as a function of particle size
Figure 8.17b	Propane hydrate diameter as a function of time
Figure 8.18	Propane hydrate particle distribution as a function of size
Figure 8.19	Comparison of hydrate deposition distance predicted by proposed model and experimental results as a function of Reynolds number

## NOMENCULTURE

$a, b, c$	Characteristic coefficients for certain gas
$A$	Cross sectional area
$C$	Heat capacity
$C_0$	Initial Particle Concentration
$C_{dep}$	Number of Deposited Particle
$C_c$	Cunningham correction factor
$C_D$	Drag Coefficient
$c$	Specific heat
$d_p$	Particle diameter (m)
$D_{pipe}$	Pipe diameter (m)
$e$	Internal energy
$f$	Friction Coefficient
$f$	Fugacity
$f_p$	Penetration Coefficient
$g$	Gravitational acceleration ( $m/s^2$ )
$G$	Particle mass flux
$H_s$	Heat of solution
$j$	Volumetric flux
$K$	Friction and losses constants
$k$	Surface roughness
$k_B$	Boltzmann Constant
$L$	Pipe length (m)
$m$	Mass (kg)
$MW$	Molecular weight
$n$	Number of particles
$P$	Pressure
$Q$	Flow rate
$r_p$	Radius of Particle (m)
$R$	Pipe radius
$Re$	Reynolds Number
$\hat{R}$	Universal Gas constant
$\bar{R}$	Gas constant
$S$	Supersaturation
$S$	Density ratio
$S_L$	Stop Distance (m)
$St$	Stoke Number
$Sc$	Schmidt Number
$t$	time (s)
$T$	Temperature (K)
$u$	Velocity in the ( $x$ ) direction (m/s)
$u^*$	Friction Velocity (m/s)

$u_s$	Settling Velocity (m/s)
$U_g$	Mean gas velocity (m/s)
$V_d$	Deposition Velocity (m/s)
$V_0$	Initial Velocity (m/s)
$W$	Relative velocity
$W_r$	Shaft work
$WA$	Rate of work done by exterior surroundings
$W\Xi$	Rate of work done by other components
$Z$	Compressibility

### Greek Symbols

$\rho$	Density ( $\text{kg/m}^3$ )
$\mu_g$	Gas dynamic viscosity ( $\text{N.s/m}^2$ )
$\lambda_g$	Mean Free Path (m)
$\nu_g$	Gas Kinematics Viscosity ( $\text{m}^2/\text{s}$ )
$\tau_v$	Relaxation time (s)
$\eta$	Collection efficiency
$\Gamma$	Diffusivity ( $\text{m}^2/\text{s}$ )
$\alpha$	Volumetric fraction
$\Xi$	Mass interaction parameter in Equation (3.1)
$\chi$	Net force acting on the component in Equation (3.6)
$\sigma_c$	Tensor stress;
$\sigma$	Surface tension
$\tau$	Shear stress;
$\tau_h$	Adhesive
$\theta$	Driving force
$\Theta$	Rate of heat addition from outside
$\Theta\Xi$	Rate of heat transfer within the system
$\varepsilon$	Energy interaction in Equation (3.13)

### Superscript

$ind$	Induction
$eq$	Equilibrium
$T$	Total

### Subscript

$c$	Critical condition
$C$	Continuous component
$D$	Disperse component
$F$	factor
$g$	Gas
$h$	Hydrate
$N$	Phase or component
$p$	Particle
$s$	Solid
$T$	Temperature

v volume

# CHAPTER 1

## INTRODUCTION

### 1.1 General

Natural Gas is a mixture of hydrocarbon gases that occurs within petroleum deposits. It is principally composed of methane together with varying quantities of ethane, propane, butane, and heavier hydrocarbons, and is used as a fuel and in the manufacture of organic compounds. These hydrocarbon components can appear in multiple phases according to changes in temperature, pressure, and composition. Under certain pressure and temperature conditions, solids may also precipitate resulting in changes to flow of the fluid. The occurrence of such solids may lead to severe problems in oil and gas production systems. One of the most common solid precipitation problems is caused by hydrate clathrates which will be the main focus theme in this research.

Hydrate can pose a major risk in all high pressure natural gas transport lines including the connecting lines and manifold systems in marine transportation of compressed natural gas. Given the significance of safety and reliability in any high pressure natural gas transport system, it is critical to have a very accurate analysis of such systems from the safety stand-point. The variation in pressure and temperature of the system is one of the most significant factors which lead to the formation of hydrate. These circumstances can also be commonly found in exploration and production systems when fluids flow through various types of equipment along the production tubing or transportation pipelines.

Components such as chokes, velocity-controlled subsurface safety valves, and conventional valves and fittings (piping components) can all act as restrictions to the flowing fluids causing changes in the flow conditions (Brill and Mukherjee, 1999).

## **1.2 What is Clathrate Hydrate?**

The term “clathrate”, from the Greek word *khlatron* meaning barrier, refers to crystalline compounds in which small guest atoms or molecules are physically trapped in the host cavities shaped by a three dimensional assembly of hydrogen bonded molecules (Imen *et al.*, 2005).

The crystalline compounds form when gas or a volatile liquid comes in contact with water at high pressures (typically more than 0.6 MPa) and low temperatures (typically less than 300K) (Zhao *et al.*, 2002). These compounds are called clathrate hydrates when they contain water and natural gas hydrates in non-stoichiometric ratio varying from 5.67 to 17 water molecules per hydrate gas molecules (Lee *et al.*, 1998 and Sloan, 1998).

Macroscopically, the structure looks similar to ice or snow, but unlike ice these hydrates are also stable at temperatures above 0 °C (Jinping *et al.*, 2004; Svandal *et al.*, 2005; and Trygve *et al.*, 2006). Gas hydrates represent one of the few phases and perhaps the sole condensed phase where water and light non-polar gases exist together in significant proportions.

Solid gas hydrate masses, up to several meters across, are commonly found in nature. The modern thrust of investigation into gas hydrate is divided into several areas: environment, including global climate, carbon budget, and CO<sub>2</sub> sequestration; seafloor stability, including slope failure and drilling hazards; flow assurance and energy extraction.

The growth of large crystals is made easier by maintaining the system within or near the metastable zone (MSZ), a region free of primary nucleation. The MSZ exists beyond the equilibrium line, within the stability region of hydrate (see Figure 1.1).

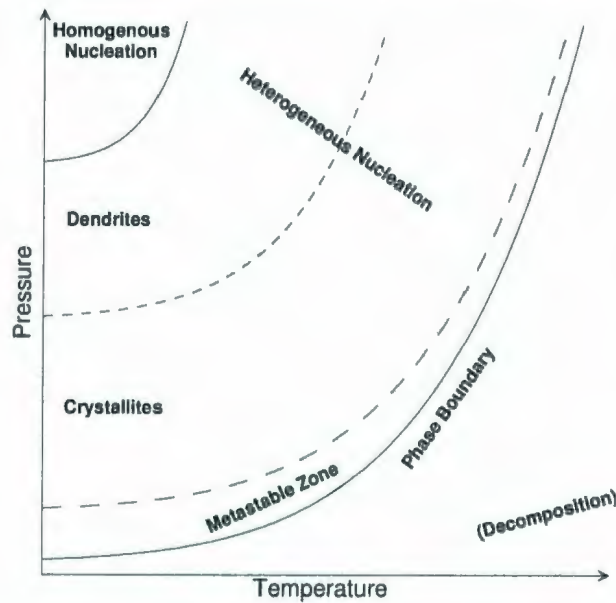


**Figure (1.1)** Precipitation phase boundary for gas hydrate showing the metastable zone, heterogeneous nucleation, homogenous nucleation, and the domains of crystallite formation and dendrite formation (Osegovic, *et al*, 2005)

During nucleation, clusters of solute and water molecules form. Small clusters have large positive surface free energies relative to the volume free energy. Once the cluster radius has reached the critical size, the negative volume free energy becomes the dominant factor and growth becomes spontaneous (Osegovic *et al.*, 2005).

Among several different hydrate structures, the two most common are structure I and structure II. Type I forms with smaller gas molecules such as methane, ethane, hydrogen sulphide, and carbon dioxide, whereas structure II is a diamond lattice, formed by larger molecules such as propane and isobutene (Sloan, 1998). Nitrogen, a relatively small molecule, also forms a type II hydrate (Carroll, 2003). Further, in the presence of free water, temperature and pressure can also influence the type of hydrate structure, where the hydrate structure may change from structure II at low temperatures and pressures to structure I at high pressures and temperatures (GPSA, 1998).

Clathrate hydrates are solid solutions of a volatile solute in the host lattice (van der Waals, 1956). The solvent is known as the empty hydrate lattice. It is thermodynamically unstable. It owes its existence to the fact that the water molecules are linked through hydrogen bonding and form a lattice-like structure with cavities. The diameter of the cavities is between 0.780 and 0.920 nm (Englezos, 1993). Molecules which do not interfere with the hydrogen bonding of water molecules and have a diameter smaller than the diameter of cavity can render the structure stable under suitable pressure and temperature conditions (Englezos, 1993). This stable structure is the *gas hydrate*.

Structure I gas hydrates are formed when these cavities arrange themselves in space in a manner that they link together through their vertices. The unit cell of structure I gas hydrate is a cube with a 1 200 picometer side length and contains 46 water molecules (Englezos, 1993). These molecules have diameters in the range 410-580 picometer (Handa and Tse, 1986).

Structure II gas hydrates are formed when the cavities arrange themselves in space in a manner that they link together through face sharing. A unit cell of gas hydrate of structure II is a cube of side length close to 1 730 picometer, contains 136 water molecules. The diameter of the molecules is less than 410 picometer or greater than 550 picometer (Englezos, 1993).

### **1.3 Why Hydrates are of Interest?**

Over a long period following their discovery by Sir Humphrey Davy in 1810, interest in clathrate hydrates was purely academic. Intense research on natural gas hydrates was conducted by the oil and gas industry when it was pointed out that these compounds were responsible for plugging natural gas pipe (Svandal *et al.*, 2005; Lee *et al.*, 1998; and HammerShmidt, 1934).

Hydrate plugs have disturbed the normal flow of natural gas and other reservoir fluids in the production and transportation lines and have claimed lives of personnel and resulted loss of property in oil and gas industries (Sloan, 1998). They can plug high pressure transportation lines as large as 24 inches and higher and therefore are treated with very careful attention. In fact, light gases such as methane or ethane present in petroleum products, are easily trapped as guest molecules in hydrate structures. The most notable fact that they are non-flowing crystalline solids, denser than typical fluid hydrocarbons and that the gas molecules they contain are effectively compressed, giving rise to numerous applications in the broad areas of energy and climate effects.

The physical properties of these compounds may include an important bearing on flow assurance and safety issues. More recently, they were encountered in refrigeration systems where their crystallization occurred in expansion valves (Imen *et al.*, 2005). However, combating these drawbacks has made it possible to acquire substantial knowledge of hydrates, including their existing conditions, their crystalline structure, their ability to store gas and their heat of dissociation.

Consequently, the interest in hydrates has expanded in other directions because of their potential as a separating agent, and their potential as a storage vehicle (Holder and Enick, 1995). Indeed, gas hydrates naturally found in deep seas and permafrost may provide a large amount of methane. Other positive applications include carbon dioxide sequestration (Lee *et al.*, 2003)], separation (Englezos, 1993) and natural gas storage and transportation (Sloan, 2000). Finally, the use of their dissociation energy can be applied in refrigeration processes and cold storage (Tanasawa and Takao, 2002; Fournaison *et al.*, 2004).

To touch on the importance of hydrate research, it is more convenient to detail their advantages and shortcomings from an economic point of view. Several key physical properties of hydrates determine the roles that they play (or might play in the future) in both industry and environment. They are solids with densities greater than those of typical fluid hydrocarbons, and this has practical implications for flow assurance in pipelines and the safety thereof. Furthermore, the fact that, in effect, hydrates concentrate their guest molecules, results in three potential applications: that energy can be recovered

from *in situ* hydrates; that hydrates can be used to transport stranded gas; and that hydrates may be a factor in climate change. Each of these implications and applications is discussed briefly below.

### **1.3.1 Hydrate as an Energy Source**

The vast amounts of gas hydrates in the Earth's crust might be considered as a new source of sustainable energy. Makogon (1965, 1988) and Kvenvolden (1988) pointed out that the amount of gas in known hydrate reserves up until 1988 was at least twice as much as the energy contained in the total fossil fuel reserves. A unit volume of methane hydrate can yield 164 times more methane than a unit volume of gaseous methane under the same pressure conditions and at standard temperature (Davidson DW *et al.*, 1978).

This study was completed by Collett and Kuuskraa (1998), who estimated that these gas reserves range from  $1.4 \times 10^1$  to  $3.4 \times 10^4$  trillion cubic meters (tcm) for permafrost areas and from  $3.1 \times 10^3$  to  $7.6 \times 10^6$  tcm for oceanic sediments. It is important to note that the total discovered conventional natural gas reserves in 2006 amounts to about 180 tcm (BP magazine, 2006). Gas hydrate deposits are mainly distributed offshore due to the high pressure and low temperature conditions at the seabed and more parsimoniously encountered in permafrost (Kvenvolden, 1995 and Sloan, 1998). However gas hydrate deposits might represent a real threat to the environment. For instance destabilizing hydrate sediments plays an undeniable role in climate change due to the great amount of Methane that is released as a result of any slight global warming (Brewer, 2000).

### **1.3.2 Storage and Transportation**

It is estimated that about 70% of the total gas reserve is either too far from an existing pipeline or too small to justify liquefaction facility (Sloan, 2003). Gudmundsson and Borrehaug (1996) suggested that it is economically feasible to transport stranded gas in hydrated form.

### **1.3.3 Safety**

When hydrate blockages dissociate in pipelines, they detach first at the pipe wall; therefore, any pressure gradient across the high-density hydrate plug will cause the hydrate to travel rapidly (~300 km/hr) down the pipeline. This effect will compress the downstream gas, either causing pipeline blowouts or causing the plug to erupt through pipeline bends. A second safety concern arises when hydrate plugs are locally heated (for example, using a blowtorch outside a pipeline) to dissociate them. Frequently, the evolving gas from the hydrate is contained by the ends of the plug until the pipeline bursts owing to the pressure being too high. This safety concern is a result of the next hydrate property- the ability of hydrates to concentrate high levels of gas.

### **1.3.4 Pipeline Plugging**

In thermal-hydraulic design of multiphase transmission systems, the system designer is encountered with several challenges associated with multiphase flow, which can significantly change design requirements. The aim of any pipeline designer is to secure "flow assurance" i.e., the transmission system must operate in a safe, efficient, and reliable manner throughout the design life. Failure to do so has significant economic

consequences, particularly for offshore gas production and transportation system (Mokhatab *et al.*, 2006).

“Flow assurance” covers the whole range of possible flow problems in pipeline, including multiphase flow and fluid-related effects such as gas hydrate formation, wax and severe slugging. The avoidance or remediation of these problems is the key aspect of flow assurance that enables the design engineer to optimize the production system and to develop safe and cost-effective operating strategies for the range of expected conditions, including start-up, shutdown, and turndown scenarios. However, as production systems go increasingly deeper, flow assurance becomes a major issue for offshore production and transportation systems, where traditional approaches are inappropriate for deepwater development systems due to extreme distances, depths, temperature, or economic constraints (Wilkens, 2002).

The marine transportation of natural gas in compressed form using ocean going ships is an evolving technology in which gases with various composition and therefore water contents might be considered for transportation in high pressure storage systems. The production and transfer of gas to the ships involve various pressure and flow control systems within relatively small diameter transport lines through which the gas may easily face the Joule-Thompson effect (Berner, 1992) similar to those encountered in offshore oil and gas production systems. The formation of hydrate in flowlines in compressed natural gas (CNG) transporting ships during loading and unloading operations can also potentially pose severe risk factors to such systems.

While many other factors influence hydrate formation, the temperature and pressure at locations across the system are the key factors to be considered when predicting the likelihood of the hydrate forming (Jadhawar, 2003). The exact temperature and pressure at which hydrates form depend on the composition of the gas and the water. For any particular composition of gas at a given pressure, there is a temperature below which hydrates will form and above which hydrates will not form. As the pressure increases, the hydrate formation temperature also increases. As a general rule, as pressure increases or as the system becomes colder, the tendency to form hydrates increases (GPSA, 1998). Hence, many gas-handling systems are at significant risk of forming hydrate plugs during shut-in and subsequent start-up (Mokhatab *et al.*, 2006).

Hydrate propagation tends to gradually form a plug that separates the pipe into two pressure sections: a high pressure section between the well or high pressure gas source and the plug and a second section at low pressure between the plug and the gas recovery division. In the upstream section, a pipe blast can occur due to pressure rise. The plug can also behave as a projectile that destroys the pipe when the pressure difference between the upstream and downstream sections increases. Both events can endanger personnel safety and damage production equipment (Sloan, 2000).

Hammerschmidt (1934) indicated that the formation of gas hydrate was responsible for blocking pipelines. Considering the significant economic risks in the gas and oil industry, a great deal of research has been conducted by petroleum industry to inhibit this undesirable phenomenon. Annually, an operating expense greater than \$500 million is

devoted to hydrate prevention (Lederhos *et al.*, 1996), almost half of that is devoted for hydrate inhibition (Sloan, 2003). In addition, offshore operations spend approximately \$1,000,000 per mile for insulation of subsea pipelines to prevent hydrates (Sloan, 2003). Further, Lysne (1995) listed three incidents in which hydrate projectiles erupted from pipelines at elbows and caused loss of three lives and over \$7 million (US) in capital costs. Accordingly, concerns have been expressed about the effect of hydrates on foundations of platforms and pipelines, as well as offshore drilling.

First and perhaps most importantly, when hydrates form, they are solid, non-flowing crystalline structures. Oil and gas wells always produce undesired water along with hydrocarbons that are in the hydrate guest size range. As the flowing mixed phases cool, hydrates form and plug transmission lines, causing costly production stoppage, sometimes for as long as months, in large pipelines, while the hydrates are dissociated (Sloan, 2003).

Fortunately, the hydrate stability temperature and pressure range is predictable to within experimental accuracy using modern thermodynamic programs usually based upon the Gibbs free energy extension (Ballard and Sloan, 2002) of the van der Waals and Platteeuw (1959) method. Such multiphase programs (e.g. PIPEPHASE<sup>®</sup>) can predict the pipeline conditions leading to free hydrate formation. Figure (1.2) shows the pressure and temperature conditions superimposed on the hydrate stability curves (Bollavaram, 2002). At a short distance, say 7 miles, the fluid stream retains the high temperature from the hot reservoir. The ocean cools the fluid stream, and at 9 miles, the fluid enters the hydrate

stability region. Typically, these conditions commonly exist in wells, valves, flow lines and meter discharges. In a pipeline, hydrates form at the hydrocarbon-water interface, and accumulate. Once the hydrates accumulate enough to plug the pipeline, they hinder flow through pipeline. This is a major safety and economical concern to the industry. Unfortunately, low temperatures (such as the deep-sea floor temperature of 277 K) and the mandates of high pressure for economic energy densities place many pipelines well within the hydrate-formation region.

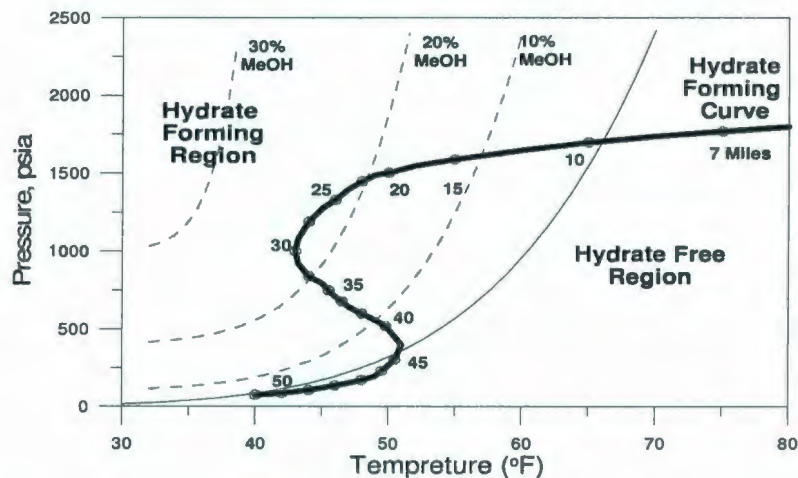


**Figure (1.2)** Pressure and temperature along a typical pipeline (Notz, 1994)

#### 1.4 Objectives of Proposed Research

The objectives of the current study can be summarized as follows:

1. A novel and comprehensive model for prediction of hydrate deposition location in high pressure natural gas flowlines is proposed. The model should be able to predict the distance between the spots where the conditions for hydrate formation exists and the actual location of hydrate agglomeration. The main goal is to develop an efficient

simulation algorithm that has the capability to foresee the location, migration, and agglomeration of hydrate particles. The flow of a single Fluid (gas) through a restriction device (such as an orifice) is simulated by combining existing physical transport, thermodynamics, and hydrate models.

2. A new definition for the process of nucleation and growth of hydrate particles is introduced. Based on the law of mass action, the new approach describes the process of particle growth and distribution using analytical correlations. These equations can be used to explain the growth of the hydrate particles with time and can also demonstrate the influence of flow structure on the process.

3. A robust model for predicting the trajectory of hydrate particles is developed. The model divides the flow regime into two regions, the turbulent and the sublayer regions, each region having its own model for tracking the hydrate particle.

4. In the near wall region, the particle bouncing effect is considered for particles with sizes of the order of, and larger than sublayer thickness. Since the particle-wall collision is sufficient enough to keep the particle moving forward, the distance traveled by the particle due to bouncing extends the deposition distance.

### **1.5 Outline of Thesis**

The thesis is organized as follows:

- Chapter 2 reviews literature related to hydrate structure, physical properties, formation, and treatment.
- Chapter 3 outlines the governing equations of multiphase flow built in the CFD software and used to describe the flow configuration.

- Chapter 4 presents a new mathematical modelling approach to demonstrate the hydrate nucleation formation and distribution in a gas flow.
- Chapter 5 details the forces exerted on particles travelling in a fluid.
- Chapter 6 describes the proposed novel algorithm to predict hydrate particle deposition in high pressure gas flowlines.
- Chapter 7 explains the experimental apparatus and its parts that used to perform verification tests in this study.
- Chapter 8 discusses two model verification case studies specifically tests with saturated air and saturated propane
- Chapter 9 summarizes the findings of this research and suggests areas that need to be further considered in future examination.

## CHAPTER 2

### LITERATURE SURVEY

#### 2.1 General

The literature reviews and articles concerning gas hydrate are numerous. The literature includes but is not limited to the structure of hydrate, favourable conditions to form, hydrate formation and growth, thermodynamic properties, potential for hydrate formation, flow assurance, and dissociation techniques. In this chapter, a brief review of the research on the structure of hydrates will be presented followed by a concise review of the properties of hydrate. The research relevant to the formation and growth of hydrate will then be covered in details, and finally the chapter will be concluded by reviewing the literature concerning the dissociation and inhibition of hydrates.

#### 2.2 Hydrate Structures

Hydrates are hybrid crystalline structures formed when small gas molecules are in contact with water. As illustrated in Fig. (2.1), there are three basic hydrate structures known to form from natural gases, structure I (sI), structure II (sII), and structure H (sH). The type of hydrate that forms depends on the size of the gas molecules included in the hydrate. As a rule of thumb, small molecules such as methane or ethane form sI hydrates as single guests, larger molecules such as propane and *i*-butane form sII hydrates. Larger molecules such as *i*-pentane form sH hydrates in the presence of a “help” molecule such as methane (Bollavaram, 2002). The type of hydrate that forms depends on the composition, temperature, and pressure of the system.

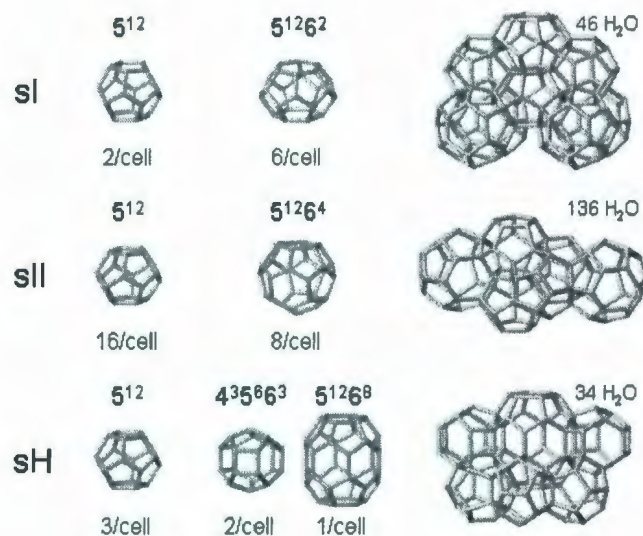


**Figure (2.1)** the three common hydrate structures (Bollavaram, 2002)

Numerous literatures studied the structure of hydrates. Palin and Powell (1945) reported the results of the X-ray analysis of the crystalline compound formed between quinol (hydroquinone) and sulfur dioxide. They also discussed and revealed the structure of the clathrate compound of quinol with methanol and other compounds. Later, X-ray analyses revealed that gas hydrates could be recognized as Clathrates and crystallize in two distinct cubic structures (Englezos, 1993). Von Stackelberg (1949 a, b) reported the conclusion of his work over 20 years of investigation and proved that all crystals form in the cubic class. Claussen (1951) constructed a cubic unit cell containing 136 water molecules and proposed structure II hydrates. His results were immediately confirmed by

von Stackelberg and Muller (1951). Simultaneously, Pauling and Marsh (1952) determined structure I hydrates.

Many structural, calorimetric, and molecular simulation studies were carried out by Davidson and his co-workers at National Research Council (NRC) of Canada (1978). Their structural work led to: i) endorsing the purely theoretical study of Holder and Manganiello (1982), which suggested the elucidation of hydrate structure II that the small molecules of argon, krypton, oxygen, and nitrogen can form (Davidson *et al.*, 1984, 1987), and ii) the identification of the third hydrate structure, structure H (Ripmeester, 1987, 1990).

### **2.3 Hydrates Properties**

Despite more than 200 years of gas hydrate history, their properties were studied very little due to the fact that the research is extremely complicated. The study of the hydrates' properties was initiated with the advent of modern measurement techniques. Recently, hydrates are studied on the molecular level using the most advanced instruments, such as X-ray diffraction, Nuclear Magnetic Resonance (NMR), proton NMR, infrared (IR) spectroscopy, and quantum microcalorimetry. Only after the study of gas hydrates structure using NMR and EPR were completed, the methods for calculating the hydrate density was developed (Makogon, 1997). The density could be determined by knowing the parameters of hydrate lattice, the filling ratio of cavities in the structure, and the density of hydrate of a former gas with known molecular mass. The number of studies related to the direct study of mechanical, thermal deformation parameters of hydrates and

hydrate-saturated media is limited. These studies were completed by Parameswaran and Paradis (1985, 1989), Cameron, Baker and Handa (1989), and Jeanjean and Briaud (1990). Handa *et al.* (1990) compared the strength characteristics of ice-and hydrate-saturated sandstone and found that at  $-10^{\circ}\text{C}$  the ice-saturated sandstone failed under stress of  $P = 7$  MPa, while hydrate-saturated sandstone failed at  $P = 12.2$  MPa. That means hydrate-cemented samples are stronger than ice-cemented ones.

The thermo-physical properties of hydrate formation and decomposition processes are extremely important in all problems of the natural gas hydrate. Quite accurate results have been obtained through instrumental methods and allowed to calculate the heat of hydrate formation, their heat capacities, and thermal conductivities. The latter is extremely important for the development of thermal methods of treatment of hydrate-saturated deposits in gas production systems, for applications involving the removal of hydrates in gas production, transportation, and processing systems, and also for the climate calculations (Makogon, 1997).

The impetus for measuring thermal conductivity measurement studies was initiated by Stoll and Bryan (1979). They indicated anomalously low thermal conductivity for bulk hydrate. Among the experimental studies on the thermal conductivity for hydrates of methane and several other gases, as well as for ice and water at various temperatures and pressures, results showed that the thermal conductivity of hydrate is close to that of water and slightly increases with temperature (Makogon, 1997). In turn thermal conductivity of ice at freezing temperature is four times higher than that of hydrates and decreases

significantly with temperature (Makogon, 1997). These results indicate that further research of thermal conductivity of hydrates of pure gases and natural gas mixtures, and of the hydrate saturated rock at various pressures and temperatures is extremely important.

The anomalies in the thermal conductivity mentioned earlier often manifest themselves in the heat capacity (Callanan and Sloan, 1983). Heat capacity of hydrates is one of the major thermodynamic parameters affecting their accumulation, decomposition, and structural characteristics. The heat capacity of hydrates depends on the composition and type of hydrate (Callanan and Sloan, 1983; Makogon, 1997) as well as on the pressure and temperature (Makogon, 1997). Callanan and Sloan (1983) correlated the average heat capacity for four hydrates using differential scanning calorimeter. A polynomial was fitted to represent heat capacity data as a function of temperature for each hydrate using the information obtained from their experiments.

## **2.4 Hydrate Formation**

Literature related to hydrate formation is summarized as follows:

### **2.4.1 Induction Time**

Hammersmidt (1934) first indicated that there could be an induction period associated with the appearance of the first crystals from a hydrocarbon-water mixture. The gas-water mixture should have a suitable composition at the right temperature and pressure such that hydrates could thermodynamically form.

During their studies on the formation of gas hydrates containing Ar, Kr, and Xe, Barrer *et al.* (1967) found that the induction period varied with the type of the hydrate former. The induction time is defined as the mean time lapse for the appearance of the first crystal in the fluid. However, this time includes the nucleation time and the time required for crystals to grow from the critical size ( $r_c$ ) to an observable size (Liu *et al.*, 2003).

Natarajan *et al.* (1994) discussed the induction phenomena associated with methane, ethane and carbon dioxide hydrate formation and offered a correlation for the induction time based on a large number of experiments with three hydrate formers namely, methane, ethane, and carbon dioxide. Skovborg *et al.* (1993) reported isothermal experimental data on induction times for the formation of methane and ethane hydrates. They found the induction time to be strongly dependent on the stirring rate of gas water mixture and on the deviation of potential driving force. This deviation, known as driving force, can be expressed as the degree of super-cooling, or the degree of overpressure or thermodynamically using a suitable function of the fugacity of the hydrate forming gas.

Monfort and Nzihou (1993) found that probability of hydrate formation at a given time decreases with decreasing degree of super-cooling. In their experimental tests, they investigated the sub-cooling driving force, defined as the difference between equilibrium and experiment temperature ( $T_{eq} - T_{exp}$ ), and its influences on hydrate nucleation and growth time. They showed that induction period was relatively short at large Temperature Driving Force (TDF). Moreover, they observed that when a solution that has been

preliminary hydrated and rapidly depressurized is used, during a second hydrate formation cycle:

- The induction time is greatly reduced.
- The crystal growth occurs on sites different from those observed during hydration in a fresh water solution.

Herri *et al.* (1999) studied the nucleation and mechanism of crystallization of methane hydrate and observed that appearance of first crystals was generally not immediate, but occurs after a certain period. They studied experimentally the influence of pressure as a driving force and showed the good agreement between the experimental behaviour and the classic law of Zettlemoyer (1969) which formulated the induction period as:

$$t_{ind} = \exp\left(\frac{B}{\log^2(P_{sys} / P_{eq})}\right) \quad (2.1)$$

Where,  $B$  is a constant.

In his experimental study on the influence of agitation on the induction time, Sun C. (2004) showed the impact of system pressure and flow rate on induction period. He suggested that induction time was influenced by the turbidity time, the time when the solid hydrates grow in the solution, and the solubility time, the time need for gases to dissolve into the liquid and the aqueous solution when it is not yet saturated. He determined the induction period by analyzing the experimental data and came up with the following formula:

$$t_{ind} = K \left( \frac{f_g^V}{f^{eq}} \sqrt{Q/Q_0} - 1 \right)^{-m} \quad (2.2)$$

Where,  $K$  and  $m$  are constants,  $f^{eq}$  the three phase equilibrium fugacity (MPa),  $f_g^V$  the fugacity of the dissolved gas in the liquid, (MPa),  $Q$  is liquid flow rate and  $Q_0$  is a reference flow rate ( $Q/Q_0$  shows the influence of agitation in the flow system).

Jinping Li; *et al* (2004) studied the influence of agitation and adding surfactants and inoculating seeds on the induction time. Their target was to reduce the induction time and super-cooling degree of crystallization and to promote the growth rate of gas hydrates. Their experiments, however, concluded that there are some limitations in the effective use of the above methods in practice. Other means such as employment of ultrasonic and magnetic fields have been studied as well and have shown favourable effects on the formation of gas hydrates (Jinping, 2004).

#### 2.4. 2 Growth Rate

It is important to note the distinction between nucleation, growth, and deposition of hydrate particles. During the nucleation process, solid crystals may form, but no operational problems will occur if the crystals are carried along by the flowing fluids. The hydrate growth may occur both before and after deposition, for instance on the pipe wall, although difficulties only arise if the solid begin to deposit and stop moving.

The nucleation process has a random component and hence is difficult to model. It may occur instantaneously or may take several days to start. On the contrary, the growth of hydrate crystals is amenable to mathematical modeling.

While many factors influence the hydrate formation, the two major conditions that promote this process are the gas being (Sloan, 1998):

1. At the appropriate temperature and pressure; and
2. At or below gas dew point.

Other factors that affect, but are not necessary for hydrate formation include turbulence, nucleation site, surface for crystal formation, agglomeration, and the salinity of the system (Mokhatab *et al.*, 2006). Makogon (1981) described the factors which affect hydrate nucleation and growth; those factors include super-cooling, pressure, temperature, state of water, composition, and state of the gas-hydrate forming system.

In general, temperature is thought to increase the rate of any kinetic process. However, higher gas temperatures also decrease the pressure driving force and will tend to impede the rate over the temperature range used. Driving force has been addressed by many authors. Knox *et al.* (1961) and Lee *et al.* (1998) identified the degree of super-cooling (TDF) as an important factor in the rate of hydrate formation. The growth rate response to perturbation in the (TDF) has been also addressed by Erik *et al.* (2001). Their results indicated that growth rate has a linear dependence with bulk temperature at constant equilibrium temperatures but is nonlinearly dependent on equilibrium temperature at

constant bulk temperatures. The latter unexpected behaviour was attributed to the ambiguity in the defined driving force.

Higher pressures increase the rate of hydrate formation (Lee *et al.*, 1998 and Hwang *et al.*, 1990). However, the experimental results of Osegovic *et al.* (2005) indicated that the rate of nucleation unexpectedly levelled off at higher pressures because probably nucleation becomes mass transfer limited at higher pressures.

Another factor that may be important in the hydrate formation process is the ability to stabilize the large cavity of the hydrate structure (Lee *et al.*, 1998). The stability and kinetics of hydrate depends on temperature and pressure as well as on the concentrations of all components involved in the phase transition (Svandal *et al.*, 2005). Higher gas flow rate tends to produce higher rates of hydrate formation (Lee *et al.*, 1998). This is because the higher gas flow rates dissipate the considerable heat release generated during hydrate formation and also improve the mass transfer of water to the hydrate-forming surface. However, the experiments by S.Y. Lee *et al.* (1998) showed that the effect of gas flow rate levelled off at higher rates. Thus mass and heat transfer are no longer limiting.

It was also noticed that no clear difference in growth rate was observed for the 95% methane and 97% methane mixtures, but the rates for gas mixtures and for carbon dioxide were faster than for pure methane (Lee *et al.*, 1998). Taro *et al.* (2002) also observed that the growth rate of CO<sub>2</sub> hydrate became fast particularly in the temperature range just below melting point of ice.

Nerheim *et al.* (1992) reported the results of their investigation on hydrate kinetics in the nucleation and early growth phase by laser light scattering. Their measured nuclei sizes were found to compare well with those calculated by Englezos *et al.* (1987a). The model of Englezos (1987 b) was adopted to predict the growth of hydrates and it was found that the model predictions matched the experimental data well. Hwang *et al.* (1990) studied the formation of methane hydrates from the melting of ice and concluded that the rate of formation depended on the rate of supply of hydrate former to the growth surface and the rate of removal of the heat from the forming surface.

Lee *et al.* (1998) experimentally measured the rates of hydrate formation at various conditions. They physically simulated their system such that gas was flowing at rates comparable to those that might exist in gas transmission pipelines. Hydrates formed at 7.58 MPa and around 280 K in a mixture of methane with 3% and 5% propane. The reaction rates for forming hydrates were proportional to the pressure driving force, the pressure difference between the system pressure and the equilibrium pressure. According to their results, linear growth rates of 0.2 cm/h were likely to represent the maximum growth rate that could be expected in gas transportation lines operated at ocean temperatures of 275-277 K. This is because as hydrates thicken, they can serve as insulators of the line, which will result in slower cooling of the produced fluids. The insulation will produce higher transportation temperatures, which would inhibit hydrate formation.

Bilyushove *et al.* (1988) analytically studied the hydrate formation in a pipeline. He mathematically modeled the process of hydrate formation in pipeline transport of a moist gas. The analysis of the result showed that hydrate formation is possible if the input concentration of water vapour in the gas exceeds the minimum required for the given conditions, which depends on a number of parameters such as external temperature, the heat liberation coefficient, and the thermal conductivities of the hydrate and surrounding material. His model also concluded that the hydrate is distributed non-uniformly over the length of the pipe. The position of the maximum hydrate layer thickness move down the flow as time passes and the velocity of this motion decreases with increase in the concentration. Then the hydrate layer grows monotonically with time, which in case of long term use of the pipeline with unchanging gas parameters can lead to total blockage of the pipe. Also, increase in temperature of the surrounding material leads not only to increase in the dew point of the gas transportable without hydrate formation, but also to a slowing of the hydrate formation rate.

The coefficient of heat liberation from the gas to the hydrate has a significant effect on the process of hydrate formation and decomposition in wells and pipelines. Results showed that with increase in the heat liberation coefficient, the leading edge of the hydrate layer is located closer to the input section and the thickness of the hydrate layer increases significantly (Bilyushove *et al.* 1988). Hydrate formation in the tube depends significantly on the heat and mass liberation coefficients, which in turn are determined by the mass flow rate of the gas. On the other hand the gas flow rate determines the gas flow parameters and through them affects the hydrate formation process.

Svandal *et al.*'s (2005) experimental study on growth and dissociation of CO<sub>2</sub> showed that the growth and dissociation of CO<sub>2</sub> hydrates were governed by the diffusion of CO<sub>2</sub> in the aqueous phase particularly the initial mole fraction of CO<sub>2</sub> in the aqueous phase. Recently, Tegze *et al.* (2006) applied a phase field theory with model parameters evaluated from atomistic simulations/experiments to predict the nucleation and growth rates of solid CO<sub>2</sub> hydrate in aqueous solutions. They determined the growth rate from phase field simulation as a function of composition. They found that the growth rates predicted by theory were about three orders of magnitude too high in comparison with respective experimental observation. They suggested that the kinetic barrier reflecting the difficulties in building the complex crystal structure was the most probable source of the deviation.

Glew and Hagget (1968 a and b) studied the kinetics of ethylene oxide (EO) hydrate formation. They correlated their results and found the EO hydrate growth was limited by heat transfer from hydrate slurry. Different dependencies, however, were found by Pangborn and Barduhun (1970), who studied the kinetics of methyl bromide hydrate formation in a continuous stirred tank reactor. Their study showed that hydrate formation rate appears to be controlled mainly by the kinetics of interfacial reaction to form crystals.

Graauw and Rutten (1970) proposed a mass transfer-based model for the kinetics of hydrate formation. They used chlorine and propane as the hydrate forming substances

and showed that mass transfer at the hydrate-forming substance-water interface can be a rate-determining factor. However, the hydrate formation reaction at the surface can also become a rate-determining step. Svandal *et al.* (2006) confirmed the dominating effect of the mass transport of solutes towards the growing front.

Scanlon and Fennema (1972) found in their studies of the formation of ethylene oxide hydrate (structure I) and of tetrahydrofuran (THF) hydrate (structure II), that at any degree of super-cooling, hydrate-forming solutions crystallized more slowly than pure water, and the THF hydrate crystallized more slowly than hydrate of ethylene oxide. They attributed this difference to the fact that the rate of hydrate formation should decline as more molecules of water are required to associate in an orderly fashion with each molecule of hydrate former.

Werezak (1969) examined the rate at which the solute concentration was increasing due to hydrate formation in aqueous solutions of coffee extract, sucrose, and sodium chloride. It was found that miscible hydrate formers exhibited higher rate of formation compared to the slightly soluble hydrate formers used. The rate of solution concentration was found to be a function of the initial thermal driving force and heat transfer capabilities of the hydrate formation vessel.

## **2.5 Preventing Hydrate Formation**

Gas hydrates, as mentioned in Chapter 1, may be of potential benefit both as an important source of hydrocarbon energy and as a means of storing and transporting natural gas.

They however pose severe operational problems, as the crystals may deposit on the pipe wall and accumulate as large plugs that can completely block pipelines and lead to shutting in production (Sloan, 1998 and GPSA, 1998).

Methods of preventing hydrate solids development in gas production systems have been of considerable interest for a number of years (Bufton, 2003). The chemical methods, which can be used either to prevent or to remove plugs, consist of injecting additives in the pipe that act differently on hydrate agglomeration according to whether the inhibitors are thermodynamic (TI), kinetic (KI), or dispersant (DI).

The hydraulic removal method is based on the dissociation of the hydrate plug by depressurization. This method seems promising, given the porous structure of the gas pipeline plugs (Sloan, 2000; Kelkar *et al.*, 1997).

Thermal methods consist of delivering a local heat flow towards the plug through the pipe wall in order to raise the system temperature above the hydrate formation point. This method is possible for onshore pipelines but unsuitable for subsea equipment (Sloan, 1998). Mechanical methods, such as pipeline pigging, can be used to prevent hydrate plugs. Pipeline pigs are inserted into pipe and travel throughout the pipeline, driven by fluid flow. These projectiles then remove the obstacles or deposits they encounter (Sloan, 2000).

The ultimate remedy for hydrate problem is to remove or reduce the water content of the gas using gas dehydration processes. However in practical field operation, water can be economically removed only to a certain vapour pressure and residual water vapour always exists in a dry gas (Denney, 2005). Gas dehydration reduces the risk of rapid hydrate formation and deposition.

## **2.6 How This Work Helps the Hydrate Community**

This work involves an important problem in oil and gas production, processing and transportation. The question is: if hydrates form due to a contraction (such as an orifice) in a pipe, where would be the accumulation spot and how this distance could be related to the geometry of the contraction, pressure reduction, and flow configuration?

The following questions would be answered in this thesis:

1. What are the factors that dominate the growth and distribution of hydrates? Theoretical correlations for the growth rate and particle distribution of a hydrate are developed. Two main processes govern the formation, growth, and distribution of hydrates; mass transfer and the reaction kinetic. The correlations could account for the behaviour of the process of hydrate growth and size distribution with time.
2. What are the major variables that influence hydrate deposition process and how are they related? There are many factors that may dominate the process of particle travels such as particle size, particle-wall interaction, and flow conditions and geometry of the gas carrier. Our model should be comprehensive enough to take the impact of these

parameters into consideration and be able to predict the location of hydrate accumulation as accurately as possible.

3. How do we quantitatively anticipate the agglomeration position? A novel mathematical model proposed in the thesis divides the migration of the particle towards the pipe wall into two main regions, the fully turbulent and the sublayer regions; the latter is modelled based on the size of the particle and on the forces experienced by the particle.

## CHAPTER 3

### Mathematical Model of Flow Structure

This chapter summarizes the transport equations of gas/solid multiphase flow in differential form and explains briefly the computational fluid dynamics (CFD) technique used to solve these equations. More details can be found in many texts and literatures such as (Brennen, 2005), (Gidaspow, 1994) and Jassim *et al.* (2006).

#### 3.1 Equations of Motion

It is implicitly assumed that an *infinitesimal* volume of dimension  $\varepsilon$  is considered to define the flow model. The dimension parameter  $\varepsilon$  is considered such that it is very much smaller than the typical distance over which the flow properties can significantly vary but is very much larger than the size of individual phase elements (the disperse phase particles, drops, or bubbles). The first condition for the dimension parameter is necessary to define derivatives of the flow properties within the flow field. The second condition is necessary so that each *averaging* volume (of volume  $\varepsilon^3$ ) contains representative samples of each of the components or phases.

### 3.1.1 Continuum Equation for Conservation of Mass

The 3D continuity equation of component  $N$  can be written as:

$$\frac{\partial}{\partial t}(\rho_N \alpha_N) + \frac{\partial(\rho_N \alpha_N u_{Ni})}{\partial x_i} = \Xi_N \quad (3.1)$$

Where,  $u_{Ni}$  velocity and  $\alpha_N$  volumetric fraction of the component (or phase),  $N$ .  $\Xi_N$ , called the *mass interaction term*, is the rate of transfer of mass to the phase  $N$  from other phases per unit total volume.

For each phase or component there is continuity equation present in the flow called the Individual Phase Continuity Equation (IPCE). Since the mass as a whole must be conserved whatever phase changes happen, it follows that:

$$\sum_N \Xi_N = 0 \quad (3.2)$$

In the other words, the sum of all the IPCEs results in a Combined Phase Continuity Equation (CPCE) that does not involve  $\Xi_N$  as follows:

$$\frac{\partial}{\partial t} \left( \sum_N \rho_N \alpha_N \right) + \frac{\partial}{\partial x_i} \left( \sum_N \rho_N j_{Ni} \right) = 0 \quad (3.3)$$

or

$$\frac{\partial \rho}{\partial t} + \frac{\partial}{\partial x_i} \left( \sum_N \rho_N \alpha_N u_{Ni} \right) = 0 \quad (3.4)$$

where,  $\rho$  is mixture density

### 3.1.2 Disperse Phase Number Continuity

Complementary to the equations of conservation of mass are the equations governing the conservation of the number of particles, drops, or bubbles that constitute a disperse phase.

The equation takes the form:

$$\Xi_D = n_D \left( \frac{\partial(\rho_D v_D)}{\partial t} + u_{Di} \frac{\partial(\rho_D v_D)}{\partial x_i} \right) = n_D \frac{D}{Dt} (\rho_D v_D) \quad (3.5)$$

Where,  $n_D$  is the number of particles of the disperse component,  $D$ , per unit total volume.  $D/Dt$  denotes the Lagrangian derivative following the disperse phase. This demonstrates a result that could, admittedly, be assumed a priori. Namely that the rate of transfer of mass to the component  $D$  in each particles,  $\Xi_N/n_D$ , is equal to the Lagrangian rate of increase of mass,  $\rho_D v_D$ , of each particle.

### 3.1.3 Continuum Equation for Conservation of Momentum

Viewed from Lagrangian perspective, the momentum equation of component  $N$  is:

$$\rho_N \alpha_N \left\{ \frac{\partial u_{Nk}}{\partial t} + u_{Ni} \frac{\partial u_{Nk}}{\partial x_i} \right\} = \alpha_N \rho_N g_k + \chi_{Nk} - \Xi_N u_{Nk} - \delta_N \left\{ \frac{\partial p}{\partial x_k} - \frac{\partial \sigma_{Cki}^D}{\partial x_i} \right\} \quad (3.6)$$

Where, the left-hand side is the normal rate of increase of the momentum of the component  $N$ . The term  $\Xi_N u_{Nk}$  is the rate of increase of the momentum due to the gain of mass by that phase.  $\chi_{Nk}$  is the force that each component impose on the component  $N$ .  $\delta_D = 0$  for the disperse phase and  $\delta_C = 1$  for the continuous phase.

If the momentum equations, Eq. (3.6), for each of the components are added together, the resulting Combined Phase Momentum Equation (CPME) becomes the following:

$$\frac{\partial}{\partial t} \left( \sum_N \rho_N \alpha_N u_{Nk} \right) + \frac{\partial}{\partial x_i} \left( \sum_N \rho_N \alpha_N u_{Ni} u_{Nk} \right) = \rho g_k - \frac{\partial p}{\partial x_k} + \frac{\partial \sigma_{Cki}^D}{\partial x_i} \quad (3.7)$$

### 3.1.4 Disperse Phase Momentum Equation (DPCE)

Newton's equation of motion for an individual particle of volume  $v_D$  may be written as:

$$\frac{D_D}{D_D t}(\rho_D v_D u_{Dk}) = F_k + \rho_D v_D g_k \quad (3.8)$$

Where,  $F_k$  is the force that the surrounding continuous phase imparts to the particle in direction  $k$  and includes not only the force due to the velocity and acceleration of the particle relative to the fluid but also the *buoyancy* forces due to pressure gradients within the continuous phase. Expanding Eq. (3.8) and using Eq. (3.5) for the mass interaction,  $\Xi_D$ , one obtains the following form of the Disperse Phase Momentum Equation (DPME):

$$\rho_D v_D \left\{ \frac{\partial u_{Dk}}{\partial t} + u_{Di} \frac{\partial u_{Dk}}{\partial x_i} \right\} + u_{Dk} \frac{\Xi_D}{n_D} = F_k + \rho_D v_D g_k \quad (3.9)$$

Now if we set  $\alpha_D = n_D v_D$  in Eq. (3.6), expand and compare the result with Eq. (3.9), using the continuity, we would end up with:

$$\chi_{Dk} = n_D F_k \quad (3.10)$$

Hence the appropriate force interaction term in the disperse phase momentum equation is simply the sum of the fluid forces acting on the individual particles in a unit volume, namely  $n_D F_k$ . Extensive discussions of the forces acting on the particle (drag, buoyancy, left and adhesive) can be found in the literature (Brennen, 2005).

### 3.1.5 Velocity Relaxation Time

Downstream of a disturbance that creates a relative velocity,  $W_k$  (defined as the difference between the particle velocity,  $V_k = u_{Dk}$ , and the fluid velocity,  $U_k = u_{Ck}$ , that would have existed at the centre of the particle in the latter's absence), the drag force will tend to reduce that difference. Hence it is useful to characterize the rate of equalization of the particle (mass,  $m_p$ , and radius,  $r_p$ ) and fluid velocities by defining a *velocity relaxation time*,  $t_u$ . For gas flows laden with small particles, it is common to assume that the equation of motion can be approximated by just two terms, namely the particle inertia and a Stokes drag, which for a spherical particle is  $6\pi\mu_C r_p W_k$  (Mokhatab, 2006). It follows that the relative velocity decays exponentially with the time constant,  $t_u$ , given by:

$$t_u = m_p / 6\pi r_p \mu_C \quad (3.11)$$

### 3.1.6 Equation for Conservation of Energy

The IPEE may be written as follows:

$$\frac{\partial}{\partial t} (\rho_N \alpha_N e_N^*) + \frac{\partial}{\partial x_i} (\rho_N \alpha_N e_N^* u_{Ni}) = \Theta_N + W_N + \Theta \Xi_N + W \Xi_N + \delta_N \frac{\partial}{\partial x_j} (u_{ci} \sigma_{cij}) \quad (3.12)$$

where  $e_N^*$ , total internal energy density;  $\Theta_N$  rate of heat addition to  $N$  from outside CV;

$\Theta \Xi_N$  Rate of heat transfer to  $N$  within CV including the heat of formation;  $W_N$ , rate of

external *shaft work*;  $W \Xi_N$  Rate of work done to  $N$  by other components in CV.  $\sigma_{cij}$

stresses acting on the component  $N$  on the surface of the control volume

The two terms involving internal exchange of energy between the phases may be combined into an *energy interaction* term given by  $\varepsilon_N = \Theta \Xi_N + W \Xi_N$ . It follows that:

$$\sum_N \Theta \Xi_N = 0 \quad \text{and} \quad \sum_N W \Xi_N = 0 \quad \text{and} \quad \sum_N \varepsilon_N = 0 \quad (3.13)$$

Moreover, the “work-done” term,  $W \Xi_N$ , may clearly be related to the interaction forces  $\chi_{Nk}$ . In a two phase system with one disperse phase we have the following:

$$\Theta \Xi_C = -\Theta \Xi_D \quad \text{and} \quad W \Xi_C = -W \Xi_D = -u_{Di} \chi_{Di} \quad \text{and} \quad \varepsilon_C = -\varepsilon_D \quad (3.14)$$

IPEE equation for each phase or component can be summed to obtain the combined phase energy equation (CPEE):

$$\frac{\partial}{\partial t} \left( \sum_N \rho_N \alpha_N e_N^* \right) + \frac{\partial}{\partial x_i} \left( -u_{Cj} \sigma_{Cij} + \sum_N \rho_N \alpha_N u_{Ni} e_N^* \right) = Q + W \quad (3.15)$$

$$\text{where, } Q = \sum_N \Theta_N \quad \text{and} \quad W = \sum_N W_N$$

Using Eq. (3.14), continuity equation, momentum equation, and the relation:

$$e_N = c_{vN} T_N + \text{constant} \quad (3.16)$$

Between the internal energy,  $e_N$ , the specific heat at constant volume,  $c_{vN}$ , and the temperature,  $T_N$ , of each phase, the thermodynamic form of the Eq.( 3.12) can be written as follows:

$$\rho_N \alpha_N c_{vN} \left\{ \frac{\partial T_N}{\partial t} + u_{Ni} \frac{\partial T_N}{\partial x_i} \right\} = \delta_N \sigma_{Cij} \frac{\partial u_{Cj}}{\partial x_j} + \Theta_N + W_N + \Theta \Xi_N \\ + \chi_{Ni} (u_{Di} - u_{Ni}) - (e_N^* - u_{Ni} u_{Ni}) \Xi_N \quad (3.17)$$

And, summing IPEE, the thermodynamic form of CPEE is:

$$\sum_N \left\{ \rho_N \alpha_N c_{vN} \left( \frac{\partial T_N}{\partial t} + u_{Ni} \frac{\partial T_N}{\partial x_i} \right) \right\} = \sigma_{cij} \frac{\partial u_{ci}}{\partial x_j} - \chi_{Di} (u_{Di} - u_{Ci}) \quad (3.18)$$

$$- \Xi_D (e_D^* - e_C^*) + \sum_N u_{Ni} u_{Ni} \Xi_N$$

In Eqs. (3.17) and (3.18), it has been assumed that the specific heats,  $c_{vN}$ , are constant and uniform.

### 3.1.7 Temperature Relaxation Time

Analogous to the definition of velocity relaxation time,  $t_u$ , the temperatures of the phases might be different downstream of a flow disturbance and consequently there would be a second relaxation time associated with the equilibration of temperatures through the process of heat transfer between the phases. This temperature relaxation time is denoted by  $t_T$  and can be obtained by equating the rate of heat transfer from the continuous phase to the particle with the rate of increase in heat stored in the particle. The heat transfer to the particle can occur as a result of conduction, convection, or radiation. However, for simplicity, we neglect the radiation component.

**Conduction Component:** if the relative motion between the particle and the gas is sufficiently small, the only contributing mechanism is the conduction and it will be limited by the thermal conductivity,  $k_C$ , of the gas (because the thermal conductivity of the particle is usually much greater). Then the rate of heat transfer to a particle (with radius  $r_p$ ) is given by  $2\pi r_p k_C (T_C - T_D)$ , where  $T_C$  and  $T_D$  are representative temperatures of the gas and particle respectively.

Convection Term: To add the component of heat transfer by convection caused by relative motion, we define the Nusselt number,  $Nu$ , as twice the ratio of the rate of heat transfer with convection to that without convection (Mokhatab, 2006). Then the rate of heat transfer becomes  $Nu$  times the above result for conduction. Typically, the Nusselt number is a function of both the Reynolds number of the relative motion,  $Re = 2 W_r r_p / \nu_C$  where  $W_r$  is the typical magnitude of  $(u_{Di} - u_{Ci})$ , and the Prandtl number,  $Pr = \rho_C \nu_C c_{pC} / k_C$ . One frequently used expression for  $Nu$  (Ranz and Marshall 1952) is:

$$Nu = 2 + 0.6 Re^{\frac{1}{2}} Pr^{\frac{1}{3}} \quad (3.19)$$

Assuming that the particle temperature has a roughly uniform value of  $T_D$ , it follows that:

$$\Theta \Xi_D = 2\pi r_p k_C Nu (T_C - T_D) n_D = \rho_D \alpha_D c_{sD} \frac{DT_D}{Dt} \quad (3.20)$$

Where, the material derivative,  $D/Dt$ , follows the particle's temperature. This provides the equation that must be solved for  $T_D$ :

$$\frac{DT_D}{Dt} = \frac{Nu (T_C - T_D)}{2 t_T} \quad (3.21)$$

where,

$$t_T = c_{sD} \rho_D r_p^2 / 3k_C \quad (3.22)$$

Obviously  $t_T$  represents a typical time for equilibration of the temperatures in the two phases and is referred to as the *temperature relaxation time*.

The above general equations are built in the CFD software, so one can predict the flow properties either separately (Eulerian model) or using slip velocity (mixture model). The

results obtained will be used in the hydrate nucleation and growth models which will be discussed in the next chapter.

### **3.2 Technique of Solving Transport Equations (CFD)**

CFD techniques are currently used in industry for design purposes in many different areas (e.g., propulsion, chemistry, combustion, turbo-machinery, etc.). The importance of such techniques for integration of the Navier-Stokes equations is steadily growing because of the fact they improve the design reliability and flexibility. Three main methodologies in the CFD modeling research can be highlighted (Carvero and Satta, 2000) as: a) flexible and robust schemes for steady or unsteady flows for all fluid velocities, b) turbulence modeling ( $k$ - $\epsilon$ ,  $k$ - $\omega$ , Reynolds stress), and c) fluid properties modeling (two phase, real gas, and cryogenics).

At high Reynolds numbers, turbulent fluctuations transport a far greater amount of momentum than viscous forces throughout most regions of the flow. Thus the modeling of the Reynolds stress is a vital part of the flow prediction. A turbulence model is a means of deriving the Reynolds stresses (and other turbulent fluxes) in order to close the mean-flow equations.

Turbulent flow can be modeled by using several schemes. However, the  $k$ - $\epsilon$  model (Pope, 2000) is used here due to its frequent use for industrial applications, its relative accuracy, and its incorporation in the most commercial CFD codes.

The commercial software adopted in our work is built based on the Finite Volume Method. The solver discretizes the mass, momentum and energy equations in integrated form. The general form of the transport equation is:

$$\int_{\Delta t} \frac{\partial}{\partial t} \left( \int_{CV} \rho \phi dV \right) dt + \int_{\Delta t} \int_A n \cdot (\rho \phi u) dAdt = \int_{\Delta t} \int_A n \cdot (\Gamma \text{grad} \phi) dAdt + \int_{\Delta t} \int_{CV} S_{\phi} dV dt \quad (3.23)$$

Equation (3.23) is used as the starting point for computational procedures in the finite volume method. By setting  $\phi$  equal to 1,  $u$ ,  $v$ , and  $T$  and selecting appropriate values for the diffusion coefficient  $\Gamma$  and the source term  $S_{\phi}$ , the mass, momentum and energy equations are obtained.

The governing equations are transformed into algebraic equations for every cell. The discrete equation for 2D becomes:

$$a_P \phi_P = a_w \phi_W + a_e \phi_E + a_s \phi_S + a_n \phi_N + b \quad (3.24)$$

$$a_P = a_w + a_e + a_s + a_n - b \quad (3.25)$$

Where,  $a$  stands for the coefficient of the property  $\phi$  (diffusion, advection, etc.) and  $b$  is the source term coefficient.

## CHAPTER 4

### Hydrate Nucleation, Growth and Distribution

In principle, the problem of finding the size distribution function for hydrate is sufficiently hard both from physical and mathematical prospective. In this chapter, we endeavour to confine our consideration to a derivation of a formula for size distribution function which satisfies the Law of Mass Action. Two nucleation models are proposed and compared in this work, the first model is based on mass transfer alone while the second is based on both mass transfer and hydrate formation reaction kinetics. A comparison between the two models in terms of growth rate is also presented in this chapter.

#### 4.1 Review

The basic behaviours of flowing particles such as deposition, transport, lifetime, and optical influence, depend strongly on their size, their chemical composition, and on the nature of the carrier gas.

Among considerable work reported in the literature concerned with the Particle Size Distribution PSD, Den Ouden and Thomson (1991) proposed a simplified form of population balance which could not address several key issues related to the full precipitation problem. Tandon and Rosner (1996) measured the deposition rate using the influence of the particle size distribution. Wachi and Johns (1991) studied precipitation effects in gas/liquid mass transfer by means of population balances.

In his study on aerosol particles in the early 1950's, Junge (1963) found in measurements that atmospheric aerosol particles had the interesting property that the mass was almost uniformly distributed in equal geometric intervals. Then he derived the Junge distribution function as follows (1963):

$$n = \frac{dN}{d \log r} = Cr^{-\alpha} \quad (4.1)$$

Where,  $N$  is the particle number concentration,  $C$  is a constant,  $r$  is the particle radius, and  $\alpha$  is an adjustable constant in the range between 2.2 and 4.0.

The Junge distribution was proved to be very good for dispersed particles, especially for particles with radii larger than 0.1  $\mu\text{m}$ . Because of the limitation of the development of aerosol technology to measure particles with sizes smaller than 0.1  $\mu\text{m}$  in 1950's, Junge could not find a suitable size distribution function to describe fine size particles. Usually particles in fine size region have bimodal and other distribution shapes because of the strong interactions among them such as coagulation and diffusion collision.

The present chapter starts with explaining the phenomena of hydrate nucleation, which is mainly affected by mass transfer and reaction kinetics. The value of each term will be evaluated and discussed, followed by presenting a mathematical model for particle distribution ( $n$ ) based on conservation of mass. The influence of saturation and gas-particles relative velocity on the growth rate is also discussed. Finally the discussion concludes with a comparison between the results of the two proposed models in expressing the distribution of the particles with time and size growth rate.

## 4.2 Theory

### 4.2.1 Mass Transfer

The mass transfer rate between the particle and the gas medium can be expressed by the mass transfer rate equation on the particles:

$$\dot{m} = 4\pi r_p^2 m_v (J_+ - J_-) \quad (4.2)$$

Where,  $J_+$  stands for the flow rate of vapour molecules direct towards the particle and  $J_-$  is the outward flow rate from the particle surface;  $m_v$  is the mass of a single molecule of vapour. The solution of the equation depends significantly on Knudsen number. For the case of continuum region  $Kn \ll 1$ , the net molecule flow rate  $J = J_+ - J_-$  obeys the Fick's law:

$$J = -D_v \frac{dz}{dr} \quad (4.3)$$

Where,  $z$  is the molecule number density ( $\rho = m_v z$ );  $D_v$  is the molecule diffusivity of vapour in a fluid media. With boundary conditions  $z(r) = z_s$  at  $r = r_p$  and  $z = z_\infty$  at  $r = \infty$ , we obtain the solution of the mass transfer equation:

$$\dot{m} = 4\pi D_v r_p (\rho_\infty - \rho_s) \quad (4.4)$$

Since the particles move in a gas flow, the moving flow around the particles cause an increase in mass transfer as a result of the 'forced' convection besides the 'free' diffusion convection. Eq. 4.4 is valid for free diffusion convection and needed to be modified for the consideration of relative movement between particles and gas medium. Therefore, by introducing particle Sherwood number ( $Sh$ ), Eq. 4.4 becomes:

$$\dot{m} = 2\pi D_v r_p Sh (\rho_\infty - \rho_s) \quad (4.5)$$

When the system under free diffusion convection, Sherwood number is ( $Sh = 2$ ), and Eq. 4.5 becomes identical to Eq.4.4.

For forced diffusion convection, a following new modified expression based on experimental data is considered (Kulmala and Vesala, 1995):

$$Sh = 2.009 + 0.514 Re_p^{1/2} Sc^{1/3} \quad (4.6)$$

Where,  $Re_p$  is the particle Reynolds number:

$$Re_p = \frac{2|\mu_r|r_p}{\nu_g} \quad (4.7)$$

$\mu_r$  is the gas-particle relative velocity;  $\nu_g$  is the kinematics viscosity of the carrier gas.

#### 4.2.2 Model of Homogenous Nucleation and Droplet Growth (Model I):

The saturation ratio defined in multi-component mixture as the ratio of actual molar fraction of component  $k$  in the vapour phase ( $y_v$ ) and the equilibrium molar fraction ( $y_{eqv}$ ).

$$S = \frac{y_{vk}}{y_{eqvk}} \quad (4.8)$$

and its value of a solution at the temperature  $T$  can be estimated using the following formula:

$$S = 1 + \frac{\Delta H_s (T_{eq} - T)}{\bar{R}T^2} \quad (4.9)$$

Where,  $\Delta H_s$  is the heat of solution (for hydrate  $13.26 \times 10^3$  J/mole), (Max and Pellenbarg, 1999),  $\Delta T$  is the super-cooling and  $\bar{R}$  is the gas constant (8.314 J/mole K).

Using saturation ratio ( $S$ ) as a driving force, the critical radius is defined as:

$$r_c = \frac{2\sigma}{\rho_L R_v T \ln(S)} \quad (4.10)$$

Where,

$\rho_L$  : Liquid density

$R_v$  : Specific gas constant

The droplet growth is governed by diffusion and the change in droplet size over time is represented by:

$$\left(\frac{dr_p}{dt}\right) = n_v \left(\frac{Sh D_v MW}{\rho_L}\right) \frac{(y - y_{eq})}{2r_p} \quad (4.11)$$

Where,

$Sh$  : Sherwood number for mass transfer (Eq. 4.6)

$MW$  : Molar mass

$n_v$  : Vapour molar density

Pressure and temperature dependence diffusivity coefficient is considered in the present work. The following equation for estimating the rate of diffusivity has been developed from a combination of kinetic theory and corresponding states arguments (Bird *et al.*, 2002):

$$D_{AB} = \frac{a}{P} \left(\frac{T}{\sqrt{T_{cA} T_{cB}}}\right)^b (P_{cA} P_{cB})^{1/3} (T_{cA} T_{cB})^{5/12} \left(\frac{1}{MW_A} + \frac{1}{MW_B}\right)^{1/2} \quad (4.12)$$

Where,  $D_{AB}$  is the binary diffusivity in (cm<sup>2</sup>/s),  $P$  is the pressure in (atm),  $T$  is the temperature in (K).

Analysis of experimental data gives the dimensionless constants  $a$ ,  $b$  as follows (Bird *et al.*, 2002):

For nonpolar gas pair:  $a = 2.745 \times 10^{-4}$ ;  $b = 1.823$

For pairs consisting H<sub>2</sub>O and a nonpolar gas:  $a = 3.640 \times 10^{-4}$ ;  $b = 2.334$

#### 4.2.3 Model of Reaction Kinetics combined with Mass Transfer (Model II):

The kinetics of the hydrate formation reactions can be written as (Clarke and Bishnoi, 2000; Clarke and Bishnoi, 2001; Englezos *et al.*, 1987a,b; Kim *et al.*, 1987):

$$r^m = kA_s(f - f_{eq}), \quad (4.13)$$

Where,  $r^m$  (mol/m<sup>3</sup> s) is the consumption rate of methane;  $k$  (mol/m<sup>2</sup> Pa s) is the kinetic constant of hydrate formation or dissociation;  $A_s$  (m<sup>2</sup>/m<sup>3</sup>) is the reaction surface area, which is essentially the interface area between hydrate particles and the surrounding phases;  $f$ (Pa) is the fugacity of methane under the local temperature and pressure;  $f_{eq}$ (Pa) is the methane fugacity at the equilibrium pressure corresponding to the local temperature.

For hydrate dissociation, the kinetic constant  $k$  is written in an Arrhenius-type equation as (Kim *et al.*, 1987):

$$k = k_0 \exp\left(-\frac{\Delta G^*}{RT}\right) \quad (4.14)$$

Where,  $k_0$  is the intrinsic kinetic constant and  $\Delta G^*$  is the activation energy. For sl methane hydrate in a bulk phase system without salt,  $k_0 = 3.6 \times 10^4$  mol/m<sup>2</sup> Pa s, and  $\Delta G^*/R = 9752.73$  K, as measured by Clarke and Bishnoi (2001). Measurement of kinetic

constant for hydrate formation is more difficult than for dissociation. Englezos *et al* (1987a) measured the value of formation of sI methane hydrate from methane gas and aqueous-phase. The results exhibited an ambiguous dependence on temperature. In our analysis, we assume that the kinetic constant for hydrate formation is constant and its default value takes the average of the results measured by Englezos *et al.*' (1987a) which is  $0.5875 \times 10^{-11} \text{ mol/m}^2 \text{ Pa s}$ .

The determination of reaction surface  $A_s$  in Eq. (4.13) has been numerously proposed in the literatures. Among those were: Yousif *et al* (1991) ; Masuda *et al* (2002); and Sun *et al* (2006). For simplicity, the model of Masuda *et al.*, which estimated the average surface area to be approximately  $3.75 \times 10^5 \text{ m}^2/\text{m}^3$ , is adopted in this research.

Eq. (4.13) can be manipulated to determine the rate of growth due to nucleation process:

$$\frac{dr_p}{dt} = \frac{kA_s MW(f - f_{eq})}{3000\rho_p} r_p \quad (\text{m/s}) \quad (4.15)$$

Where,  $MW$  is the molecular weight of the gas (g/mol);  $\rho_p$  density of the gas hydrate particle ( $\text{kg/m}^3$ ). For sI methane hydrate, Eq. 4.15 becomes:

$$\frac{dr_p}{dt} = 1.2689 \times 10^{-11} (f - f_{eq}) r_p \quad (4.16)$$

Where,  $f$  and  $f_{eq}$  are in (Pa).

Combining Eqs (4.11) and (4.15), the final expression of the hydrate growth rate as a result of mass transfer and kinetic reaction is:

$$\frac{dr_p}{dt} = \frac{kA_s MW(f - f_{eq})}{3000\rho_p} r_p + \left( \frac{n_v (Sh)(D)MW}{\rho_L} \right) \frac{(y - y_{eq})}{2r_p} \quad (4.17)$$

**Assumptions:**

- The growth rate due to kinetic reaction is independent of the surface area
- The particle-gas relative velocity is small
- For methane fugacity and other gas properties calculations, ideal gas has been assumed at this stage for simplicity.

**4.3 Size Distribution model:**

The growth equation can be expressed as (Brock, 1983):

$$\frac{\partial n(v,t)}{\partial t} + \frac{\partial}{\partial v}(I_v(v,t)n(v,t)) = \Lambda_p(v,t) \quad (4.18)$$

Where,  $n(v,t)$  is the particle size distribution function defined as the number of particles per unit volume, with particle volumes is in the range  $(v, v + dv)$  at time  $t$ .  $I_v(dv/dt)$  is the growth rate of particle volume.  $\Lambda_p(v,t)$  is the 'source' rate accounting for emission and other particle sources as well as sinks. In this study, we can neglect the source term since there is no external sources or sinks of particle.

Defining  $I_r = (dr_p / dt)$  as the radius growth rate of a single particle ( $I_v = 4\pi r_p^2 I_r$ ), and

using the approximation:  $I_r = \frac{I_m}{4\pi r_p^2 \rho_p}$ ,  $I_m = (dm_p / dt)$ , Eq. (4.18) can be written as:

$$\frac{\partial n(r_p,t)}{\partial t} + \frac{\partial}{\partial r_p}(I_r(r_p,t)n(r_p,t)) = 0 \quad (4.19)$$

### 4.3.1 Solution of Mass Transfer Model:

Simulating the evolution of the particle size distribution with time along the pipe can be obtained through introducing Eq. (4.11) into Eq. 4.19.

Eq. 4.11 for single component can be written as:

$$\frac{dr}{dt} = \frac{\beta_1}{r} \quad (4.20)$$

$$\text{Where, } \beta_1 = \left( \frac{n_v (Sh)(D_v) MW}{2\rho_L} \right) (y - y_{eq}) \quad (4.21)$$

Sherwood number is a function of the particle Reynolds number which in turn is a function of gas-particle relative velocity and particle radius as shown in Eq.4.6. However, since the particle relative velocity is relatively low, we assumed in our analysis that the Sherwood number is non-size dependant. This assumption is reasonable especially in the tiny particle which its average radius is of order  $10^{-8}$  m while the particle relative velocity ( $u_r$ ) considered in our model is relatively small ( $\sim 5$  m/s) and the gas viscosity is of order  $10^{-6}$ .

Combining Eqs. 4.19 and 4.20, the deferential equation for size density would be:

$$\frac{\partial n}{\partial t} + \frac{\partial}{\partial r_p} \left( \frac{\beta_1}{r} n \right) = 0 \quad (4.22)$$

and the solution of Eq. 4.22 (details are in discussed in Appendix A):

$$n(t, r) = n_0 \frac{r}{r_c} \exp \left( \frac{1}{2r_c^2} (2\beta_1 t - r^2) \right) \quad (4.23)$$

Where,  $n_0$  is the concentration of sites in the system, on which the clusters of the new phase can form (particle per  $m^3$ ).

Introducing the following parameters in Eq. (4.23):

$$\text{Particle Fourier number: } Fo = \frac{\beta_1 t}{r_c^2} \quad (4.24)$$

$$\text{Reduced radius: } r^* = \frac{r}{r_c}, \quad (4.25)$$

Eq. (4.23) becomes:

$$n^*(t, r) = 1.65r^* \exp\left(Fo - \frac{r^{*2}}{2}\right) \quad (4.26)$$

Where, a dimensionless parameter:  $n^* = \frac{n}{n_0}$ ,

#### 4.3.2 Solution of Model of Reaction Kinetics with Mass Transfer:

Using Eq. (4.17), the general size distribution function can be written as:

$$\frac{dr_p}{dt} = \frac{\beta_1}{r_p} + \beta_2 r_p \quad (4.27)$$

$$\text{Where, } \beta_2 = \frac{kA_s MW(f - f_{eq})}{3000\rho_p} \quad (4.28)$$

One can now simulate the evolution of the particle size distribution with time.

Substituting Eq (4.27) into Eq. (4.19), the deferential equation for size density would be:

$$\frac{\partial n}{\partial t} + \left(\beta_2 r + \frac{\beta_1}{r}\right) \frac{\partial n}{\partial r} + \left(\beta_2 - \frac{\beta_1}{r^2}\right) n = 0 \quad (4.29)$$

and the solution of Eq.4.29 would be:

$$n(t, r) = \frac{n_0 \beta_1 r}{r_c (\beta_2 r^2 + \beta_1)} \exp\left(\frac{\beta_1}{r_c^2} t\right) \quad (4.30)$$

Again by introducing Eqs. 4.24 and 4.25, Eq. 4.30 becomes:

$$n^*(Fo, r^*) = \frac{\beta_1}{\beta_2 r_c^2} \frac{r^* \exp(Fo)}{(r^{*2} + \beta_1 / \beta_2 r_c^2)} \quad (4.31)$$

Details of the solution of Eq. (4.29) are presented in Appendix-B.

#### 4.4. Analysis and Discussion:

In the present study, the classical nucleation theorem is applied to hydrate formation in a saturation gas flow. The analysis here begins with the investigation on the growth rate of particles in each model, followed by studying the influence of the saturation and particle-gas relative velocity on the radius growth rate. Then the comparison of particle size distribution results for the two models is presented.

##### 4.4.1 Growth of particle radii (Model I)

Due to the mass transfer between the gas (and water vapour) and solid particles, nucleation could occur. However, the formed hydrate particles may melt if the driving force is vanished. In turn, when the flow is still under driving force, the particles grow and reach the critical size; such particles are stable and will stay in the solid form even though the driving force is eliminated. As mentioned earlier, the driving force of the first model used in our analysis is the supersaturation of the gas. Figure (4.1) shows the growth of the particle radius as a function of time. The relation reveals that the radius grows exponentially with the time. In contrast the speed of the particle growth decreases with the time as shown in Figure (4.2). Thus, Small size particles grow much more

quickly compared to large size particles. In other word, the particle growth decelerates as the particle becomes large (see Figure 4.3). Therefore, the nuclei starts forming rapidly and as its size develops, the growth rate becomes slow.

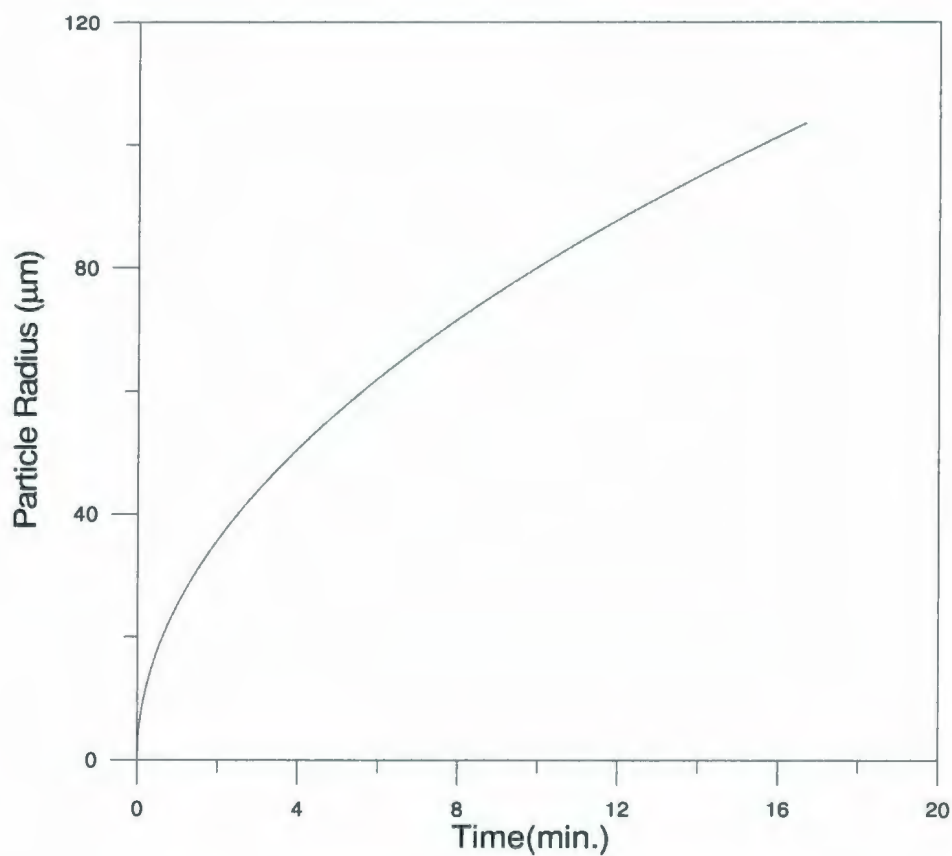


**Figure (4.1)** Growth of hydrate particles (Model I)

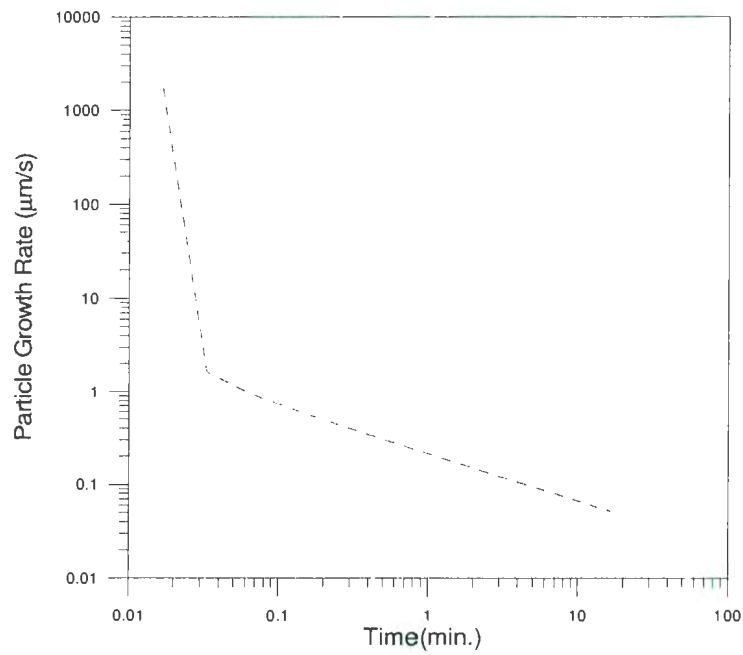


**Figure (4.2)** Development of hydrate particle growth rate (Model I)

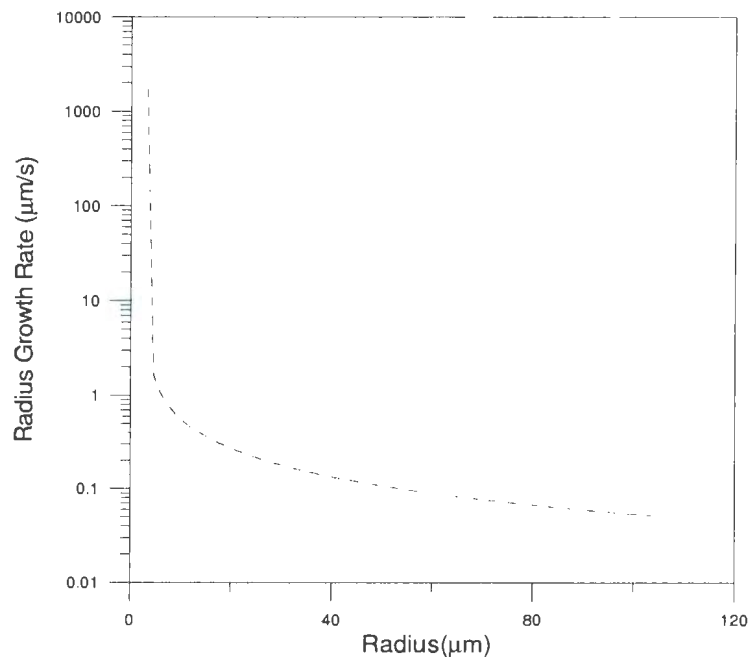


**Figure (4.3)** Hydrate growth rate vs. particle radius (Model I)

#### 4.4.2 Growth of particle radii (Model II)

Since the particle growth in the process of hydrate formation is affected by the reaction kinetics, time, as well as mass transfer, a second driving force, the fugacity of the gas, takes a part in the particle growth process. The influence of the reaction time appears after the particle reaches the critical size as shown in Figure (4.4). While the significance of the mass transfer diminishes as the particle size grows, the reaction kinetics however dominates the process of hydrate formation. Figure (4.5) shows the trend of the reaction and condensation terms as a function of particle radii. One can conclude that the effect of condensation decreases reciprocally and almost vanishes as the size of the particle becomes relatively larger. In turn, the reaction rate starts to control the growth process and even becomes the sole effective driving force in the particle growth process.

The existence of kinetic reaction in the process of nucleation decelerates the particle rate, causing a delay in the particle evolution as illustrated in Fig. (4.6).

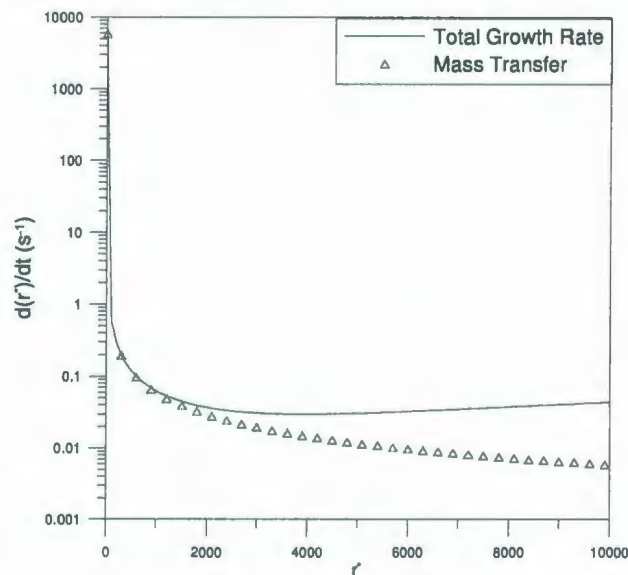


**Figure (4.4)** Effect of hydrate formation reaction kinetics on particle growth rate

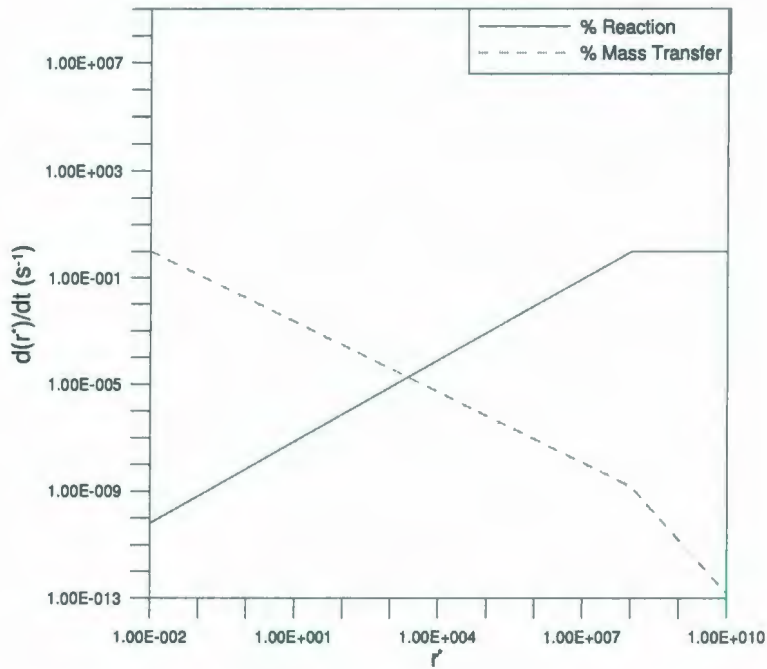


**Figure (4.5)** Percentage of participation of kinetics and mass transfer terms in particle growth with particle size

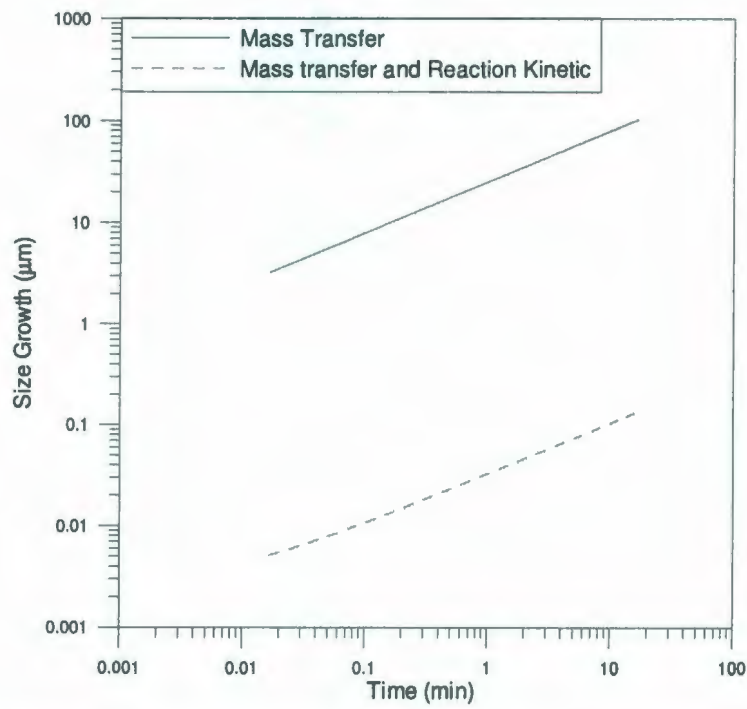


**Figure (4.6)** Delay in size growth due to reaction kinetic process

#### 4.4.3 Effect of Saturation

The supersaturation ratio ( $S$ ), the ratio of actual molar fraction of a component in the vapour phase and the equilibrium molar fraction, is an important parameter which influences the free energy change, critical radius, and critical energy at a fixed temperature (Sakrani *et al*, 2005). The effect of saturation has been studied in this work. The result reveals the very significant rule that the larger the supersaturation ratio,  $S$ , the smaller is the critical radius  $r_c$ . This could attribute to the fact that as the supersaturation ratio increases, it will raise the molecular bombardment rate and reduce both the critical radius  $r_c$  and the attendant height of the activation energy barrier  $\Delta G^*$  to such extent that the probability of some sub-critical embryo fortuitously growing to supercritical size in a short time approaches unity (Abraham, 1974).

Figure (4.7) illustrates the particle size as a function of time for various saturation values. The graph concludes that the particle grows faster in a short period of time when the saturation ratio increases. Further, an increase in the saturation ratio results in a significant deviation in the particle growth rate as illustrated in Figures (4.8a) and (4.8b). In fact, higher saturation ratios enhance the growth rate by improving the diffusion process.

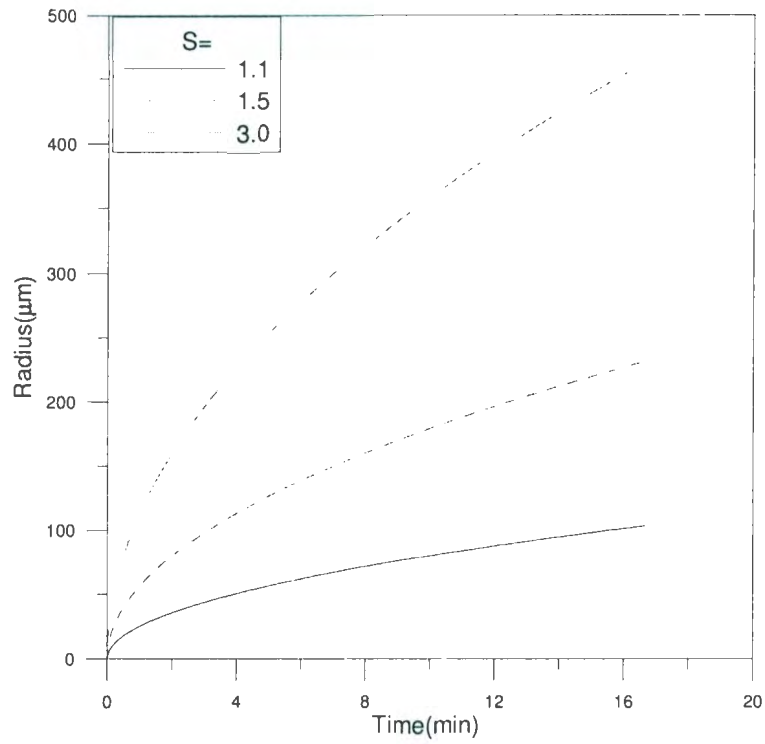
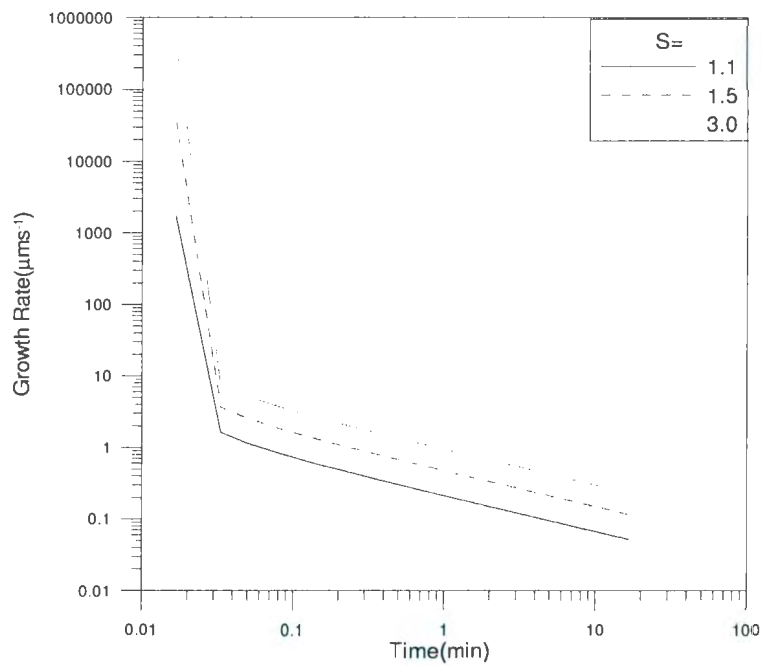
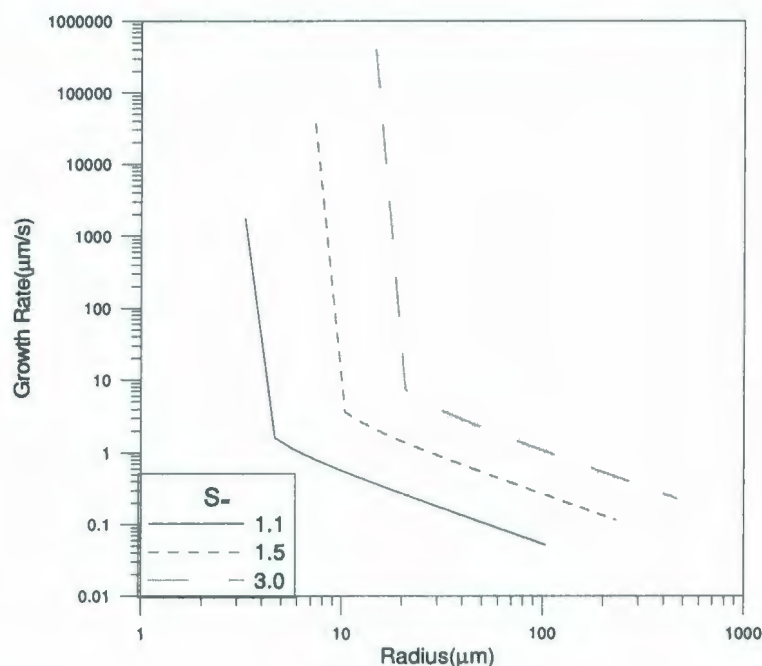


Figure (4.7) Influence of saturation ratio on hydrate particle size growth



(a)



(b)

**Figure (4.8)** Effect of saturation ratio on hydrate growth development: a) with time, b) with particle radius

#### 4.4.4 Effect of Relative Velocity

The gas-particle relative velocity is studied and analyzed in the present work. Figure (4.9) shows the particle radii growth at different relative velocities. The relative velocity works as a driving force and increases the particle growth rate. This could be attributed to the increase in the mass transfer since the relative velocity results in inducing the convective mass transfer, assists the diffusion, and therefore accelerates the mass transfer.

The relative velocity shows no significant effects on the particle growth rate for very small particle sizes, however, the influence of the relative velocity can clearly appear at relatively larger sizes as shown in Figure (4.10). Such behaviour could be explained by the fact that the particle Reynolds number required for the convective mass transfer

process becomes more significant as the size of the particle increases. Figure (4.11) represents the growth rate as a function of the particle size for various relative velocities. Again the growth rate becomes faster when the relative velocity increases.

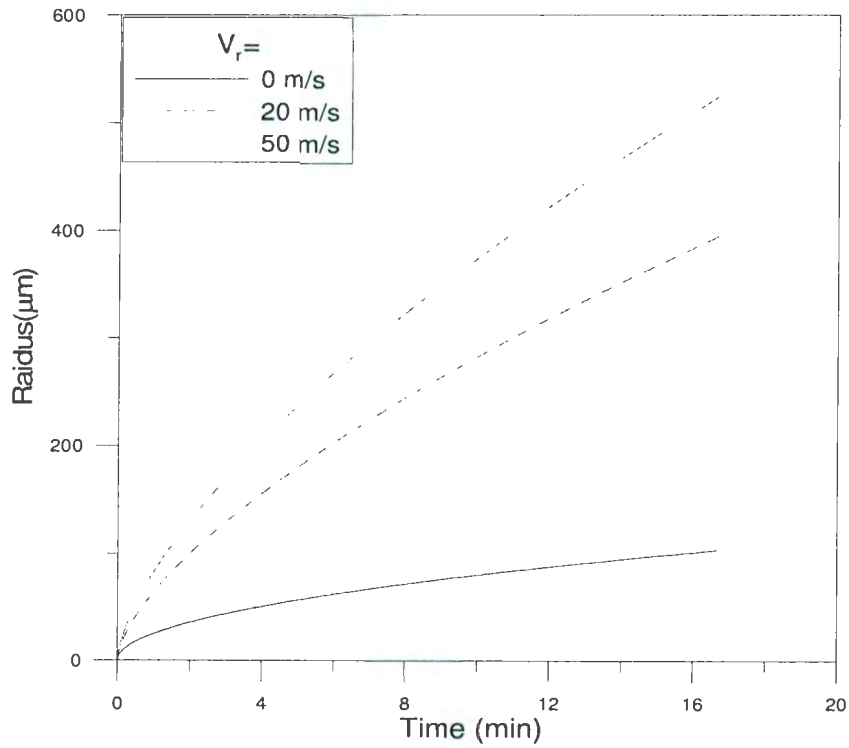


**Figure (4.9)** Influence of relative velocity on hydrate particle size growth

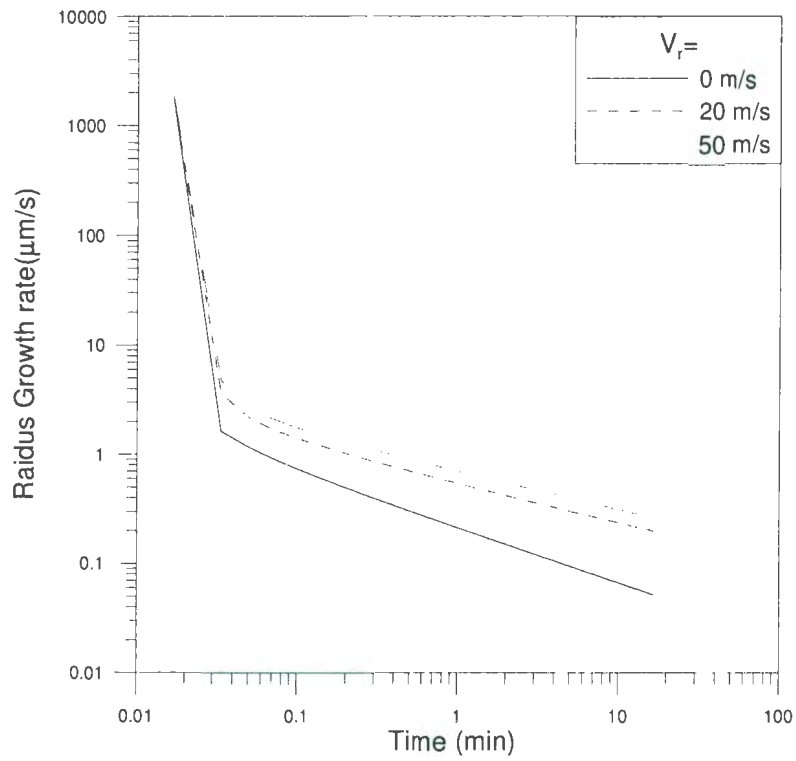


**Figure (4.10)** Effect of relative velocity on hydrate growth rate verses time

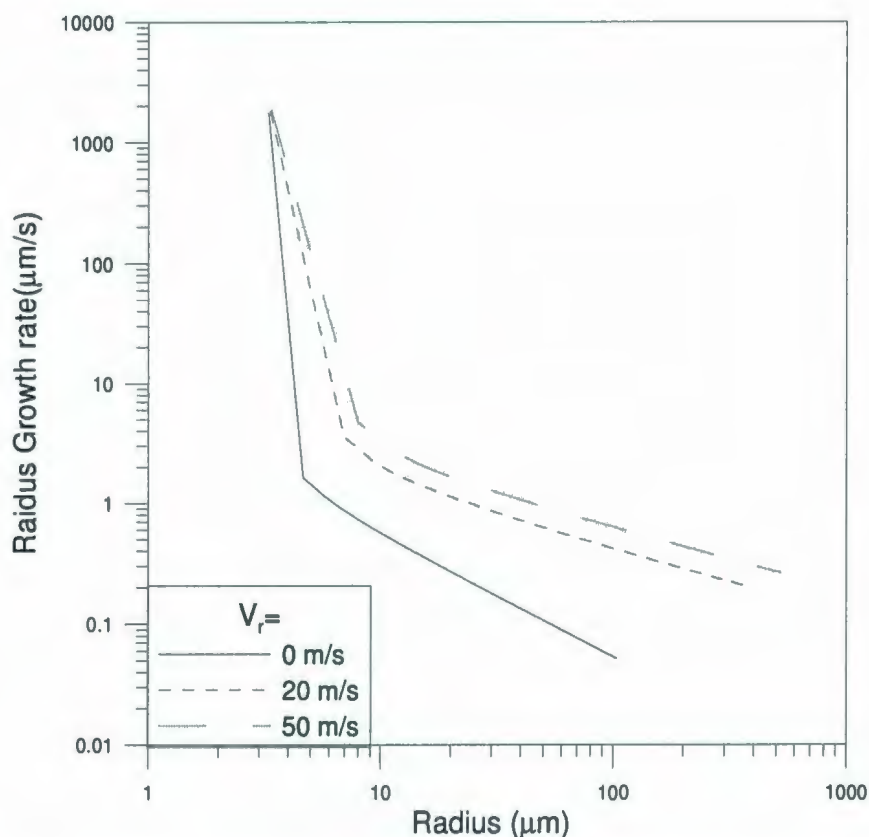


**Figure (4.11)** Effect of relative velocity on hydrate growth rate verses particle size

Aldaco *et al* (2007) performed experimental studies on the crystallization process in fluidized bed reactors. They were interested in the influence of the saturation ratio and the relative velocity of particles on the particle growth rate. Their experimental results support the modeling proposed in this thesis in that the increase in the relative velocity and supersaturation gives rise to an increase in the particle growth rate. This conclusion was also observed by Yang (1999), who simulated the growth of aerosol condensing particles and came up with identical trends. He also found that the relative velocity between the particles and the fluid have a noticeable influence on the growth rate for the particles with radii larger than 1.0  $\mu\text{m}$ . The results of the influence of supersaturation and

relative velocity presented in this thesis are in agreement with the conclusions of Aldaco *et al* (2007) and Yang (1999).

#### 4.4.5 Size distribution

Particles suspended in a gas - the gas being either confined in an enclosed space or flowing in a conduit or through equipment - are in a state of constant motion. The particle motion generates a change in size distribution as a result of diffusivity, gravity, and thermal activity. Other processes responsible for changes in size distribution are condensation, which occurs on the existing particles (particle growth), and nucleation, which occurs to generate entirely new particles (Nadkarni and Mahalingam, 1985). The impacts of condensation and reaction kinetics on the particles distribution are of interest in the present work.

In Section 4.3 we derived an analytical expression for particle size distribution based on mass balance for two cases: condensation alone and condensation with reaction. In this section we compare the results of both models and discuss the significance of parameters in each model. Figure (4.12) demonstrates the particle size distribution as a function of particle radius ( $r_p$ ) for both cases. The plot shows quantitatively the impact of reaction kinetics on the population equation. The impact increases the domain of particle sizes that are instantaneously formed.

The behaviour of size distribution in each case remains unchanged with the time as shown in Figure (4.13). In fact both cases have the same exponential term in their

expression, (see Eqs. 4.23 and 4.30), which means no discrepancies in the behaviour of the particles population with time. However, in the case of Model II, the number of particles definitely increases as a result of the second driving force term.

Finally, Figure (4.14) illustrates the number of particles formed as a function of time for various particle sizes. The graph shows that the number of particles with larger sizes is always fewer than that of very small sizes because the very small particles form and grow faster than large particles. This conclusion is in agreement with numerous literature reports concerning the particle size distribution; see for instance papers by Sakrani (2005) and Abraham (1974).

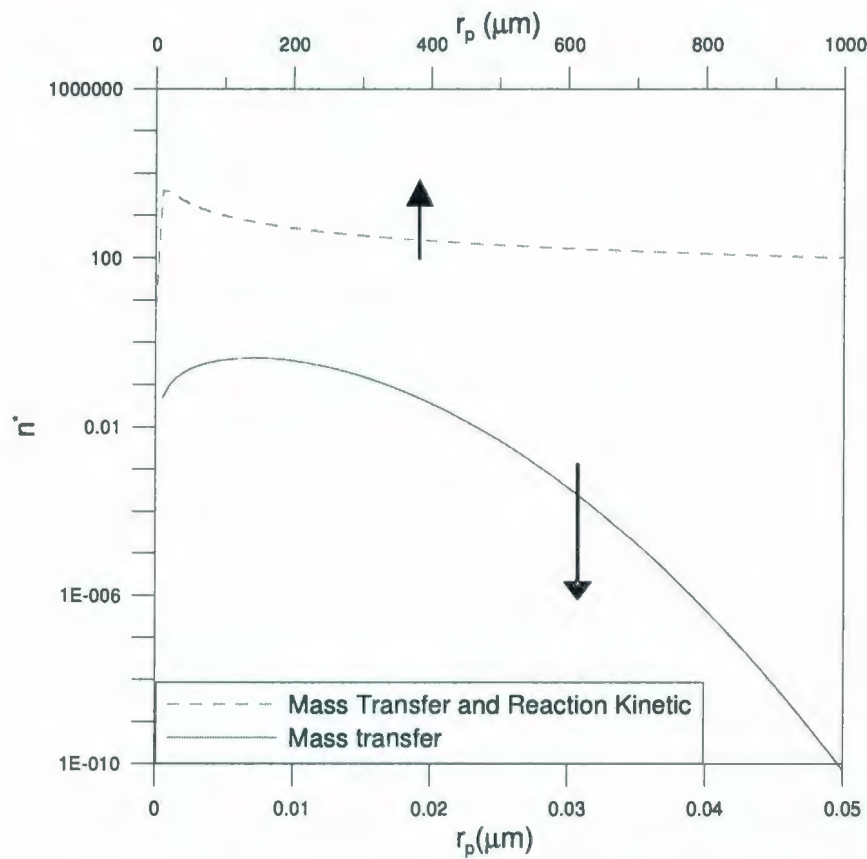


**Figure (4.12)** Hydrate particle distribution as a function of size

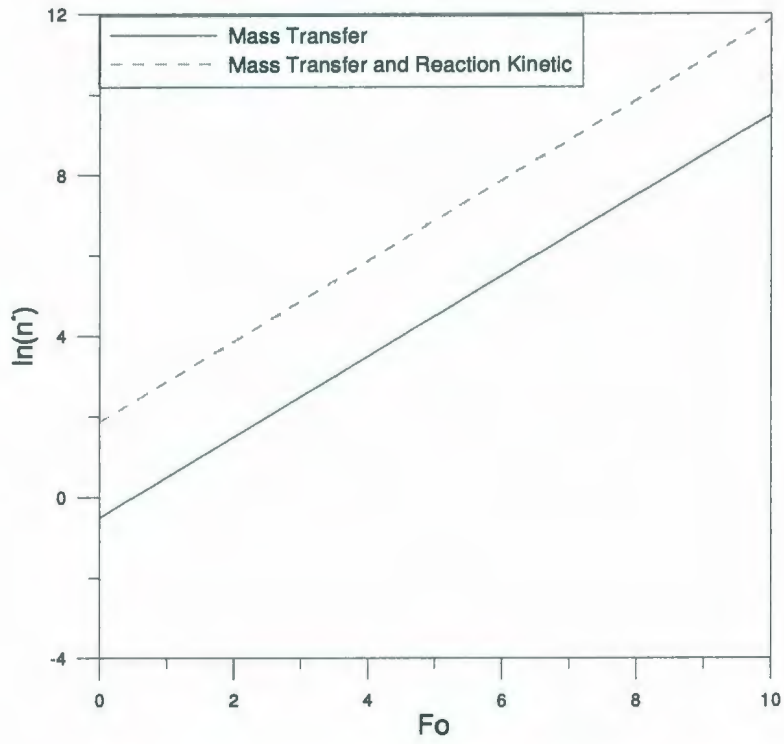


**Figure (4.13)** Distribution of Hydrate particles vs. time

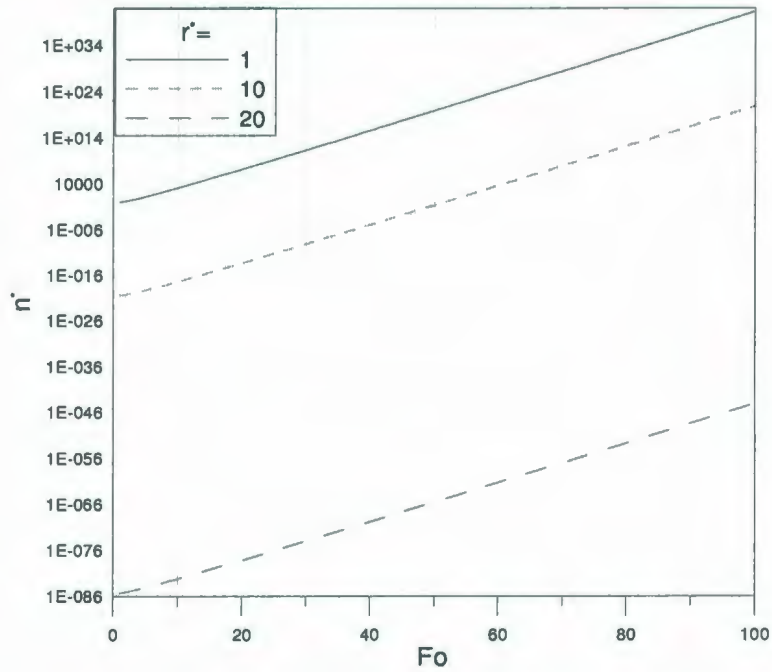


**Figure (4.14)** Number of hydrate particles appearance with time for different radius

#### 4.5. Conclusion

New nucleation and distribution models including mass transfer and kinetics of reaction were applied to model the hydrate formation and deposition process. Analytical expressions were derived for the case of formation and growth as a result of mass transfer alone and for the case of both mass transfer and reaction. A comparison between the results of the proposed models was made. Influence of saturation and relative velocity on the growth process was also proposed.

The main conclusions can be summarized as follows:

- The supersaturation ( $S$ ) forces the particle growth rate to be fast and decreases the critical radius.
- The particle-fluid relative velocity works as a driving force and increases the particle growth rate.
- The growth rate due to mass transfer decreases as the size of the particle increases.
- The hydrate formation reaction kinetics changes the trend of the growth rate as a result of saturation.
- Mass transfer is the dominant factor in the beginning of the nucleation process then the reaction kinetics becomes the controlling factor in the growth process.
- Particle size distribution (PSD) is also influenced by the reaction kinetics. The modeling results showed that particles with a wider size distribution form when reaction kinetics is taken into account.

- The dependence of PSD to time for both cases (i.e., modeling only with mass transfer vs. modeling considering the reaction kinetics) is identical although the number of particles per unit volume of the container is different.

## CHAPTER 5

### Forces Applied to a Single Particle

The Lagrangian equations governing the position  $X_i$  and velocity  $u_{pi}$  along the trajectory of each spherical particle, of diameter  $d_p$  and mass  $m_p$  in the carrier flow field can be written as

$$\frac{dX_i}{dt} = u_{pi} \quad (5.1)$$

$$m_p \frac{du_{pi}}{dt} = -F_i \quad (5.2)$$

Where,  $F_i$  denotes the summation of all forces acting on the particle. It is vital first to identify all forces acting on a moving particle that is immersed in a flowing fluid. These forces can be divided into four categories:

- (1) Forces that act on a particle due to the motion of particle such as the Basset force (the force associated with past movements of the particle), virtual mass (added mass), and Magnus force (the force perpendicular to the forward motion on a spinning object moving through a fluid or gas) (Amiri *et al*, 2006).
- (2) Forces that act on a particle due to the motion of the surrounding fluid such as drag and lift forces.
- (3) Forces that act on a particle regardless of whether the particle is in motion or is immersed in a flowing fluid, i.e., body forces, such as gravity.
- (4) Forces that act on any object immersed in fluid, regardless of either particle or fluid motion such as buoyancy forces.

As the diameter of the hydrate particles in the situation of interest in this research is much smaller than the carrier pipe radius and its density is much greater than that of the carrier fluid, the particle equation of motion can be reduced to an equation consisting only of the drag and gravitational forces (Crowe, 2006). Therefore, for such a particle, the Basset and virtual added mass forces can be neglected (Burry and Bergeles, 1993). For a particle with a Reynolds number higher than the Stokes limit, a lateral force, called lift force, may exist due to the asymmetric pattern of flow around the particle. If the particle does not rotate, only slip-shear lift is caused by the shear of the surrounding fluid, which makes the pressure distribution around the particle inconsistent and generates the so-called the Saffman lift force (Saffman, 1968). Another transport phenomenon associated with the interaction of small particles with fluid molecules is the Brownian motion. The Brownian motion results when high-momentum molecules in the fluid collide with small particles in suspension.

The following section demonstrates the forces that act on the flowing particle:

### **5.1 Pressure Gradient Force**

An additional force on the particle, which may be included in the calculation, is the force due to pressure variation across the particle. The formula takes the form:

$$F_p = -2\pi r_p^3 \nabla p \quad (5.3)$$

Where,  $p$  is the pressure in the continuous phase. This force is small for particles with densities much higher than the continuum fluid and may be excluded in the modeling of the hydrate particle movement.

## 5.2 Buoyancy Force

The next force holding a particle to a surface to be considered is the net weight. For a density difference  $\Delta\rho = \rho_p - \rho_f$  between particle and fluid the net weight (that is, buoyancy-corrected) is:

$$F_b = (\pi/6)\Delta\rho g d^3 \quad (5.4)$$

The buoyancy effects have been neglected in the analysis since the particle density is much more than gas density (Crowe, 2006).

## 5.3 Drag Force

Since the particles in gas flow have diverse sizes, they obtain different accelerations as a result of their different inertias. The general expression for the drag force  $F_D$  on a spherical particle in a gas of constant velocity can be written as:

$$F_D = \frac{1}{2} \pi r_p^2 \rho_f |u_p - u_g| (u_p - u_g) \frac{C_D}{C_c} \quad (5.5)$$

Where,  $C_c$  Cunningham non-continuum correction, defined as:

$$C_c = 1 + \frac{\lambda}{d_p} \left[ 2.34 + 1.05 \exp\left(-0.39 \frac{d_p}{\lambda}\right) \right] \quad (5.6)$$

Case I: Stoke's Regime ( $Re_p < 0.1$ )

$$F_D = \frac{6\pi\mu_g r_p u_p}{C_c} \quad (5.7)$$

Case II: for other values of  $Re_p$ :

$$F_D = \frac{C_D Re_p}{24C_c} (6\pi\mu_g r_p (u_p - u_g)) \quad (5.8)$$

Where,  $\mu_g$  is the dynamic viscosity of the gas;  $Re_p$  is the particle Reynolds number defined as

$$Re_p = \frac{2|u_p - u_g|r_p}{\nu_g}; \text{ and } \nu_g \text{ is the kinematics viscosity of the gas.}$$

The drag coefficient is obtained from the following piecewise expression depending on the particle Reynolds number:

$$C_D = \frac{24}{Re_p} \quad Re_p < 0.1 \quad (5.9a)$$

$$C_D = \left( \frac{24}{Re_p} \right) \left[ 1 + \frac{3Re_p}{16} + \frac{9Re_p^2}{160} \ln(2Re_p) \right] \quad 0.1 < Re_p < 2 \quad (5.9b)$$

$$C_D = \left( \frac{24}{Re_p} \right) [1 + 0.15 Re_p^{0.687}] \quad 2 < Re_p < 500 \quad (5.9c)$$

$$C_D = 0.44 \quad 500 < Re_p < 2 \times 10^5 \quad (5.9d)$$

### 5.3.1 Slip Correction Factor

Correlation of the drag force which obeys the Stokes's law assumed that the relative velocity of the gas right at the surface of the sphere is zero. However, this assumption is not met for small particles whose sizes approach the mean free path of the gas. Such particles settle faster than those predicted by the Stokes's law since there is the "*slip*" at the surface of the particle and often the error becomes more significant for particles less than 1  $\mu\text{m}$  in diameter. In 1910, Cunningham (Hinds, 1999) derived a correction factor for the Stokes's law to account for the effect of *slip*. The factor is always greater than one and reduces the Stokes drag force by:

$$C_c = 1 + \frac{2.52\lambda}{d} \quad (5.10)$$

Where,  $\lambda$  is the mean free path (48 nm for methane), given by:

$$\lambda = \frac{1}{\sqrt{2}n\pi d_m^2} \quad (5.11)$$

Where,  $d_m$  is the diameter of gas molecule;  $n$  number of molecules per unit volume.

The correlation extends the range of application of the Stokes's law to particles of 0.1  $\mu\text{m}$  in diameter. The more extended formulas to still smaller particles are empirical correlations based on experimental measurements of the *slip*. The following equation, developed by Allen and Raabe for oil droplets (1982) and for solids particles (1985) agrees with Eq. (5.10) (adjusted for mean free path) within 2.1% for all particle sizes:

$$C_c = 1 + \frac{\lambda}{d} \left[ 2.34 + 1.05 \exp\left(-0.39 \frac{d}{\lambda}\right) \right] \quad (5.12)$$

The correlation is plotted for different sizes of particles flow in methane in Figure (5.1). One can observe the high slope in the slip factor for tiny particles and then at about 1  $\mu\text{m}$  in diameter, the slip factor becomes relatively constant for particles larger than 1  $\mu\text{m}$ .

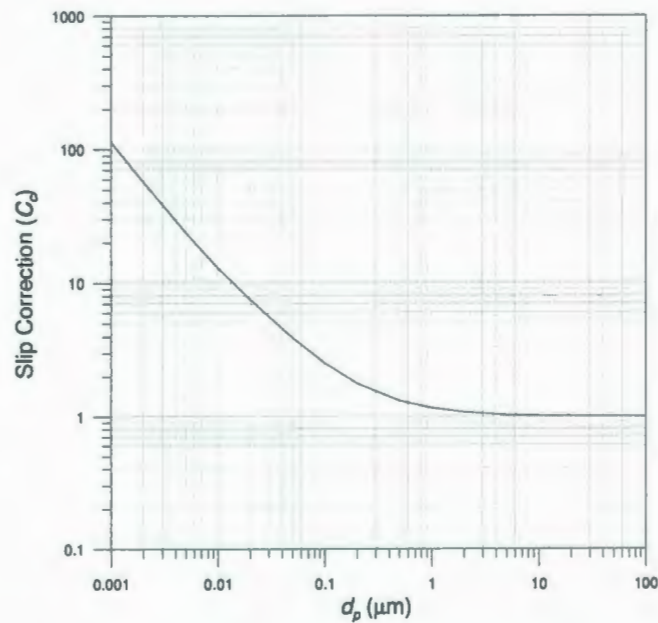


**Figure (5.1)** Stokes slip correction coefficient ( $C_c$ ) for non-continuum flow

## 5.4 Gravitational Settling

### 5.4.1 Low Reynolds numbers ( $Re_p < 1$ )

The terminal velocity of spherical particles due to gravitational settling can be obtained from the following expression:

$$u_s = \frac{\rho_p d_p^2 g C_c}{18\mu_g} \quad (5.13)$$

The above expression is valid for any particle size since the slip correction has been taken into account and can strictly be used for the Stokes flow. The formula is quite accurate over the extended range  $0.1 < Re_p < 1$  (Vincent, 1995; Hinds, 1999).

The buoyancy effects have been neglected in the formula since the particle density is much larger than that of the gas.

#### 5.4.2 Other $Re_p > 1$

For particle motion in the Stokes region, the settling velocity of Eq.(5.13) can be determined explicitly if particle diameter and density are known. Method of calculation  $u_s$  at higher particle Reynolds numbers ( $Re_p > 1$ ) is given by (Hinds, 1999):

$$u_s = \sqrt{\frac{4\rho_p d_p g C_c}{3C_D \rho_f}} \quad (5.14)$$

However, in order to calculate the settling velocity by Eq. (5.14), the drag coefficient must be determined first using Eq. (5.9). So, we need the particle Reynolds number for estimating the drag coefficient which in turn requires knowing the settling velocity. One way around this quandary is an iterative solution obtained by substituting Eq. (5.9) into Eq.(5.14) and trying different values of velocity until Eq. (5.14) is an equality to within some desired accuracy.

Another approach requires converting the implicit form of Eq.(5.14) to an explicit one.

Rearranging Eq.(5.14) for  $C_D$  and multiplying both sides by  $\text{Re}_p^2$  gives:

$$C_D \text{Re}_p^2 = \frac{4 d_p^3 \rho_f \rho_p g}{3 \mu_g^2} \quad (5.15)$$

Since Eq. (5.15) does not include velocity, the left hand side can be determined and used to estimate the settling velocity graphically by plotting the expression of Eq.(5.15) in the Drag-Reynolds number curve of Eq. (5.9a-d). Alternatively, an empirical equation has been developed for calculating settling velocity using  $C_D \text{Re}_p^2$  directly:

$$u_s = \left( \frac{\mu_g}{\rho_g d_p} \right) \exp(-3.070 + 0.9935J - 0.0178J^2) \quad (5.16)$$

Where,

$$J = \ln(C_D \text{Re}_p^2) = \ln\left(\frac{4 d_p^3 \rho_f \rho_p g}{3 \mu_g^2}\right) \quad (5.17)$$

Eq. (5.16) agrees with iterative calculations using the transition region approximation of drag coefficient, within 3% for the range  $1 < \text{Re} < 600$ .

To touch the influence of the correlation on the magnitude of the settling velocity, a plot was developed using settling velocity expressions in both the Stokes's law and high Reynolds number conditions. Figure (5.2) shows the overestimation in the settling velocity predicted by the Stokes's law. For instance, if the Stokes's law was unwittingly

applied to a condition of a particle Reynolds number of 40, the calculated velocity would have a degree of overestimation of about 180%.

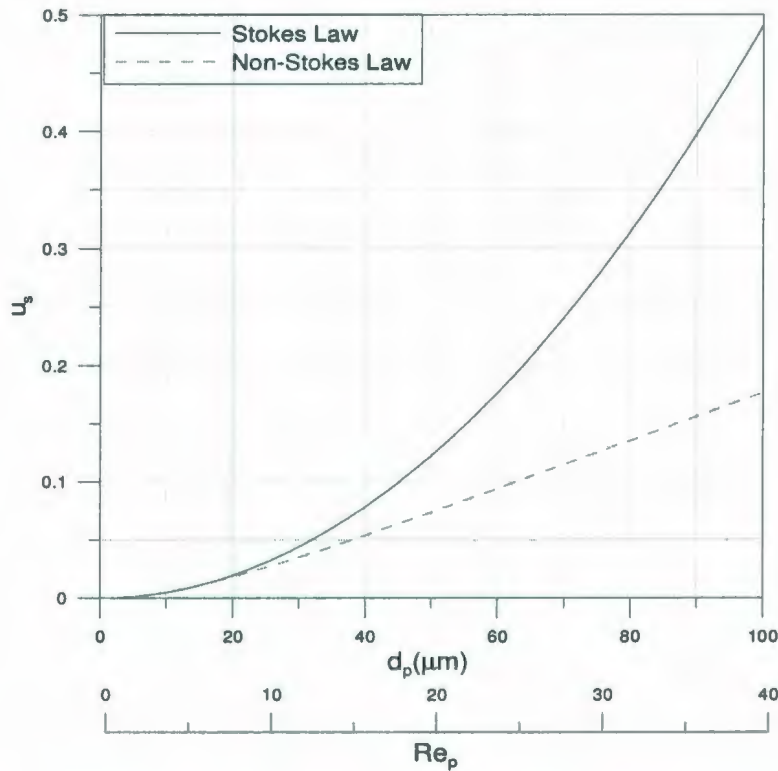


**Figure (5.2)** Deviation in settling velocity as a function of Reynolds number

### 5.5 Lift Force

Small particles lying entirely submerged in the viscous sublayer close to a wall satisfy the condition that the Reynolds number based on the friction velocity  $u^*$  is smaller than unity (Hinze 1975) and experience a lift force perpendicular to the direction of flow. The shear lift originates from the inertia effects in the viscous flow around the particle and is basically different from aerodynamic lift force. The first expression for the inertia shear lift was obtained by Saffman (1968):

$$F_{L(Saff)} = 1.615 \rho v^{0.5} d_p^2 (u_f - u_p) \left| \frac{du_f}{dy} \right|^{0.5} \operatorname{sgn}\left(\frac{du_f}{dy}\right) \quad (5.18)$$

Equation (5.18) is valid under the following constraints:

$$\operatorname{Re}_p = \frac{V_r d_p}{\nu} \ll 1; \operatorname{Re}_G = \frac{\dot{\gamma} d_p^2}{\nu} \ll 1; \varepsilon = \frac{\operatorname{Re}_G^{1/2}}{\operatorname{Re}_p} \gg 1; \dot{\gamma} = \frac{du_f}{dy}$$

For large and small  $\varepsilon$ , McLaughlin (1993) obtained the following empirical formulas:

$$\frac{F_L}{F_{L(Saff)}} = \begin{cases} 1 - 0.287 \varepsilon^{-2} & \varepsilon \gg 1 \\ -140 \varepsilon^5 \ln(\varepsilon^{-2}) & \varepsilon \ll 1 \end{cases} \quad (5.19)$$

Cherukat and McLaughlin (1994) analyzed the lift force acting on spherical particles near a wall as shown in Figure (5.3) and came up with the following correlation:

$$F_{L(C-L)} = \frac{\rho V_r^2 d_p^2 I_L}{4} \quad (5.20)$$

Where,

$$V_r = u_p - u_f = u_p - \dot{\gamma} \quad (5.21)$$

and for non-rotating particles,

$$\begin{aligned} I_L = & (1.7716 + 0.216K - 0.7292K^2 + 0.4854K^3) \\ & - \left( \frac{3.2397}{K} + 1.145 + 2.084K - 0.9059K^2 \right) \Lambda_G \\ & + (2.0069 + 1.0575K - 2.4007K^2 + 1.3174K^3) \Lambda_G^2 \end{aligned} \quad (5.22)$$

Where,

$$K = \frac{d_p}{2l}, \quad \Lambda_G = \frac{\gamma d_p}{2V_r}$$

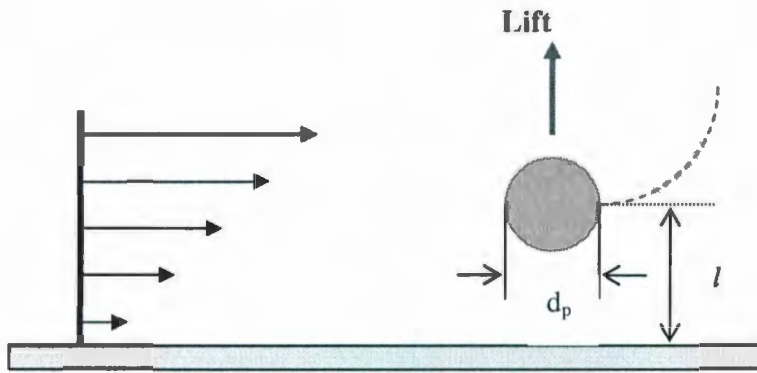


**Figure (5.3)** Lift force on particle near the wall

When  $l$  approaches  $d_p/2$ , the particle touches the wall as shown in Figure (5.4). Leighton and Acrivos (1985) obtained the following expression for the lift force on spherical particles:

$$F_{L(L-A)} = 0.576 \rho_f d_p^4 \dot{\gamma}_w^2 \quad (5.23)$$

which is always directed away from the wall.

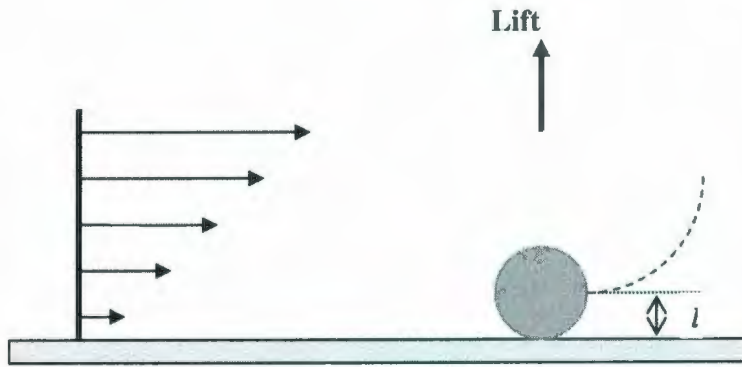


**Figure (5.4)** Lift force on particles touching the wall

For small particles in turbulent flows, using:

$$u^+ = y^+, \quad u^+ = \frac{u}{u^*}, \quad y^+ = \frac{yu^*}{\nu}, \quad \dot{\gamma} = \frac{u^{*2}}{\nu}$$

Where,  $u^*$  is the shear velocity, Eq. (5.23) becomes:

$$F_{L(L-A)}^+ = 0.567d^+ \quad (5.24)$$

Where:

$$F_L^+ = \frac{F_L}{\rho_f \nu^2}, \quad d^+ = \frac{d_p u^*}{\nu} \quad (5.25)$$

Experimental investigations on the lift force were performed for relatively larger particles in the range of 100 to several hundred micrometers. Hall's (1988) experimental work suggested the following formula:

$$F_{L(Hall)}^+ = 4.21(d^+)^{2.31} \quad \text{for } d^+ > 1.5 \quad (5.26)$$

Mollinger and Nieuwstadt (1996) found:

$$F_{L(MN)}^+ = 15.57(d^+)^{1.87} \quad \text{for } 0.15 < d^+ < 1 \quad (5.27)$$

The comparison of the model's predictions with the experimental data demonstrates that the experimental data are relatively much higher than the theoretical models. The model proposed in this thesis adopts the formula of Cherukat and McLaughlin (1994). The variation in the lift force slightly changes when the particle-wall distance is small. For particles further away from the wall, the incremental changes become more significant and the lift force increases rapidly as shown in Figure (5.5).

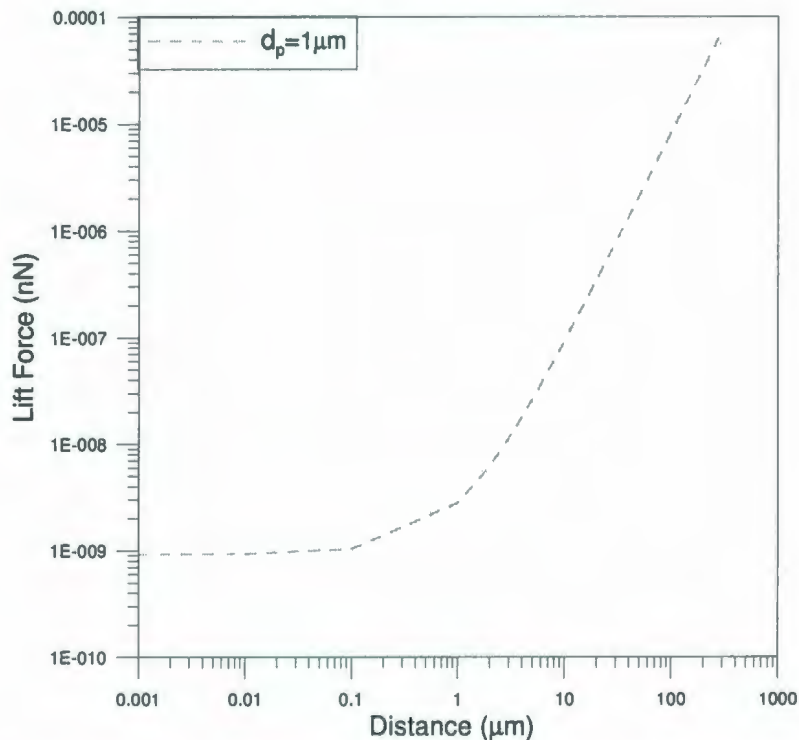


**Figure (5.5)** Lift force as a function of particle-wall distance

## 5.6 Adhesive Force

Adhesive forces are induced as a result of inter-particle forces which in turn are created due to particle wetness, electrostatic charges, and the van der Waals forces (A weak

physical force that holds together two molecules or two different parts of the same molecule). These forces are known to cause adhesion of a particle to a wall or onto another particle. The van der Waals force becomes apparent when very smooth surfaces are brought into contact. The first attempt to estimate the magnitude of the van der Waals forces acting on solid bodies was performed by London (Anandarajah *et al*, 1995). He computed the van der Waals attractive energy between two unit molecules in vacuum separated by a distance  $r$  according to the following formula:

$$U(r) = -\frac{B}{r^6} \quad (5.28)$$

Where,  $B$  is the London constant. This equation was then corrected by Anandarajah and Chen (1995) through introducing a parameter named the “characteristic wavelength  $\lambda_w$ ” of the interaction, often assumed to be about 100 nm (Chen *et al*, 1996). The formula now takes the following form:

$$U(r) = -\frac{Bc}{r^6(r+c)} ; c = -\frac{b\lambda_w}{2\pi} ; b = 3.1 \quad (5.29)$$

Hamaker proposed a method for calculating the interaction force for various geometries. For instance, the force  $F$  between two infinite flat plates with separation distance of  $z$  is expressed by (Crowe *et al*, 1998):

$$F = \frac{A}{6\pi z^3} \quad (5.30)$$

Where,  $F$  is force per unit area and  $A$  is referred to as the *Hamaker constant*. Hamaker approach is based on two assumptions:

- The retardation effect of the dispersion interaction is neglected, whatever the distances are.
- The interaction potential between two molecules keeps the same form even if other molecules surround them.

These two assumptions made the method suffering drawbacks and encouraging the other theory, the macroscopic theory, to develop. The theory was initiated by Lifshitz and then expanded in 1961 by Dzyaloshinskii *et al* (Bonnefoy *et al*, 2005), known as (DLP theory). The Lifshitz theory is complete and exact in that it takes into account the multi-body interactions and the retardation effect. However, its complexity prevents any application to complex geometries. Thus, although some advantages are acquired using the DLP theory, other problems, such as limited applications for simple geometries (sphere for example), have arisen (Bonnefoy *et al*, 2005).

To circumvent these problems, Bonnefoy *et al.* (2005) adopted the *hybridation* method of Parsegian in their study on the interaction between gas hydrate particles. They introduced the interaction potential as an approximating product of two functions. The first function is calculated with the Hamaker approach while the second function expresses the retardation effect.

This hybrid approach is adopted in our model for the van der Waals forces calculation in both particle-wall and particle-particle interactions. The model, detailed below, is simple enough to permit closed-form solutions to be obtained by the Hamaker-De Bore approach for macrobodies of different geometries (Chen *et al.*, 1996).

## 5.7 Model of Adhesion

Often times, conditions for pipe flows and boundary layer flows can produce high concentrations of particles very near the wall. Several studies have shown such high concentrations at transverse positions on the order of the particle diameter for solid particles (Young and Hanratty, 1991; Kaftori *et al.* 1995; Young & Leeming, 1997) as well as for gas bubbles (Zun *et al.* 1993; Marie *et al.* 1997; Felton & Loth, 2001). In these cases, the consideration of particle wall interactions becomes crucial.

### 5.7.1 Particle-Wall Attraction

Consider the interaction between a spherical particle (1) and a wall (2) separated by a medium (3) shown in Figure (5.6). The van der Waals energy between the particle and the wall can be obtained from the following expression:

$$U(h) = A[U_0(h) + U_1(h)] \quad (5.31)$$

Where,  $A$  is the Hamaker constant in (Joules).

$$U_0(h) = -\frac{1}{6} \left[ \left( \frac{2}{h/r - r/h} \right) - \ln \left( \frac{h/r + 1}{h/r - 1} \right) \right] \quad (5.32)$$

$$\begin{aligned}
U_1(h) = & -\frac{h+c-3r}{6c^4}(h+r+c)^3 \ln(h+r+c) + \frac{h+c+3r}{6c^4}(h-r+c)^3 \ln(h-r+c) \\
& + \left[ \frac{h-3r}{6c^4}(h+r)^3 + \frac{2(h-2r)}{3c^3}(h+r)^2 + \frac{h-r}{c^2}(h+r) + \frac{2h}{3c} \right] \ln(h+r) \\
& - \left[ \frac{h+3r}{6c^4}(h-r)^3 + \frac{2(h+2r)}{3c^3}(h-r)^2 + \frac{h+r}{c^2}(h-r) + \frac{2h}{3c} \right] \ln(h-r) \\
& - \left[ \frac{h^2 r}{3c^3} + \frac{r^3}{c^3} + \frac{hr}{c^2} + \frac{r}{c} \right]
\end{aligned} \tag{5.33}$$

where  $c = -\frac{b\lambda}{2\pi}$ ;  $b = 3.1$  and  $\lambda_w = 100 \text{ nm}$ .

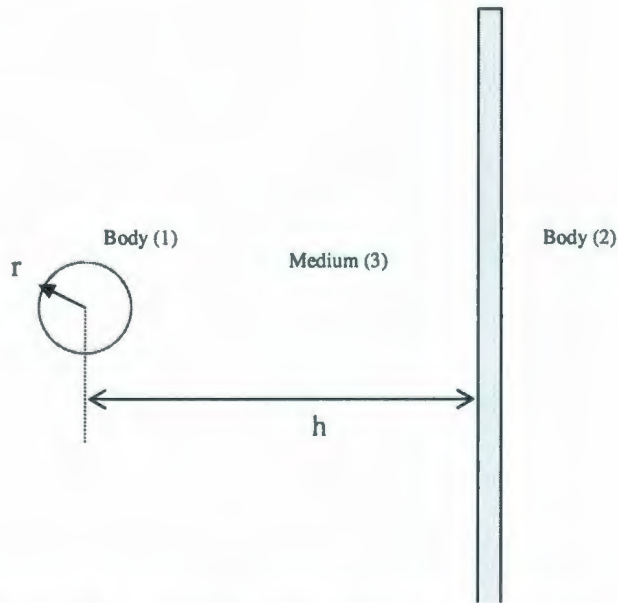


**Figure (5.6)** Adhesive force in particle-wall system

The van der Waals attractive force is obtained through differentiating Eq. (5.31) with respect to  $h$  as:

$$F(h) = A[F_0(h) + F_1(h)] \tag{5.34}$$

Where,

$$F_0(h) = \frac{2}{3r[(h/r)^2 - 1]} \quad (5.35a)$$

$$\begin{aligned}
F_1(h) = & -\frac{2(h+c-2r)}{3c^4}(h+r+c)^2 \ln(h+r+c) + \frac{2(h+c+2r)}{3c^4}(h-r+c)^2 \ln(h-r+c) \\
& - \left[ \frac{2(h+2r)}{3c^4}(h-r)^2 + \frac{2(h+r)}{c^3}(h-r) + \frac{2h}{c^2} + \frac{2}{3c} \right] \ln(h-r) \\
& + \left[ \frac{2(h-2r)}{3c^4}(h+r)^2 + \frac{2(h-r)}{c^3}(h+r) + \frac{2h}{c^2} + \frac{2}{3c} \right] \ln(h+r) \\
& - \frac{4hr}{3c^3} - \frac{8r}{3c^2} - \frac{4hr}{3c(h^2-r^2)}
\end{aligned} \quad (5.35b)$$

$U_I(h)$  and  $F_I(h)$  stand for the retardation effects according to the proposed correction function and their values approach zero when  $c$  goes to infinity. Thus original London equation will be obtained.

The Hamaker constant between two solid particles separated by a third material is expressed by:

$$A_{123} = (\sqrt{A_{11}} - \sqrt{A_{33}})(\sqrt{A_{22}} - \sqrt{A_{33}}) \quad (5.36)$$

Where,  $A_{11}$  and  $A_{22}$  are the Hamaker constants for the solids and  $A_{33}$  is the Hamaker constant of the third material.

### 5.7.2 Particle-Particle Attraction

Figure (5.7) shows a system of two spherical particles of radii  $r_1$ ,  $r_2$  placed at a centre-to-centre separation distance of  $h$ .

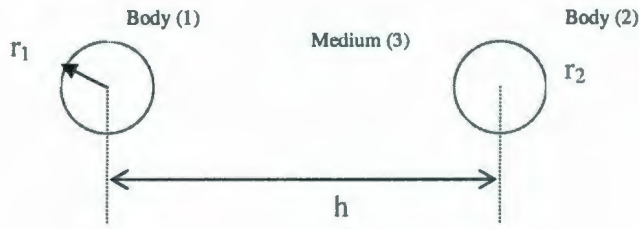


**Figure (5.7)** Particle-Particle Adhesion force

Defining the following parameters:

$$d_1 = h - r_1 - r_2 \quad (5.37a)$$

$$d_2 = h + r_1 - r_2 \quad (5.37b)$$

$$d_3 = h + r_1 + r_2 \quad (5.37c)$$

$$d_4 = h - r_1 + r_2 \quad (5.37d)$$

and

$$e_i = d_i + c \quad (5.37e)$$

$$b_i = (-1)^{i+1} e_i^4 [4e_i - 5(h+c)] - 20r_1 r_2 e_i^3 \quad (5.37f)$$

$$g_i = (-1)^{i+1} e_i^3 [4e_i^2 - 5(4h+c)e_i + 20h(h+c)] + 20r_1 r_2 e_i^2 (3h - e_i) \quad (5.37g)$$

for  $i = 1, 2, 3$ , and  $4$ , the interaction energy  $U(h)$  is given by Eq. (5.31) listed earlier with the following definitions of its terms:

$$U_0(h) = -\frac{1}{6} \left[ \frac{2r_1 r_2}{d_1 d_3} + \frac{2r_1 r_2}{d_2 d_4} + \ln \frac{d_1 d_3}{d_2 d_4} \right] \quad (5.38a)$$

$$U_1(h) = -\frac{1}{30c^4h} [4cr_1r_2(4r_1^2 + 4r_2^2 + 2h^2 + 7hc + 9c^2) + c^4(c + 5h) \ln \frac{d_2d_4}{d_1d_3} + \sum_{i=1}^4 b_i \ln \frac{e_i}{d_i}] \quad (5.38b)$$

The van der Waals attractive force  $F(h)$  is given by Eq. (5.34):

$$F(h) = A[F_0(h) + F_1(h)] \quad (5.34)$$

where:

$$F_0(h) = \frac{h}{3} \left[ -\frac{1}{d_1d_3} + \frac{1}{d_2d_4} + \frac{2r_1r_2}{d_1^2d_3^2} + \frac{2r_1r_2}{d_2^2d_4^2} \right] \quad (5.39)$$

$$F_1(h) = \frac{1}{30c^4h} [4cr_1r_2(4r_1^2 + 4r_2^2 - 2h^2 + 9c^2) + ch \sum_{i=1}^4 \frac{b_i}{e_id_i} + 2c^4h^2(c + 5h) \left( \frac{1}{d_1d_3} - \frac{1}{d_2d_4} \right) + c^5 \ln \frac{d_2d_4}{d_1d_3} + \sum_{i=1}^4 g_i \ln \frac{e_i}{d_i}] \quad (5.40)$$

It is worth to mention here that  $U_0(h)$  and  $F_0(h)$  represent the non-retarded contributions and  $U_1(h)$  and  $F_1(h)$  represent the retarded contributions in accordance with the proposed correction model.

## 5.8 Conclusion

As the external forces acting on the particles control the trajectory of the particles, it is important to understand the significance of each force on the particle movement. This chapter highlights the forces applied to the particle and the correlations that determine the particle movement. The important conclusions in this chapter can be summarized as follows:

- Drag and gravitational forces are the only significant forces influencing the particle in the fully turbulent regime.
- Slip factor should be taken into account when the particle size is smaller than 1  $\mu\text{m}$ .
- Different expressions should be used in predicting the settling velocity for the Stokes's and non-Stokes's regimes.
- Particles that merge in the sublayer region experience other forces such as lift and adhesive forces.

The model proposed in this thesis adopts the Bonnefoy hybrid approach for adhesive force calculation since it has been used for hydrate applications (Bonnefoy *et al*, 2005), and the Cherukat and McLaughlin model for lift force. The model also considers the non-continuum correction for very small particle sizes and the correlation of non-Stoke's regime.

## CHAPTER 6

### Deposition Mechanism

In this Chapter, the motion and the mechanism of the deposition of hydrate particles suspended in a fluid stream is discussed. The effects associated with the particle's own inertia become manifest for relatively large particles particularly in accelerating fluid motion. However, very tiny particles experience unsystematic motion as a result of their continuous bombardment by the molecules of the surrounding gas (Crowe, 2006). The mechanisms driving particle motion are synonymously called deposition mechanisms since the result is to make particles migrate to the bounded surfaces and deposit there.

#### 6.1 Brownian Motion

The very tiny hydrate particles exhibit a random motion called the Brownian motion as a result of their continuous bombardment by the molecules of the surrounding gas. This motion causes net transfer of particles from regions of high to low concentration, a process known as diffusion which is described by the Fick's law in terms of the number of particles diffused according to the following expression:

$$J_p = -\Gamma_p \nabla n_p \quad (6.1)$$

Where,  $J_p$  is the flux vector (particles/m<sup>2</sup>/sec),  $n_p$  the particle concentration (particle/m<sup>3</sup>), and  $\Gamma_p$  is the particle diffusion coefficient (m<sup>2</sup>/sec).

The diffusion coefficient depends strongly on the particle size, with smaller particles diffusing much more efficiently than larger ones. Figure (6.1) shows the variation of the

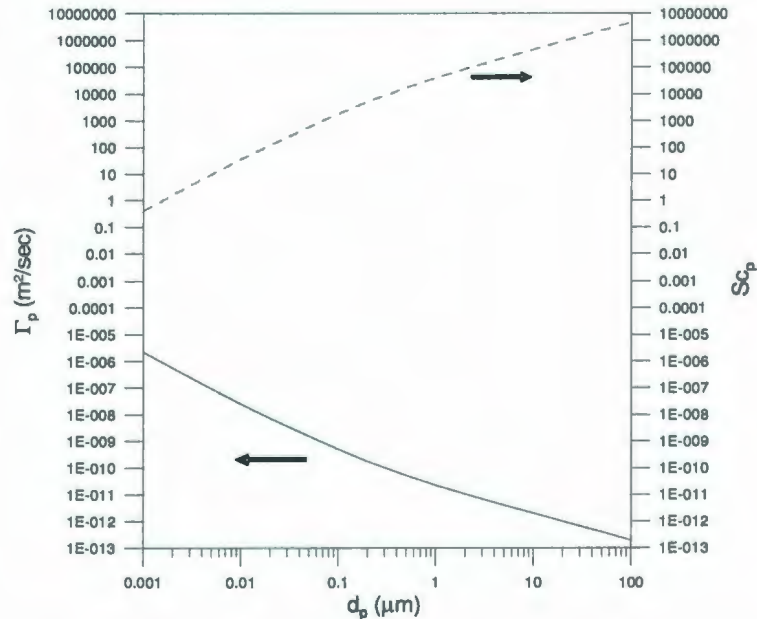
diffusion coefficient of hydrate particles in methane for different particle sizes. For example under the same concentration gradients the diffusive mass flux of a 0.01- $\mu\text{m}$  particle is about 15 000 times larger than that of a 10- $\mu\text{m}$  particle.

Figure (6.1) also shows the variation of the particle Schmidt number ( $Sc_p$ ) defined as:

$$Sc_p = \frac{V_g}{\Gamma_p} \quad (6.2)$$

Where, the diffusion coefficient of particles is determined from the Stokes-Einstein equation and slip correction:

$$\Gamma_p = \frac{k_B T_g C_c}{3\pi\mu_g d_p} \quad (6.3)$$



**Figure (6.1)** Diffusivity and Schmidt Number as a function of particle size

The strength of the Brownian diffusion can be characterized using the quantity called, the root mean square (*rms*) net displacement of a diffusing particle over a time interval  $\Delta t$ :

$$x_{rms}^2 = \langle [x(t + \Delta t) - x(t)]^2 \rangle \quad (6.4)$$

This displacement is related to the particle diffusion coefficient through the expression

$$x_{rms} = \sqrt{2\Gamma_p \Delta t}$$

Since the growth of the particle causes alleviation in the Brownian movement, the ratio  $x_{rms} / u_s \Delta t$  is an indicator of the Brownian strength of diffusion.

As illustrated in Figure (6.2), the ratio is of the order of 1 for  $d_p = 0.6 \mu\text{m}$ , whereas it is of  $10^4$  for  $d_p = 0.01 \mu\text{m}$  and of  $10^{-3}$  for  $d_p = 10 \mu\text{m}$ . It can be concluded that the Brownian diffusion is an important transport mechanism only for small particles of the submicrometer range. In contrast, the gravitational settling and inertia effects outweigh diffusional transport for particles greater than  $1 \mu\text{m}$  in diameter.

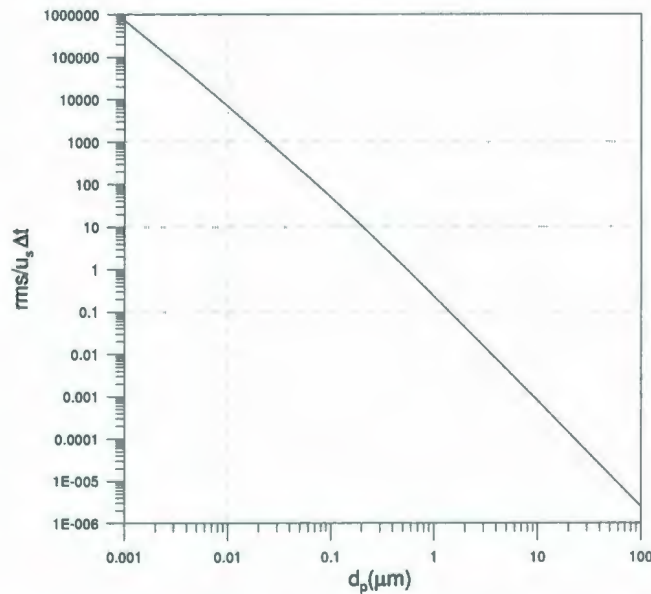


**Figure (6.2)** Brownian to settling ratio for various hydrate particle sizes

## 6.2 Impaction Effects

In an accelerating flow field, particles are not able to follow perfectly the fluid motion due to their own mass. For instance, in straight-line accelerating (decelerating) motion, hydrate particles lag behind (ahead) the Lagrangian “fluid particles”. For sub-micrometer particles, and in the absence of external force fields, the Brownian or turbulent diffusion is the basic mechanisms that drive deposition. For particles larger than about 1  $\mu\text{m}$ , deposition is primarily due to inertial impaction and gravitational settling.

A basic quantity characterizing convective transport of a hydrate particle is the *penetration ratio*, or *penetration fraction*, defined as the fraction of the inflowing particles that exit the flow system (Crowe, 2006). It can be written as:

$$f_p = \frac{C_{out}}{C_0} \quad (6.5)$$

Where,  $C_{out}$  and  $C_0$  are the particle concentrations (either mass or number) at the outlet and inlet, respectively. Alternatively, *collection efficiency* can be defined as the fraction of the inflowing particles that is lost by deposition (Crowe, 2006):

$$\eta_g = 1 - f_p \quad (6.6)$$

Another quantity commonly employed to characterize deposition in convective particle flows is *deposition velocity*, defined as:

$$V_d = \frac{G_p}{C_{av}} \quad (6.7)$$

Where,  $G_p$  is the particle mass flux to the wall and  $C_{av}$  the particle average particle concentration above the surface. The latter is usually taken equal to the average concentration over the cross-section of the conduit.

For fully developed turbulent flow in a circular pipe of length  $L$ , the deposition velocity  $V_d$  may be considered as constant along the tube, and the penetration fraction can be express as:

$$f_p = \exp\left(-\frac{4V_d L}{U_g D}\right) \quad (6.8)$$

Where,  $U_g$  is the carrier gas velocity;  $D$  is the pipe diameter.

### 6.3 Correlations of Deposition Velocity

Equation (6.8) enables the calculation of penetration through the knowledge of the deposition velocity. Models of the deposition velocity have been numerous reported in the literatures based on experiment, numerical simulation and analytical theory.

During past few decades, intensive investigations have been conducted to describe the deposition phenomena of the particles in turbulent flow. Schwendiman and Postma (1961), Wells and Chamberlain (1969), Liu and Agarwal (1974), Friedlander and Johnston (1957), Sehmel (1968), and Ilori (1971) reported extensive experimental data for particle deposition rate in turbulent duct flows. Wood (1981), and Papavergos and Hedley (1984) have provided a reviews of the experimental results. In general, the studies concluded that deposition velocity has a V-shaped variation with a minimum at the particle relaxation time of about 0.1 to 0.5 wall units (Chen et al., 1997). The rate of

particle deposition increases as the relaxation time decreases in the diffusion regime whereas it increases when the relaxation time increases in the impaction regime.

Theories of particle deposition process were also addressed by many researchers; Fuchs (1964), Wood (1981), Hidy (1984), Papavergos and Hedley (1984), and Hinds (1999). Semi-empirical correlations for evaluating particle deposition rates in turbulent ducts have been proposed by Friedlander and Johnston (1957), Davies (1966), and Cleaver and Yates (1975); however, the expressions are valid for smooth walls. Further progress in developing the deposition model was reported by Fichman et al. (1988), Fan and Ahmadi (1993, 1994), Chen and Ahmadi (1997), Shams et al. (2000), and Tian and Ahmadi (2007).

Numerical studies of transport and deposition of particles in turbulence flow field have been conducted as well in the past few decades. Among lots of literatures studied such phenomena, Li and Ahmadi (1991, 1993) performed a series of numerical simulations on deposition of small particles in a turbulent channel flow. Li et al. (1994) presented digital simulation results for particle deposition rate in an obstructed turbulent duct flow. Finally, Tian and Ahmadi (2007) compared different computational models for predicting particle deposition in the turbulent duct flows.

In summary, earlier and recent works are confirmed that the deposition velocity has a V-shaped variation. The following section discusses and compares several models that have addressed the deposition velocity of the particles in turbulent flows.

### 6.3.1 Model of Wells and Friendlander

The following three parameters need to be introduced before discussing the correlation of the deposition velocity:

- A time scale characterizing the adjustment of particle velocity to a change in fluid velocity is called the *particle relaxation time (velocity response time)*. It is calculated by considering the time required by the particle to reach its terminal settling velocity when released with zero initial velocity in a quiescent fluid and for spherical particle is given by:

$$\tau_v = \frac{u_s}{g} = \frac{\rho_p d_p^2 C_c}{18\mu_s} \quad (6.9)$$

- The *stop distance* is a length scale that characterizes the persistence of a particle to continue its original motion in a changing flow field before it equilibrates again with the fluid motion. Its value is simply the initial velocity times the relaxation time:

$$S_L = V_0 \tau_v \quad (6.10)$$

The formula represents the distance a particle will travel in stagnant fluid before it comes to rest, following injection with initial velocity  $V_0$  and in the absence of external forces.

- **Stokes number:** here defined as the ratio of the *stop distance* to a characteristic length of the flow.

$$St = \frac{S_L}{L} = \frac{V_0 \tau_v}{L} = \frac{\rho_p d_p^2 C_c V_0}{18\mu_s L} \quad (6.11)$$

Now for a particle with:  $\tau_v^+ = \frac{\tau_v (u^*)^2}{\nu_g} < 0.3$ , the correlation of deposition velocity

proposed by Wells and Chamberlain (1967) can be used:

$$\frac{V_d}{U_g} = 0.039 S_c^{-2/3} \text{Re}^{-1/4} \quad (6.12)$$

Where,  $\nu_g$  is the kinematics viscosity of the fluid. Schmidt number is calculated using Eq. (6.2) and the fluid Reynolds number is:

$$\text{Re} = \frac{U_g D_{\text{pipe}}}{\nu_g} \quad (6.12a)$$

In most cases, the above correlation is satisfied for particles with diameter  $d_p < 1 \mu\text{m}$  (Crowe, 2006).

For other regimes where  $\tau_v^+ > 0.3$ , or roughly  $d_p > 1 \mu\text{m}$ , the Friedlander and Johnstone (1957) correlation (Eq. 6.13) is frequently used. The deposition velocity is calculated as follows:

$$\frac{V_d}{U_g} = \begin{cases} \frac{f/2}{1 + \sqrt{f/2} (1525/(S_L^+)^2 - 50.6)} & S_L^+ < 5 \\ \frac{f/2}{1 + \sqrt{f/2} \{5 \ln [5.04/(S_L^+/5 - 0.959)] - 13.73\}} & 5 \leq S_L^+ \leq 30 \\ \frac{f}{2} & 30 < S_L^+ \end{cases} \quad (6.13)$$

Where,  $f$  is the Moody friction factor; and

$$S_L^+ = \frac{\rho_g d_p^2 \rho_p U_g^2 f/2}{18 \mu_g^2} \quad (6.14)$$

As a summary, Eq. 6.12 is used to estimate the deposition velocity for particles size in the range of the Brownian diffusion, whereas Eq.6.13 is the governing deposition velocity formula for particles with sizes that lie in the inertia region.

### 6.3.2 Wood Model

The Wood non-dimensional deposition velocity is given by:

$$V_{dr}^+ = 0.057Sc^{-2/3} + 4.5 \times 10^{-4} \tau^{+2} + \tau^+ g^+ \quad (6.15)$$

Where,  $Sc$  is the Schmidt number and:

$$\tau^+ = \frac{u^{*2}}{v} = \frac{\rho_p d_p^2 u^{*2} Cc}{18 \rho_f \nu^2} \quad (6.16a)$$

$$g^+ = \frac{v}{u^*} g \quad (6.16b)$$

The reference velocity, the mean stream velocity ( $Ug$ ), used in the Wells and Friedlander model has been changed to the friction velocity. Hence, the dimensionless deposition velocity would be:

$$V_{dr}^+ = \frac{V_{dr}}{u^*} \quad (6.17)$$

The first term in Eq. (15) is resulted from the Brownian motion and eddy diffusion, and the second term is the consequences of particle deposition by the eddy diffusion-impaction mechanism, while the last term stands for the gravitational sedimentation on the lower wall of horizontal pipes.

### 6.3.3 The model of Fan and Ahmadi

Fan and Ahmadi (1993) proposed an empirical correlation for deposition of particles including the effects of surface roughness and gravity. For horizontal ducts, the expression takes the form of:

$$V_{dr}^+ = \begin{cases} 0.084Sc^{-2/3} + \frac{1}{2} \left[ \frac{(0.64k^+ + 0.5d_p^+)^2}{3.42} \right]^{1/(1+\tau^+L_1^+)} \\ \times \left[ 1 + 8e^{-(\tau-10)^2/32} \right] \frac{0.037}{1-\tau^+L_1^+} + \tau^+g^+ & \text{if } V_{dr} < 0.14 \\ 0.14 & \end{cases} \quad (6.18)$$

where  $L_1^+ = \frac{3.08}{Sd_p^+}$ ;  $S = \frac{\rho_p}{\rho_f}$ ;  $d_p^+ = \frac{d_p u^*}{\nu}$  and  $k^+$  is the surface roughness ( which is zero for smooth surface).

### 6.3.4 Comparison of Models

To appreciate the process of particle deposition predicted by the model adopted in this project, comparison of the theoretical prediction of the model against some experimental data and semi-empirical correlations has been performed. Although experimental data for particle deposition from turbulent flows is relatively scarce, there is however more data for deposition from aerosols applications. The deposition efficiency is compared using the experimental data, the numerical data, and the semi-empirical models suggested by Wells and Freindlander, Wood, and Fan and Ahmadi (1993).

Figure (6.3) compares the suggested model with those of earlier studies for horizontal pipe. The experimental data of Kavasnak et al. (1993), the numerical simulation results of Tian et al. (2007) and Shams et al. (2000), and the empirical equations of Wood (1981),

Fan and Ahmadi (1993), and Wells (1967) and Friedlander et al. (1957) are plotted in this figure. The experimental data and the simulation results show that the deposition velocities have a “V-shaped” variation. The empirical equation of Wood (1981) and Fan and Ahmadi (1993) models are slightly varied for tiny particles, thus no “V-Shape” has obtained. In turn, the model of Wells and Friedlander gives better trend than Fan and Ahmadi curve and describes the deposition velocity that resulted by the experimental and numerical works in very good manner.

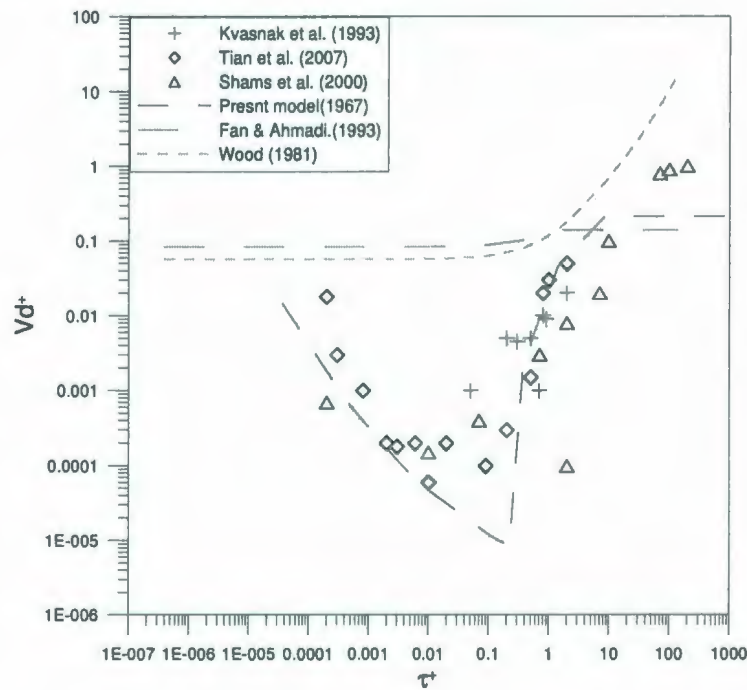


**Figure (6.3)** Comparison of non dimensional deposition velocity as predicted by earlier experiments and models in horizontal pipe

The process of deposition can be divided into two regions, the Brownian dominated region and the inertia dominated region. In the Brownian region, the deposition rate increases with decrease in particle size, see Fig. (6.4). For large particles, turbulence eddy impaction becomes significant and dominates the deposition process (Chen and Ahmadi,

1997). Hence, the deposition efficiency increases with particle size. For very large particles, the particle inertia becomes very large and essentially not influenced by other forces since the particle deposition rate approaches constant. The tendency of such particles occurs at relaxation time  $\tau^+ > 10$  as shown in Fig. (6.4).

In summary, the deposition velocity and deposition efficiency in turbulent pipe flow follow a V-shaped curve. The deposition efficiency increases both with the increase of diameter for large particles, and with the decrease of diameter for submicron particles.

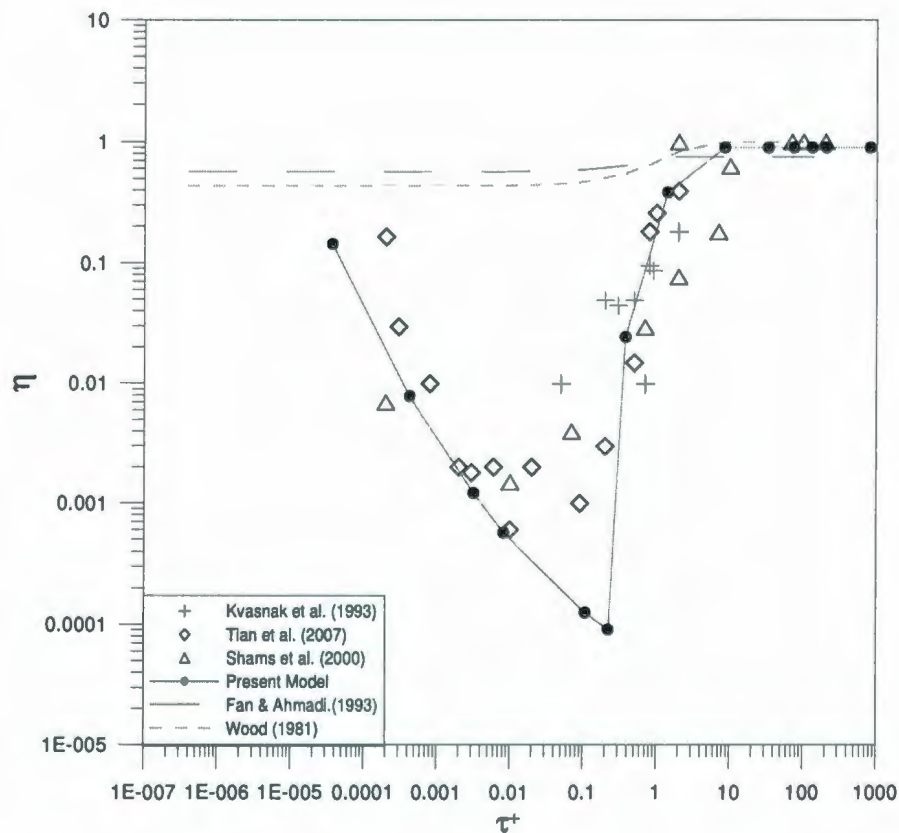


**Figure (6.4)** Comparison of deposition factor as predicted by current model (proposed in this thesis) and earlier results in horizontal pipe

#### 6.4 Number of Deposited Particles

The turbulent mass transport equation included in the model of Cousins and Hewitt (1968) states that the particle deposition flux  $G$  is proportional to the particle concentration  $C$  and to the area of deposition  $A_d$ . The flux  $G$  is the rate at which non-interacting particles deposit ( $dN/dt$ ) while particle concentration  $C$  is defined as the ratio between the number of particles  $N$  and the volume occupied by these particles  $\phi$ . We can therefore write:

$$G = -k_d C, \quad (6.19)$$

Where,  $k_d$  is the constant of proportionality called the deposition coefficient. By comparing Eq. (6.19) to Eq. (6.7), the deposition coefficient is actually the deposition velocity  $V_d$ . Therefore, Eq. 6.19 becomes:

$$\frac{dN}{dt} = -V_d \frac{NA_d}{\phi} \quad (6.20)$$

For pipe geometry, the ratio  $\frac{A_d}{\phi}$  is equivalent to  $\frac{2}{r_{dep}}$  where  $r_{dep}$  stands for the distance from the pipe centerline to the sublayer boundary ( $R-\delta$ ). Now Eq. 6.20 takes the following form:

$$\frac{dN}{dt} = -\frac{2V_d N}{R-\delta} \quad (6.21)$$

Given the initial number of particles released or formed in the pipe ( $N_0$ ) and the number of particles already deposited at a given time  $N_{dep}^0$ , the number of deposited particles,  $N_{dep}$ , can be estimated as a function of time using the solution of Eq. (6.21):

$$\frac{N_0 - N_{dep}}{N_0 - N_{dep}^0} = \exp\left(-\frac{2V_d}{R - \delta}(t - t_0)\right) \quad (6.22)$$

Or

$$\frac{N_{dep} - N_{dep}^0}{N_0 - N_{dep}^0} = 1 - \exp\left(-\frac{2V_d}{R - \delta}(t - t_0)\right) \quad (6.23)$$

Using  $\delta^* = v_g/u^*$  as the reference length and  $t^* = v_g/u^{*2}$  as the reference time, Eq. 6.23 can be written in the following non-dimensional form (identified by the superscript “+”):

$$\frac{N_{dep} - N_{dep}^0}{N_0 - N_{dep}^0} = 1 - \exp\left(-\frac{2V_d}{u^*} \frac{t^* - t_0^*}{R^* - \delta^*}\right) \quad (6.24)$$

Figure (6.5) illustrates the variation of the number of the particle reduction in time as a result of deposition for various particle relaxation times. After 800  $t^*$ , more than 4% of particles with  $\tau_p^+ = 92$  have deposited. During the same time interval, only 0.17% of particles with  $\tau_p^+ = 5.8 \times 10^{-5}$  were labeled as deposited.

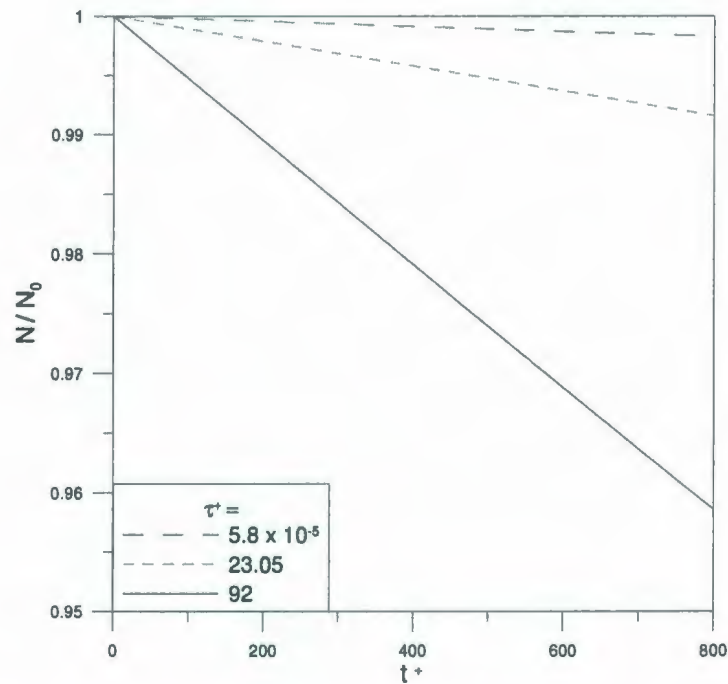


**Figure (6.5)** Decrease of particle number in time due to deposition

### 6.5 Sublayer Region

The behaviour of the particle in the boundary layer region is influenced by the fluid turbulence and properties, particle-wall interactions, particle inertia, gravity in the case of horizontal flows, and local wall surface geometry in the case of cross-flows (Wang *et al*, 2003).

The proposed approach used in the modeling of the particle behaviour within the near-wall region in the current research is discussed in this section. The particle path could be explained from the particle's resultant force based on force balance approach. As mentioned in the previous chapter, lift force is the main force affecting the particle entrainment in the sublayer region. Adhesion force of the particle with the wall resists the

lifting force and jointly influences the movement of the particle. Further drag and settling forces are considered in the model and it is shown how the balance of these forces would determine the trajectory of the particle.

Figure (6.6) shows the force balance applied to a particle moving in the sublayer region.

The following expressions are used for calculating the components of the balance force:

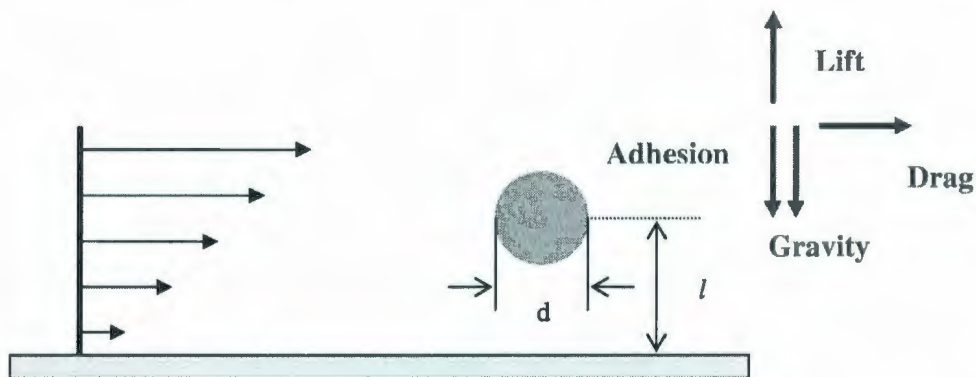


Figure (6.6) Forces acting on a particle within sublayer region

**Drag Force:**

$$F_D = \frac{6\pi\mu_g r_p u_p}{C_c} \quad (6.25)$$

**Gravity force:**

$$F_G = m_p g \quad (6.26)$$

**Adhesion force:**

The van der Waals attractive force:

$$F(h) = A[F_0(h) + F_1(h)] \quad (6.27a)$$

Where,

$$F_0(h) = \frac{2}{3r[(h/r)^2 - 1]} \quad (6.27b)$$

$$\begin{aligned} F_1(h) = & -\frac{2(h+c-2r)}{3c^4}(h+r+c)^2 \ln(h+r+c) + \frac{2(h+c+2r)}{3c^4}(h-r+c)^2 \ln(h-r+c) \\ & - \left[ \frac{2(h+2r)}{3c^4}(h-r)^2 + \frac{2(h+r)}{c^3}(h-r) + \frac{2h}{c^2} + \frac{2}{3c} \right] \ln(h-r) \\ & + \left[ \frac{2(h-2r)}{3c^4}(h+r)^2 + \frac{2(h-r)}{c^3}(h+r) + \frac{2h}{c^2} + \frac{2}{3c} \right] \ln(h+r) \\ & - \frac{4hr}{3c^3} - \frac{8r}{3c^2} - \frac{4hr}{3c(h^2-r^2)} \end{aligned} \quad (6.27c)$$

### Lift force

The model of Cherukat and McLaughlin (1994) is adopted and the lift force is calculated based on the following correlation:

$$F_{L(C-L)} = \frac{\rho V_r^2 d_p^2 I_L}{4} \quad (6.28)$$

Where,

$$V_r = u_p - u_f = u_p - \mathcal{U} \quad (6.29a)$$

and for non-rotating particles,

$$\begin{aligned} I_L = & (1.7716 + 0.216K - 0.7292K^2 + 0.4854K^3) \\ & - \left( \frac{3.2397}{K} + 1.145 + 2.084K - 0.9059K^2 \right) \Lambda_G \\ & + (2.0069 + 1.0575K - 2.4007K^2 + 1.3174K^3) \Lambda_G^2 \end{aligned} \quad (6.29b)$$

Where,

$$K = \frac{d_p}{2l}, \quad \Lambda_G = \frac{\mathcal{U} d_p}{2V_r} \quad (6.29c)$$

## **6.6 Behaviour of particles in near-wall regime**

In this section, the discussion will begin with comparing the values of forces acting on the particle. Then the influence of the particle size and the particle-wall distance on the resultant force will be discussed. The agreement of the results of the proposed model with those in the literature will then be presented.

The gravity/adhesion forces tend to keep the particles attached on the wall whereas the lift force pushes the particle away from the wall. Figure (6.7) demonstrates the variation of lift, adhesive, and gravity forces of the Brownian particles as a function of particle diameter. The distance between the particle and the wall is very short and the particle almost lies on the wall, the lift force shown in the figure cannot resist the gravity/adhesion forces and the particle will therefore tend to attach to the wall. As the size of the particle increases, lift and gravity forces increase while the adhesive force decreases, see Figures (6.7) and (6.8). The particle now could entrain as a result of the increasing positive lift force. However, the increase in the gravity force could make the particle move toward the wall. In summary, the very tiny particles have more chances to deposit whereas the relatively larger particles have an opportunity to entrain.

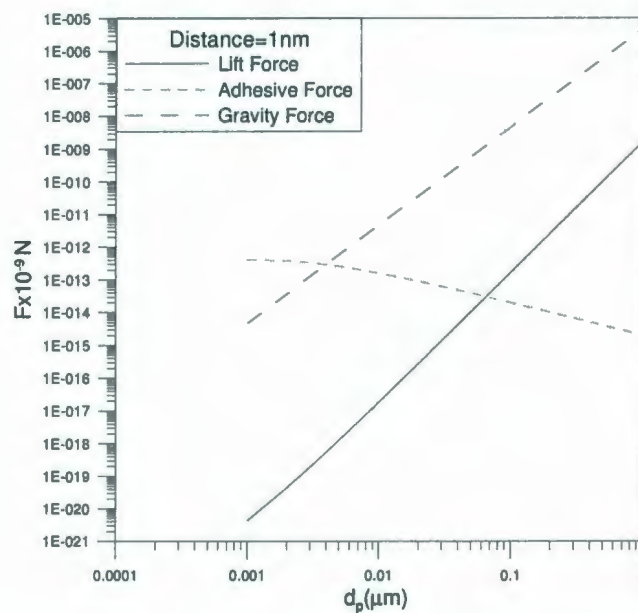


Figure (6.7) Variation of external forces for Brownian hydrate particles

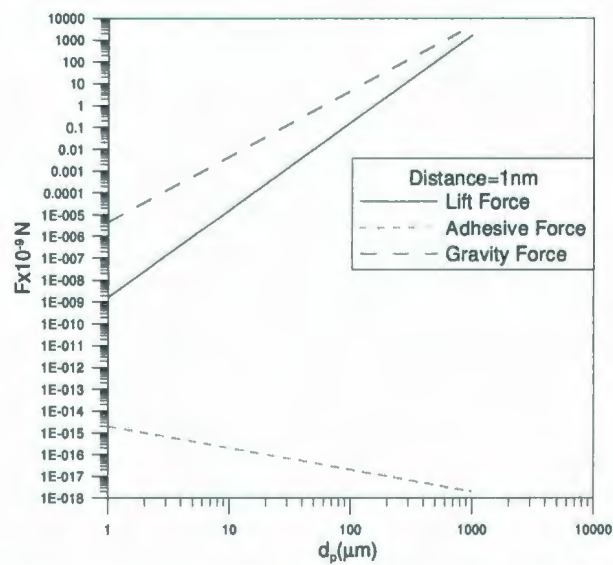


Figure (6.8) Variation of external forces for inertia hydrate particles

This conclusion is consistent precisely with the experimental studies of particles in the boundary layer region reported by Yung *et al* (1989). The interaction of the turbulence and the deposited particles within the viscous sublayer region was investigated through several tests. They carefully placed spherical particles of polystyrene and glass (50- $\mu\text{m}$  in diameter) on the wall so that the particles were completely submerged within the viscous sublayer. They were interested in the re-entrained particles by measuring the number of particles re-entrained in the viewing area at a given time and determined the ratio of the experimental number of particles re-entrained to the total number of particles under the burst area, which was identified as the cleaning efficiency. Their observation of the experiments showed that as the size of particles increased, the number of the re-entrained particles also increased. Based on these results they concluded that the turbulence-particle interaction in the viscous sublayer region is not responsible for the re-entrainment of the particles within the experimental range of  $0.5 < d^+ < 1.3$ , where  $d^+$  is the dimensionless particle diameter ( $d^+ = d_p u^* / \nu$ ). On the other hand, as  $d^+$  increases, the importance of particle re-entrainment is substantially increased. Part of their test results are summarized in Table (6.1).

**Table (6.1)** Experimental Results of Yung *et al* (1989)

$d_p$ ( $\mu\text{m}$ )	$d^+$	Re	No. of particles re-entrained experimentally per viewing area in 10-s interval	Ejection Angle ( $^\circ$ )
50	0.55	16,983	8	5.47
	0.585	18,460	30	
	0.635	20,306	37.8	
300	3.5	18,460	majority of the	15
	7.8	46,150	particles lifted up	30

Rashidi *et al.* (1990), conducted experiments to study the variation of particle size in the near-wall region. The objective was to better understand the influence of the particles on the dominant flow structures and the effect of these structures on the particle motion near the wall. Based on their observations during the tests in a horizontal channel, they suggested that the particle transport is mainly governed by the ejections originating from the lift-up and breakdown of the low-speed streaks in the wall region. They also proposed that the low-speed streaks observed near the wall are formed between pairs of longitudinal counter-rotating vortices. The particles accumulate but due to these vortex loops of the wall regions they are then lifted up, depending on their size, density and the flow Reynolds number, and ejected into the bulk of the flowing fluid. Later, the ejected particles returned toward the wall since their density was greater than the fluid density.

As these particles return to the wall region, some encounter wall ejections already in progress and are lifted up before reaching the wall region. The process repeats itself and dominates the particle transport in the flow direction.

Their experimental results showed that the particle-flow interaction is very dependant on the particle size. Their results can be summarized as follows:

As the particle diameter decreases below  $d^+ \approx 1$ , the particles falling beneath the viscous sublayer do not interact with the bursting process, the process of particle ejection into the bulk fluid as a result of vortex loops near the wall, and are rarely lifted up by the wall ejections.

### **6.7 Particle-wall distance**

Lift and adhesion forces vary with the distance between particles and the wall. The lift force increases when the particle-wall distance increases as shown in Figure (6.9). However the increment appears more clearly for tiny particles and at large size particle the lift force remains constant when the distance is short and starts to increase after a certain distance. This could be explained as follows:

The intensity of the vortices can easily dominate the weight of tiny particles even near the wall although the vortices strength is relatively low; hence the variation of the lift force with the distance is noticed from the wall. In turn, large particles should lie in the high strength regime in order for the influence of the lift force to become significant. Such influence occurs at a distance relatively far from the wall.

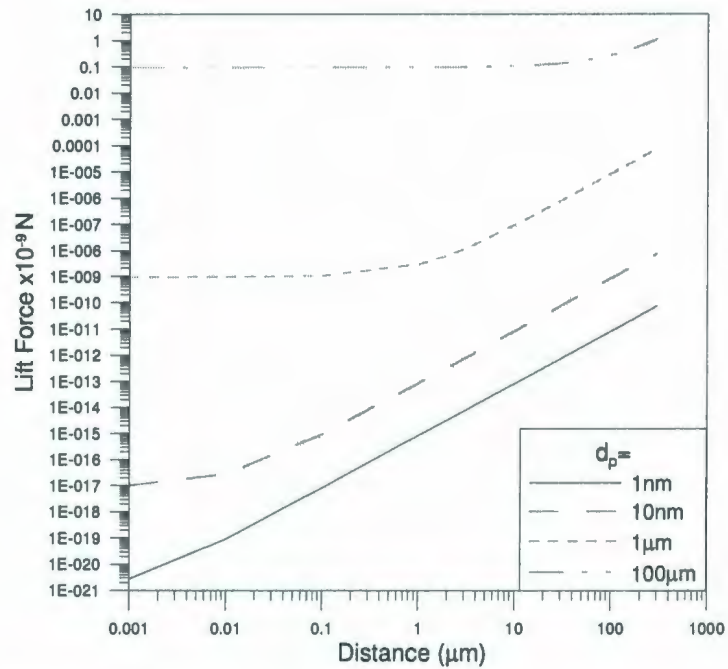


**Figure (6.9)** Influence of particle-wall distance on lift force

The van der Waals force is responsible for the adhesion and is inversely proportion to the particle-wall distance. Thus the strength of adhesion decreases as the distance increases as illustrated in Figure (6.10). However, for the same particle-wall space, the force becomes larger for larger particle sizes because the interaction potential between the wall and the particle increases.

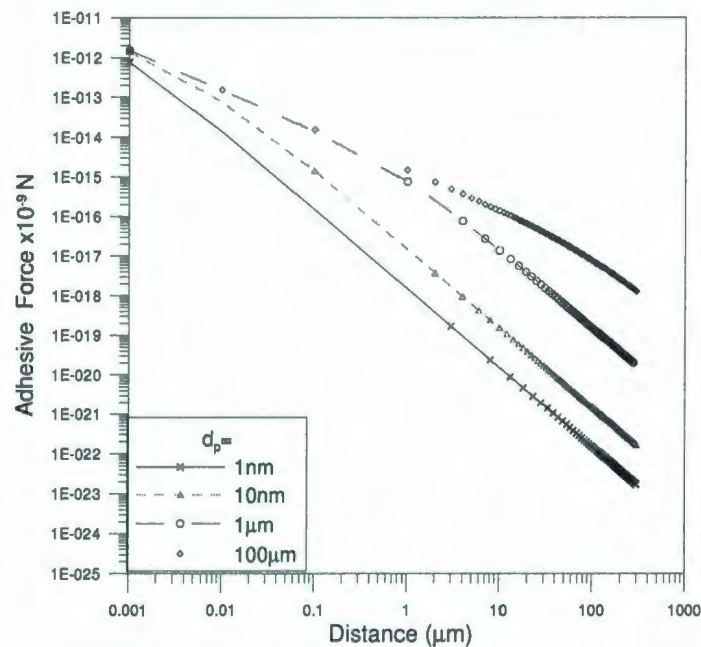


**Figure (6.10)** Influence of hydrate particle wall distance on adhesive force

Figure (6.11) shows the lift force as a function of particle diameter for the distance range from near-wall to the boundary layer limit. The conclusion is that on the one hand the particle can obtain higher value of the lift force when the distance becomes large, and on the other hand the variation of the lift force decays and eventually vanishes as the particle size becomes large. Hence, less influence of the particle-wall distance appears for large particles.

Similar conclusion can be made for the adhesion force. Figure (6.12) demonstrates the variation of adhesive force with the particle size for different particle-wall distances. Although the adhesion force increases as the distance decreases, the size of the particle also plays a significant role on the force magnitude by decreasing the force when the

particle is large. The net effectiveness of the distance and the particle size causes a peak value in the adhesion force curve.

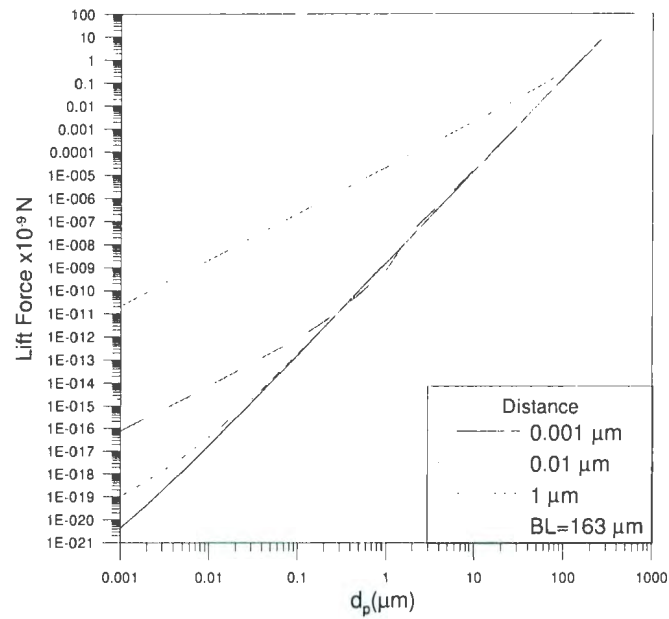


**Figure (6.11)** Lift force as a function of hydrate particle diameter at various distances

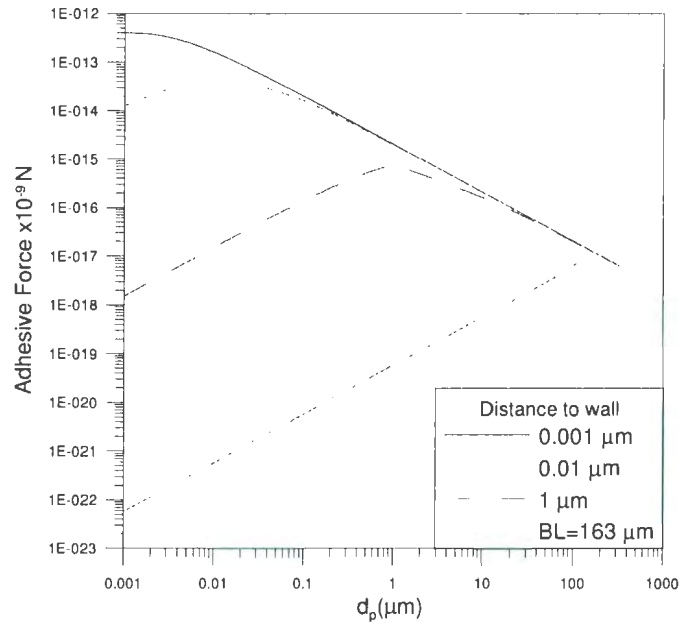


**Figure (6.12)** Adhesive force as a function of hydrate particle diameter at various distances

A graph representing lift and adhesive forces as a function of particle diameter for various particle-wall distances is shown in Figure (6.13). The equivalent lift to adhesion forces, the intersection point, occurs at smaller particle sizes when the distance increases.

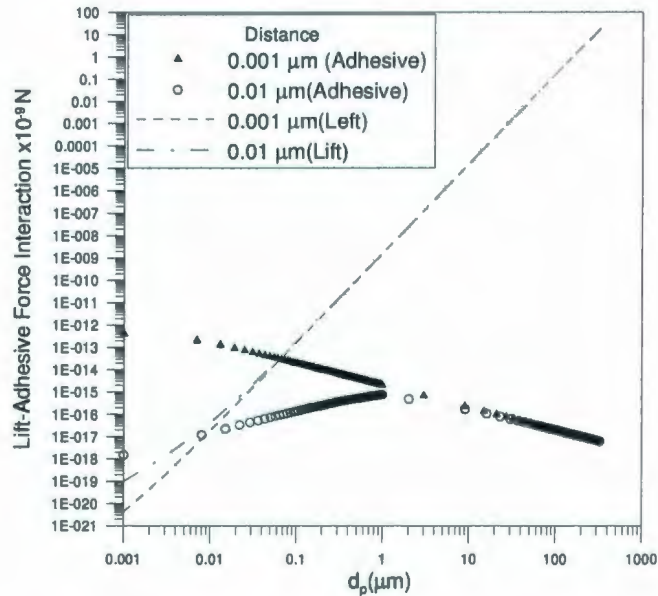


**Figure (6.13)** Lift-Adhesion Balance Point

### 6.8 Bouncing model

In many practical situations where multiphase flow is involved, particle-wall interactions play a major role in the overall dynamics of the flow. When a solid particle contacts a surface at low velocity, the particle loses its kinetic energy by deforming itself and the surface. At high velocities, part of kinetic energy is dissipated in the deformation process (plastic deformation), and part is converted elastically to kinetic energy of rebound (Hinds, 1999). If the rebound energy exceeds the adhesion energy, the particle will bounce away from the surface.

The problem of particle bounce has been experimentally and analytically reported for solid and droplets as well. The results concerning the bouncing of a solid sphere on a wall in air as well as in various fluids have been proposed by numerous researchers. The most recent experiments for such system reported by Joseph *et al.* (2001) and Gondret *et al.*(2002), have clearly demonstrated that the *restitution coefficient*  $e$  (the ratio of the velocity after the rebound to the approach velocity) can be scaled by the particle Stokes number. This conclusion matched with the analytical derivations of Davis *et al.* (1986) using the lubrication theory. A no-rebound situation ( $e=0$ ) is observed below a critical Stokes number ( $St_c \approx 10-15$ ). The *restitution coefficient* rapidly increases after the transition at  $St_c$  and monotonically reaches an asymptotic value close to the value of  $e$  obtained in air where viscous effects are supposed to be negligible during the interaction with the wall ( $St_c > 10^4$ ) (Legendre, 2006).

There are two approaches used in defining the conditions at which the particle could bounce. The first approach is based on the limiting adhesion or kinetic energy whereas the second approach defines a critical velocity  $V_c$  for which bounce will occur if that velocity is exceeded.

The surface potential energy is given by Dahneke (1971):

$$E = \frac{d_p A}{12y_0} \quad (6.30)$$

Where,  $A$  is the Hamaker constant and  $y_0$  is the equilibrium separation distance of the particle from the surface, which depends on the scale of surface roughness. For smooth surfaces, the distance is usually assumed to be 0.4 nm (Hinds, 1999).

Friedlander (1977) described the process of bouncing as a balance of energy before and after impact and proposed a relation between the velocities of the particle before and after impact. The expression is given as:

$$\frac{v_2}{v_1} = \left[ e^2 - \frac{E(1-e^2)}{\frac{m_p v_1^2}{2}} \right]^{1/2} \quad (6.31)$$

Where,  $m_p$  is the mass of the particle and  $e$  is the *restitution coefficient*. The critical approach velocity corresponding to  $v_2 = 0$  is given by:

$$v_{1c} = \left[ \frac{2E}{m_p} \left( \frac{1-e^2}{e^2} \right) \right]^{1/2} \quad (6.32)$$

It is important to note that the particle rebound model outlined here was developed for dry interface. The nature of interaction changes dramatically when the surface is coated with a liquid layer since the surface tension due to liquid bridging becomes a significant adhesion force (Kvasnak *et al.*, 1993).

The *restitution coefficient*  $e$  provides a global description of the bounce including the effect of the wall without describing the detailed action of all physical mechanisms involved: deceleration due to hydrodynamic interaction, deformation, film drainage, and restitution of initial shape (Legendre, 2006).

Using the analogy with a dissipative mass-spring system, Legendre *et al.* (2005) found that for droplets, the coefficient of restitution evolves as:

$$e = e_{\max} \exp\left[-\frac{\beta}{St}\right] \quad (6.33)$$

Where,  $St$  is defined as the Stokes number of the particle away from the wall by an order of boundary layer thickness.

$$St = \frac{(\rho_p + 0.5\rho)U_g d_p}{9\mu} \quad (6.34)$$

Where,  $\rho_p$  is the particle density,  $\rho$  is the fluid density,  $\mu$  is the fluid viscosity.  $\beta$  is a parameter that includes the viscous effects of the film drainage and according to the experimental results from many available sources in the literature for spherical drops and solid spheres colliding both in air and in different liquids, takes the value of 35.  $e_{\max}$  is the maximum *coefficient of restitution* that can be reached by the particle. In practical situation,  $e_{\max}$  is the value measured in air. Measurement done by Richard and Quéré (2000) obtained a nearly constant value for  $e_{\max} = 0.91$  for collisions in air for both solid particles and drop.

## 6.9 Summary

The flowchart presented in Fig (6.14) summarizes the procedure of the particle migration and process of deposition in turbulent flow together with the appropriate equation(s) used in describing such process. As particles travel in the fully turbulent region, deposition velocity is evaluated (depending on their sizes) and used to determine collection factor and the number of particles reaches the wall each time step.

In the sublayer region, again the size of the particle is used to direct the phenomena of the deposition to the proper model of deposition process, which is either the balance of the forces experienced by the particle or the probability of bouncing.

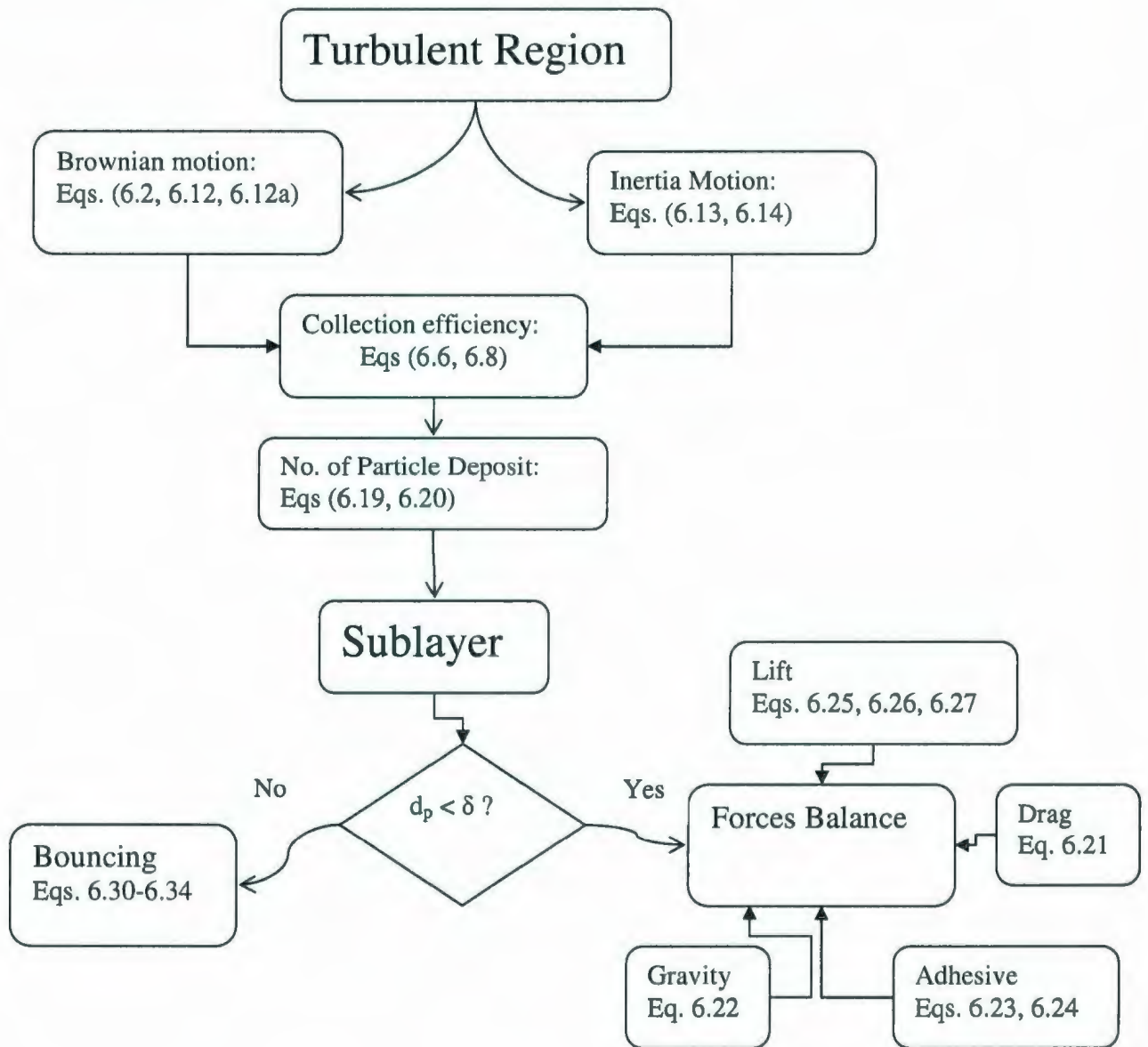


**Figure (6.14)** Flowchart of deposition model

## 6.10 Conclusion

The mechanism of particle deposition is presented and discussed in this chapter. The following conclusions could be made as a summary of the chapter:

- Two motions are exhibited by the particles depending on their sizes, namely: the Brownian and impaction motion. The particle size for distinction between the two motions is  $\sim 1 \mu\text{m}$ .
- The deposition rate in the non-continuum region decreases as the size of the particle increases whereas it increases with the particle growth in the impaction region.
- The minimum numbers of particles that deposit and reach the boundary layer are those that have sizes of about  $1 \mu\text{m}$ .
- The very tiny particles tend to deposit whereas the relatively larger particles are probably more susceptible to be entrained from the boundary layer near the wall.
- For certain particle-wall distances, adhesive forces increase to a peak with increasing particle size.

## **CHAPTER 7**

### **Experiment setup**

#### **7.1 Preliminary Experiment Setup**

Before constructing the actual apparatus for natural gas/hydrocarbon tests, we decided to perform preliminary tests using saturated air as the working fluid. The purpose of these tests was to obtain a better understanding of the test system by monitoring ice particles formed and deposited in the transparent tubes. The following section outlines the system setup.

##### **7.1.1 Apparatus and Procedures**

As illustrated in Figure (7.1), the compressed air is saturated by bubbling it through the water container, cooled down through cooling coil to drop the temperature to just above 0 °C, and then passed through separator to separate the air stream from any liquid droplets that might be formed during the cooling process. After that, the air flows through the orifice, which is connected to the tube where the accumulation is monitored, and finally the stream passes through a flowmeter before exiting to the ambient. The tests were performed at the Faculty of Engineering and Applied Science of Memorial University of Newfoundland using the environmental chamber located in the Fluids Lab. The entire system but the air source and the saturated vessel were placed inside the environmental chamber.

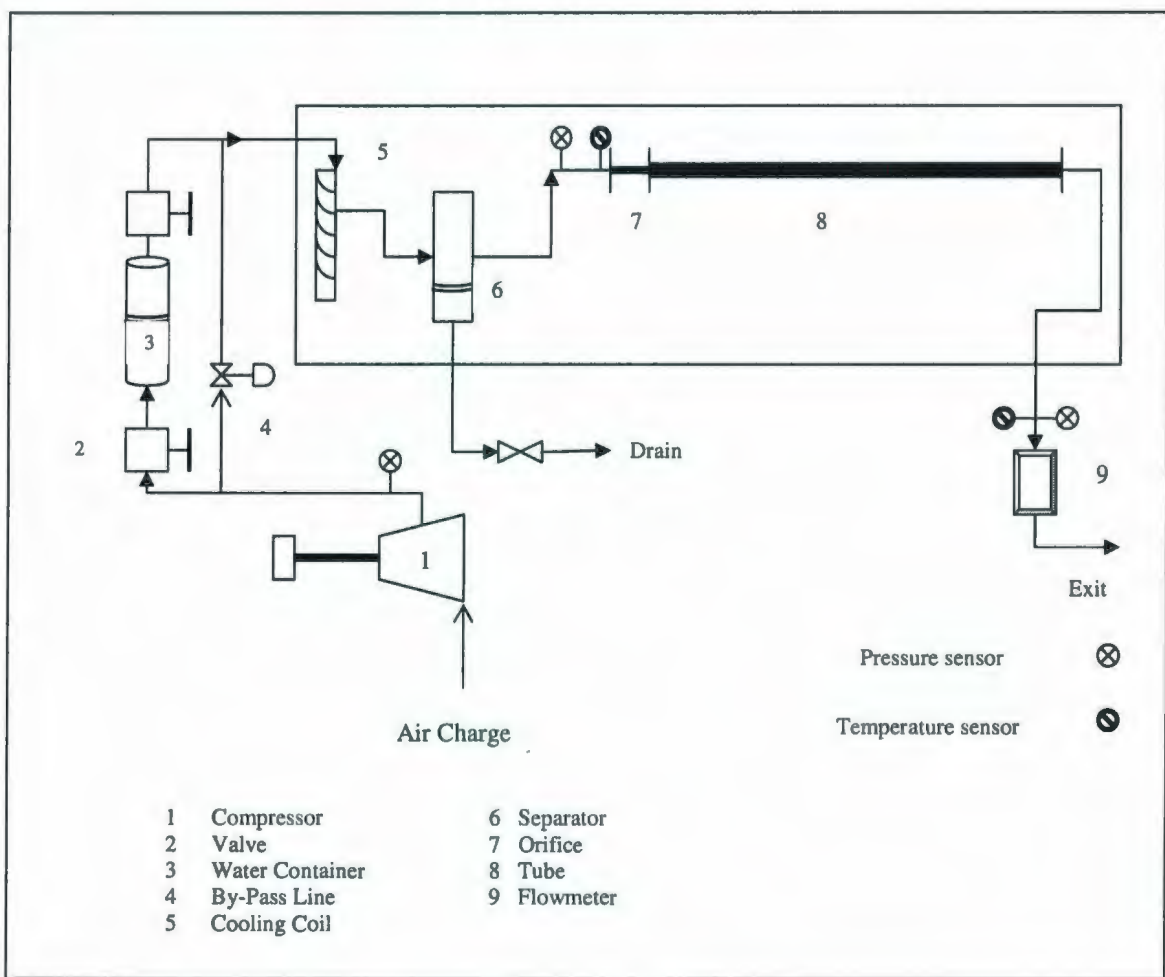


**Figure (7.1)** Schematic of deposition apparatus using saturated air

The compressed air pressure was measured right after the compressor. The orifice inlet pressure and temperature were directly measured using the attached pressure gauge and temperature sensors. Information about pressure loss through water container, cooling coil, separator, and all connections were recorded. No temperature measurement sensor was placed at the orifice outlet as any measuring sensor in this position could perturb the air flow and affect the process of condensation and/or crystallization. The pressure and temperature after the orifice were calculated using the procedure detailed in Appendix C.

The original plan was to observe ice particles formed on the tube wall. However, only water droplets (as opposed to ice particles) could be observed. Numerical analysis using computational fluid dynamics software (the Fluent software was used here) was conducted to predict the temperature after the orifice. Figure (7.2) shows the variation of air temperature along the orifice region.

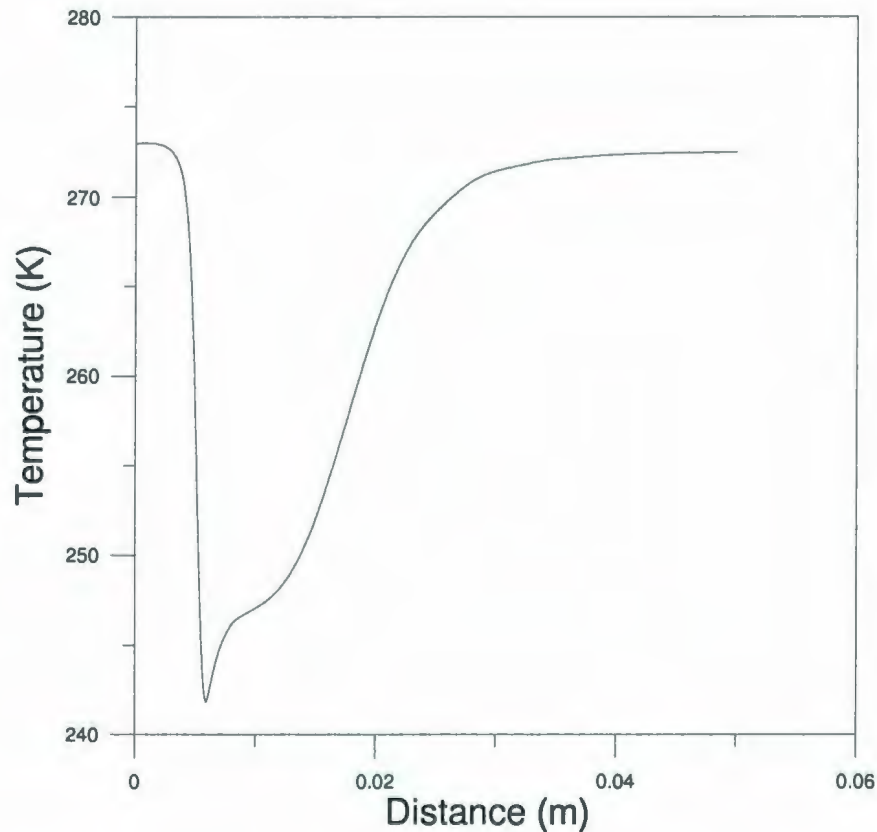


**Figure (7.2)** Numerical prediction of temperature variation through an orifice

The plot proves that although the air temperature drops sharply within the orifice, it increases rapidly right after the orifice and reaches almost orifice's inlet temperature.

Therefore, there is no sufficient time for vapour to nucleate and crystallize. Raising the flow rate (by increasing the orifice inlet pressure) decreases the orifice exit temperature.

However, the time that the fluid needs at this low temperature is still inadequate due to exposure to relatively high temperature of the chamber, i.e. the air stream is affected by a significant driving force. The temperature of the chamber was intentionally kept above zero to avoid plugging in the cooling coil. The observed water droplets however were an indication of where the ice particles were likely to form.

In order to see actual ice particles, it was concluded that the chamber temperature should be kept low enough to make the nuclei formed in the orifice exposed to a sufficient driving force in the tube suitable for stabilization and growth. The conclusions reached at this stage helped to plan and design the actual system built at the Centre for Marine CNG Inc. (see Section 7.2). The improved environmental chamber, shown in Figure (7.3), was constructed such that the temperature of the cooling coil and the tube could be controlled independently in two separate compartments. In the two separate chambers the actual natural gas or a hydrocarbon gas with similar behaviour (e.g., propane) can be used as the working fluid in the tests for hydrate formation and deposition studies. The first chamber is set around equilibrium temperature and contains the cooling coil and separator while the second chamber contains the rest of the system where temperature could be set at sufficiently below the equilibrium temperature, so the formed hydrate could be under driving force as it moves through the tube. Thus, the nucleation process could be enhanced.

## **7.2 Improved Experimental Apparatus**

The main objective of the experimental work was to establish, by physical evidence, the role played by the various forces discussed in previous chapters on particles deposition. The method adopted to examine this effect was to form hydrate particles as the result of a contraction to flow passage and record the distance required by the particle to deposit on the wall

### **7.2.1 Flow Circuit**

The experimental apparatus is composed of transparent tubes approximately 2m in length and diameters ranging from 6.35 to 19.05 mm (1/4" to 3/4"). The orifice had a diameter of 2.54 mm (0.1") and other equipment pieces are listed in Figure (7.3). Two main test zones were suggested, namely: the starting or gas saturation loop, which is designated for cooling the gas and saturating it with water at the desired temperature, and the main hydrate formation loop, where the gas passes through the orifice and the tube, and the place where hydrate particles are deposited.

In the starting loop, the charged gas is mixed with the cool gas in a separator container (9) before being routed to the compressor. In order to bring the gas temperature down, it is then passed through the cooling coil (5) located in the environmental chamber (9). This process continues until the compressor's exit temperature reaches a stable value. The gas, at this time, will be directed to the main loop by opening Valve (2).

The gas then moves through the Container (3) filled half with water to saturate the gas, the cooling coil to bring the gas temperature to the equilibrium level, and the Separator (6) to trap any droplet that could form during the cooling process in the coil. At this point, the gas is at equilibrium temperature and ready to flow through the system. It is worth to note here that the temperature of the small environmental chamber is adjusted around the gas hydrate formation temperature.

The pressure and temperature of the gas are monitored once again upstream of the orifice and the tube to confirm that its conditions are suitable for hydrate formation. The orifice and the tube are located in a separate chamber with an independent temperature control system. As the gas flows through the orifice its temperature falls rapidly. Although the gas temperature could increase after leaving the orifice, as concluded from the numerical simulation mentioned earlier, the low temperature of the second chamber will keep the gas below the equilibrium hydrate formation temperature. Figure (7.4) shows some photos of the actual system.

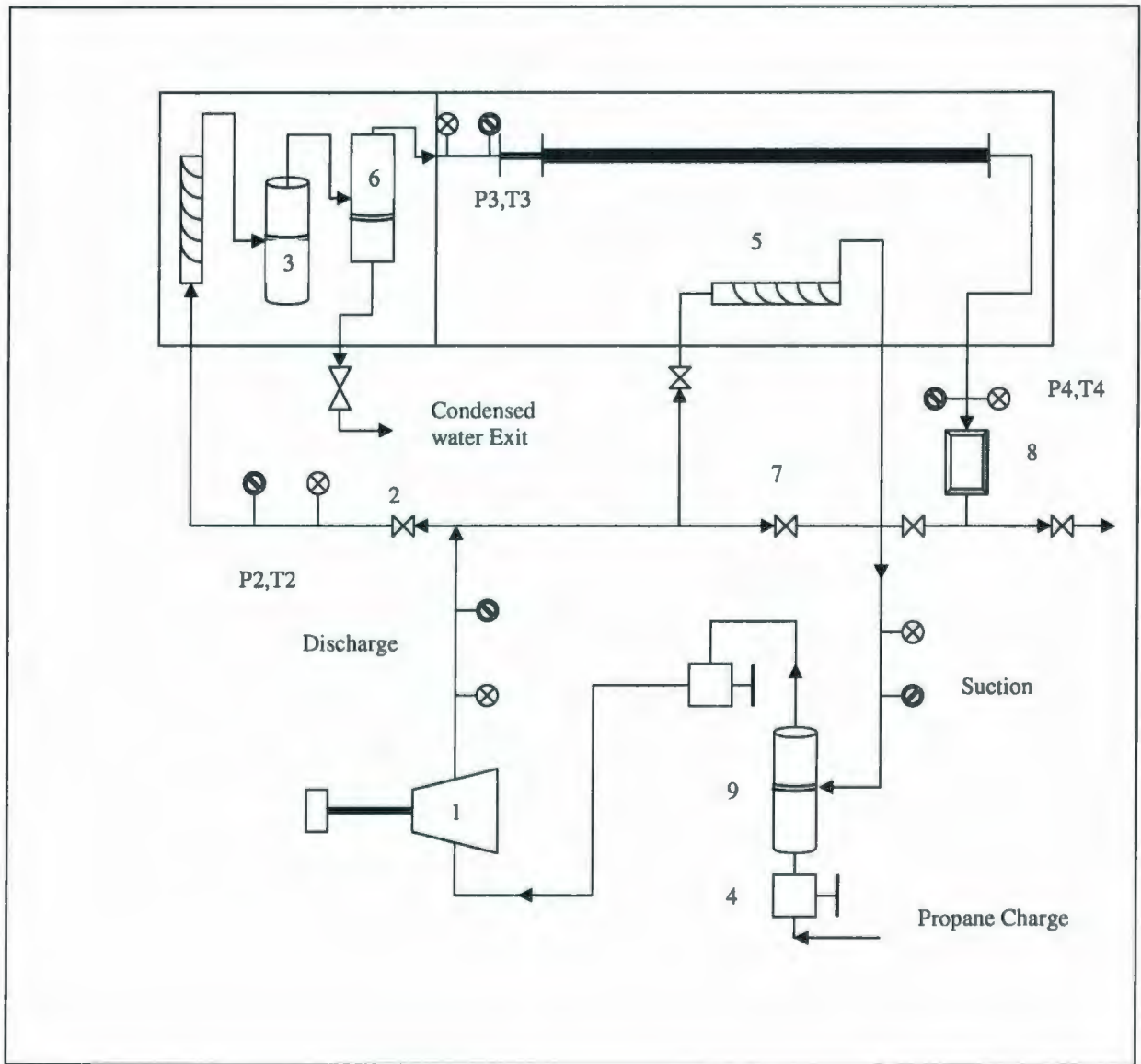
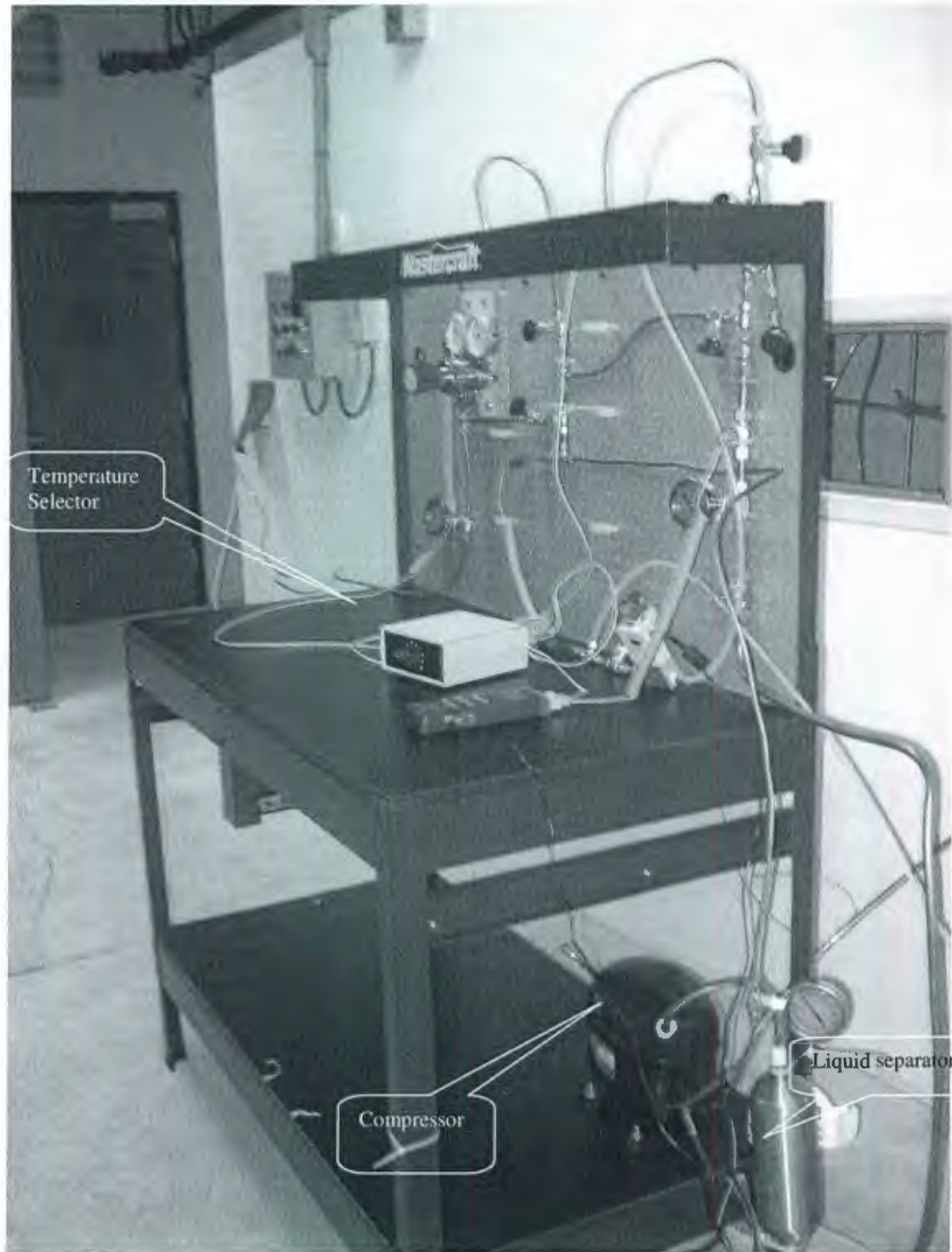


**Figure (7.3)** Schematic of improved experimental system using propane as carrier gas

- |                       |                       |
|-----------------------|-----------------------|
| 1. Compressor         | 6. Separator          |
| 2. Valve              | 7. Valve              |
| 3. Gas saturator      | 8. Flow meter         |
| 4. Gas charging valve | 9. Liquid trap/filter |
| 5. Cooling coil       |                       |

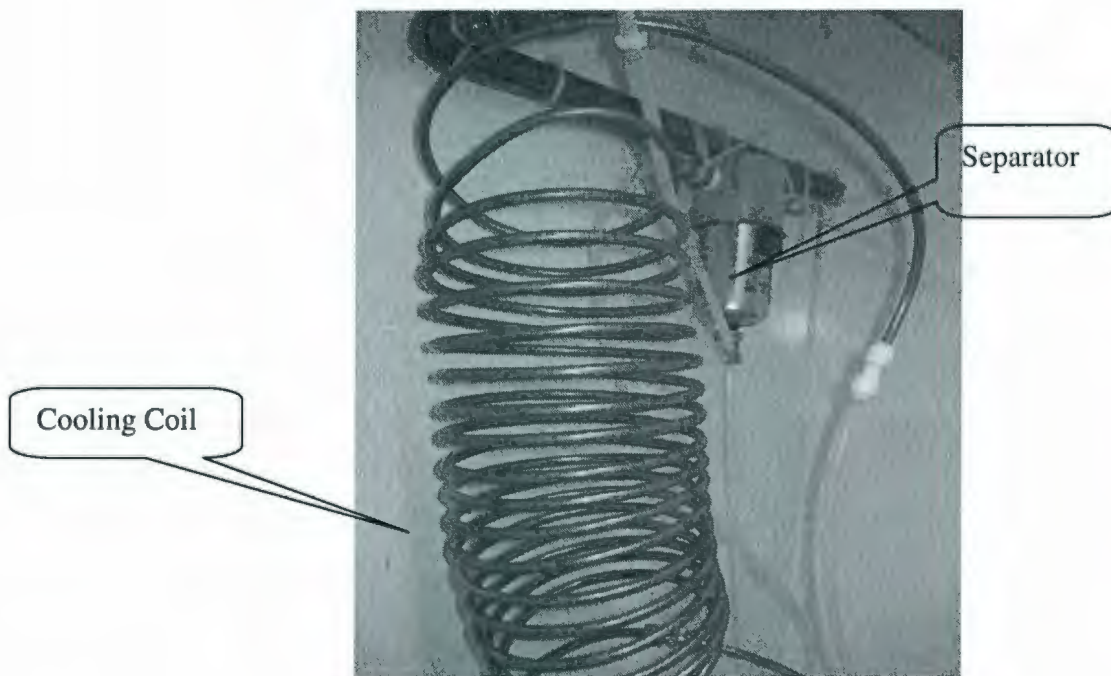


Temperature Selector

Compressor

Liquid separator

(a)



(b)



(c)

<p><b>Figure (7.4)</b></p>	<p>Components of the gas hydrate apparatus: a) b) parts located in the small chamber (coil, separator, saturator); c) Parts located in the large chamber (orifice, pipe)</p>
----------------------------	--

## Chapter 8

### Modelling of Hydrate Deposition Location for Single Particle

In this chapter the procedure to determine the particle deposition distance is outlined. A number of case studies will be discussed. The model predictions for water-air system will be first examined and then the results of model predictions for hydrocarbon hydrate formation will be compared with the experimental data.

#### A. Water-Air system

The approach taken in this research to determine the deposition distance can be categorized into three areas as discussed below:

##### 8.1 Flow Simulation-CFD results

Since the model of nucleation needs the distribution of fluid properties, e.g., temperature, velocity, pressure, along the pipe, the governing transport equations of air-vapour mixture should be numerically solved using commercial software (the FLUENT software was used in this research). However, it is first required to define the system graphically and generate a simulation grid structure using a meshing tool. The GAMBIT software was used for grid generation.

The geometry used in this study (Figure 8.1) is a simplified version of the actual orifice-pipe system, with the axisymmetric assumption. The dimensions of the orifice and the pipe are shown in Figure (8.1).

For the FLUENT air-vapour case, a grid with 575 340 quadrilateral cells was used. Good initial grid design relies largely on an insight into the expected properties of the flow such as boundary layer, point of separation, or abrupt variation of a property. The quality of the mesh plays a significant role in the accuracy and stability of the numerical computation. Obviously, the goal of any numerical simulation should be the optimization of both the discretization scheme as well as the grid generation scheme.

One of the most powerful techniques used recently to achieve this task is the *Multigrid Scheme* (Patankar, 1980). The idea of a Multigrid algorithm, which is considered in the present numerical technique, is to accelerate the convergence of a set of fine-grid discrete equations by computing corrections to these equations on a coarser grid, where the computation can be performed more economically. This process is applied recursively to an entire set of coarse-grid levels.

Since the boundary layer ( $\delta$ ) in the orifice is of interest in the present study, a non-uniform mesh was used in the  $y$  direction, and the smallest elements were placed close to the orifice wall. The parameters used were: first row  $a=0.1\delta$ ; aspect ratio, the ratio of the two consecutive mesh thicknesses, ( $t_{i+1}/t_i= 1.2$ ) and the depth of the boundary layer meshing region  $> \delta$ . Starting from the wall, the height of the first grid row should be less than the boundary layer thickness to describe the flow in that region more precisely. A structured grid with 575 340 cells was used for the calculations, resolution was found to be independent of cell dimensions, and solutions were grid independent.

The solution algorithm for the non-linear algebraic equations involves:

- The linearization of the discretized equations and solution of the resultant linear equation system to yield updated values of the dependent variables starting with a given initial value and boundary conditions;
- The update continues until the scaled relative difference between two successive iterations has been reduced below a user-set threshold. In this study, the threshold value was set as:

$$\frac{|\varphi^{k+1} - \varphi^k|}{\varphi^k} \leq 10^{-3}, \text{ where } \varphi^k \text{ represents temperatures and velocities of the } k^{\text{th}} \text{ iteration.}$$

The computational domains and the partial differential equations describing the flow were discretized before being solved. The solution process means solving the governing partial differential equations (mass, momentum, energy, and k-Epsilon). The control volume technique converts these equations into a set of algebraic equations that can be solved numerically, resulting in a solution, which satisfies the governing equations in every control volume in the computational domain.

FLUENT uses an upwind/central differencing scheme, in which the convection terms are discretized using upwinding, and the diffusion terms are centrally differenced. Second order schemes include the second order terms of the Taylor series expansion of the partial differential equations, and are therefore, more accurate. The SIMPLEC method of interpolation (Patankar, 1980) was employed for the pressure-velocity coupling of all simulations. The second order interpolation scheme was applied to calculate the pressure. The details of these methods can be found in Patankar (1980) and FLUENT User's Manual (2002).

The boundary conditions for the saturated air case are listed in Table (8.1), which represents the data measured under the experiments' conditions.

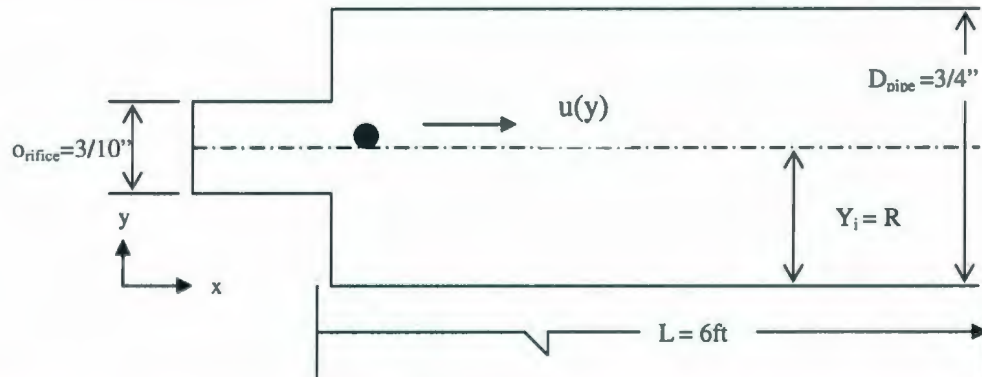


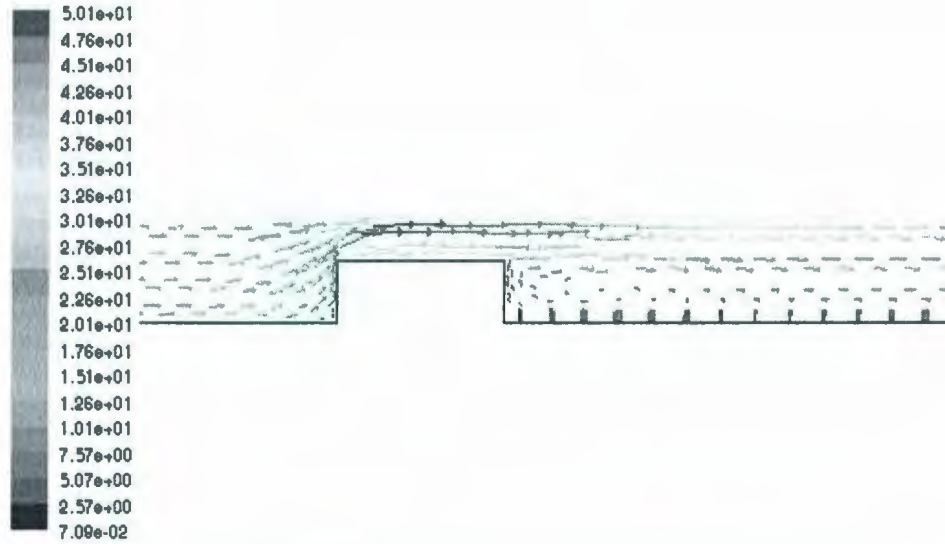
**Figure (8.1)** Schematic of the saturated air case study (identical dimensions of the experiment)

**Table (8.1)** Boundary conditions for saturated air simulation

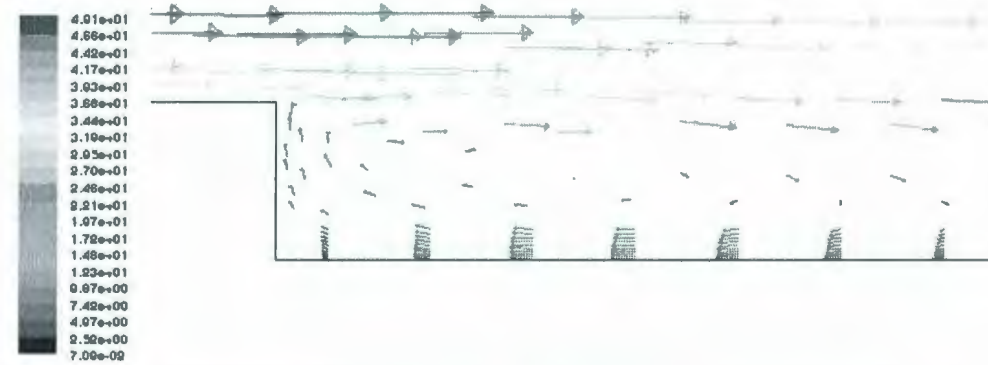
	Parameter	Value	Unit	description
Inlet	Pressure	$8.96 \times 10^4$	Pa	gauge
	Total temperature	273	K	
Exit	Pressure	$2.35 \times 10^3$	Pa	gauge
	Total temperature	300	K	
Lateral Wall	temperature	271	K	Isothermal

Default values were used k-epsilon parameters. Figure (8.2) illustrates the velocity vector of the air coloured by the velocity magnitude in the vicinity of the orifice region. The enlargement of this region could demonstrate a better view of the flow vortices and circulation right after the orifice. Figure (8.2c) show the temperature contours inside of the orifice. Due to the variable temperature within the orifice, ice particles with diverse critical sizes may form as a result of different driving forces. This can also be interpreted as the flow leaving the orifice may contain a

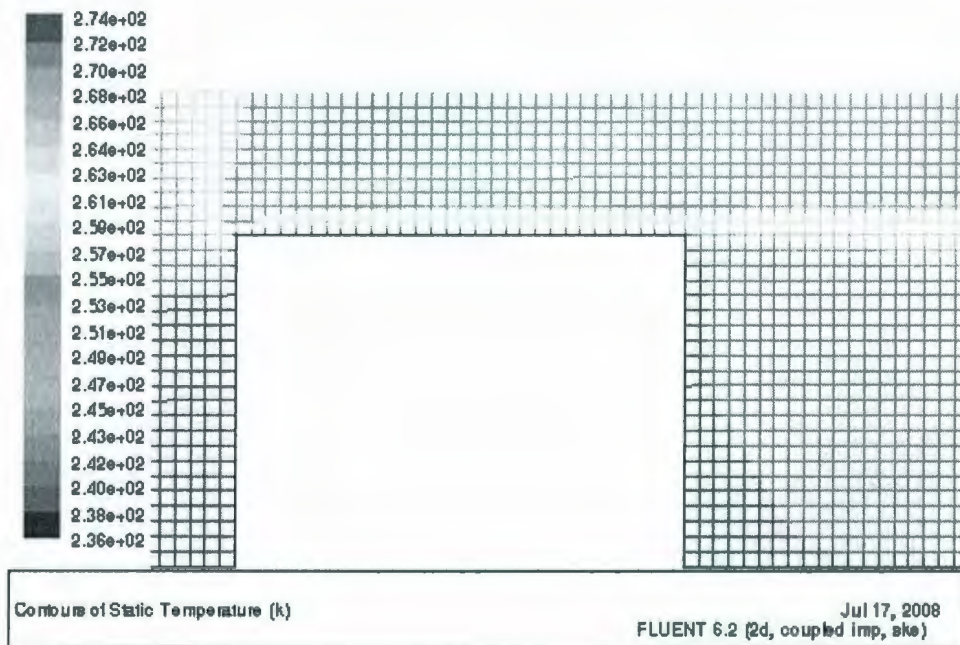
wide range of particle sizes. This conclusion will be further analyzed in the subsequent discussions.



(a)



(b)



(c)

**Figure (8.2)** Velocity vector and temperature contours generated by CFD simulation for water-air Case Study: (a) Velocity vector in the orifice region; (b) Enlargement to show circulation; (c) Temperature contours inside the orifice

## 8.2 Nucleation and Growth of Ice Particles

The data obtained from the FLUENT software was used to describe and estimate the process of nucleation and growth of the ice particles. Based on the analysis discussed in Chapter 4 and using mass transfer as the predominant process of nucleation and growth, parameters used for describing the processes are listed in Table (8.2).

**Table (8.2)** Parameters used in calculating  $\beta_1$  and critical radius for ice

Parameter	Value*
$n_v$	0.067
$Sh$	2.009
$D$	$1.636 \times 10^{-1}$ (cm <sup>2</sup> /s)
$\gamma$	$2.68 \times 10^{-3}$
$\gamma_{eq}$	$2.49 \times 10^{-3}$
$\sigma$	0.033 (N/m)

\*See Appendix E for typical calculations

The variation of the particle size and its growth rate with time for the conditions listed in Table (8.2) are now presented. Figure (8.3) shows the growth rate of ice particles in micrometer scale as a function of time. The growth starts with a very fast rate after the ice particle becomes nucleated and slows down as the time elapses. That means the ice particle growth rate decreases with particles size. Hence, the time required for ice particles to grow to several microns is relatively long; see Figure (8.4).

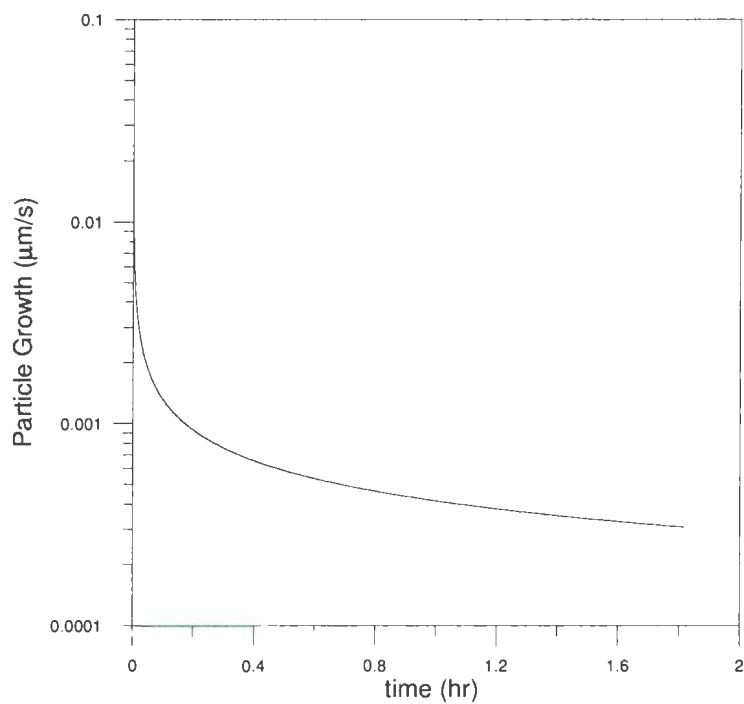


**Figure (8.3)** Growing rate for ice particle as a function of time

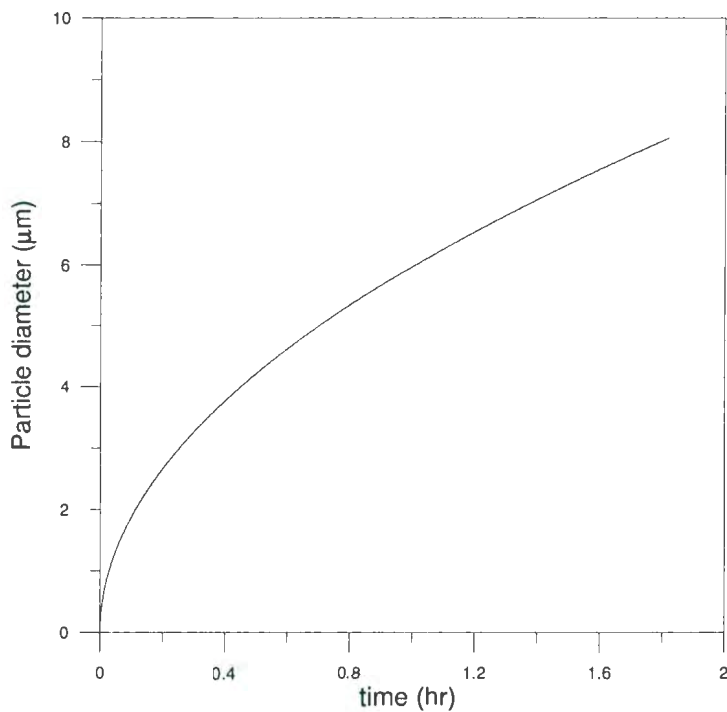


**Figure (8.4)** Diameter for ice particles as a function of time

Based on the correlation of the particle critical size, Eq. 4.10, particles formed in the orifice have different values of critical sizes. This could also be due to the fact that the temperature distribution inside the orifice is not uniform, as also mentioned in Section 8.1. The temperature of the flow inside the orifice ranges from 235 to 272K. Accordingly, the critical sizes would be 11-13 nm (calculated through the use of Eq. 4.10). Since the measurement of the actual nucleus (critical particle) size was not possible in this research, the analytical correlations of the **Particle Distribution Function**, Eq. 4.26, presented in Chapter 4, was used.

Figure (8.5) illustrates the number of particles in dimensionless form (using Eq. 4.26) as a function of dimensionless particle radius at time equal zero (nucleation time). The graph proves that the distribution of the particles contains different sizes; in particular particles with radii larger than the critical radius. It will be confirmed analytically later that the size of the particles just after the orifice are neither identical nor all at critical size, rather large sizes (several microns) could also exist. Besides, due to large amount of particles formed, the probability of particle-particle attachment is possible and even larger sizes (up to hundreds of microns) could form.

Hence the assumption made here is based on the conclusion that the particles leaving the orifice have different sizes and the approach used to describe the deposition model in this research is based on this fundamental hypothesis.

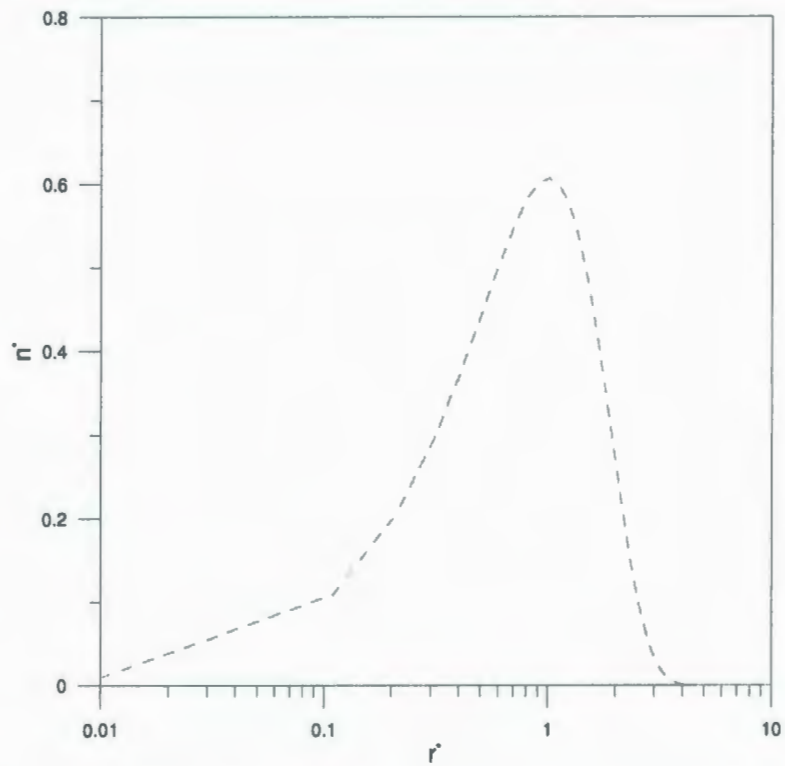


**Figure (8.5)** Particle distribution as a function of its size

### 8.3 Calculating the distance of the deposition

According to the proposed model, the procedure for calculating the distance traveled by a single particle before depositing on the wall could be summarized as follows:

- The deposition velocity is first determined using the model of Wells and Friendlander (Crowe, 2006).
- The time required for the particle to reach the sublayer region can be found from:

$$t = \frac{y_i}{V_d} \quad (8.1)$$

Where,  $y_i$  is measured from the tube wall.

- The traveling distance in the turbulent region, assuming the initial velocity of the particle is equal to the fluid velocity, becomes:

$$X_1 = u(y_i) \cdot \frac{y_i}{V_d}; \text{ where, } \frac{U_\infty - u(y_i)}{u^*} = 2.5 \ln \frac{R}{y_i} \quad (8.2)$$

- In the sublayer region, the particles smaller than the thickness of the boundary layer could migrate further as a result of external forces. Hence, the total distance from the initial position would be:

$$X_t = X_1 + X_\delta \quad (8.3)$$

- When particles larger than the sublayer thickness, the bouncing distance ( $X_B$ ), the distance taken by the particle to settle as a result of rebound, is added to the distance traveled in the turbulent region.

$$X_t = X_1 + X_B \quad (8.4)$$

### 8.3.1 Trajectory of a single particle ( $d_p < \delta$ )

The following data, obtained from the actual saturated air test, is used as the initial conditions in the simulations to track and calculate the distance from the initial position of a single ice particle ( $x_0, y_i$ ) to the point of resting on the wall ( $X_t, 0$ ):

Smooth pipe:  $D_{pipe} = 20 \text{ mm}$ ;  $f = 0.023$ ;  $Re \sim 32800$  and  $\delta \sim 56.7 \text{ } \mu\text{m}$

Fig. (8.6) illustrates the deposition of a 10- $\mu\text{m}$  particle initially located at the centre of the pipe where  $u(y_i) = U_\infty$ . Using the conditions mentioned earlier, the results show that the particle travels  $\sim 7\text{m}$  before entering the boundary layer (BL) region. In the BL, the particle moves  $\sim 1\text{mm}$  then deposits on the wall. Although the particle migration in the BL region is minor for this particular

size, very small particles tend to travel a significant distance in this region. For instant particles with  $0.1 \mu\text{m}$  diameter travel  $\sim 5,995 \text{ m}$  in the turbulent flow and  $\sim 1.5 \text{ m}$  in the BL region.

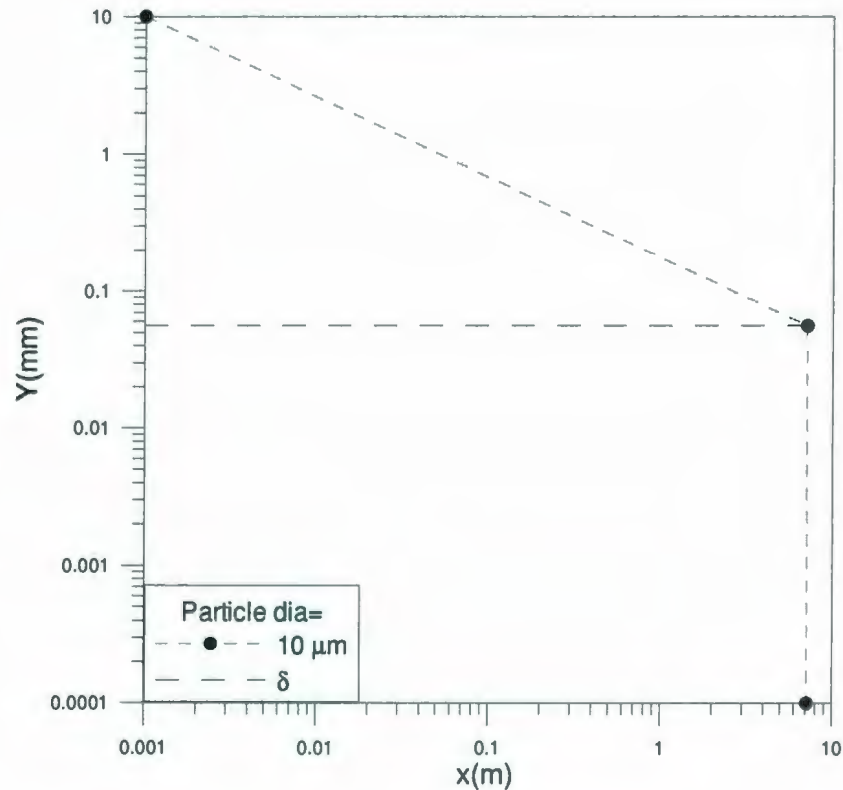


**Figure (8.6)** Deposition distance of a  $10\text{-}\mu\text{m}$  particle calculated based on influence of flow motion and force balance

### 8.3.2 Trajectory of single particle ( $d_p > \delta$ )

Particles having sizes greater than the sublayer thickness experience bouncing process as a result of collisions in the wall region. The total distance that the particle travels is now equivalent to the migration distance in the turbulent regime plus the distance traveled due to bouncing effect, (Eq. 8.4). Fig. (8.7) shows the deposition distance as a function of the particle size for particle diameters greater than the sublayer thickness. The three curves in this figure indicate

respectively: the distance caused by bouncing, the distance traveled in the turbulent region, and the total distance traveled by the particle. The figure also shows that as the particle becomes larger, the inertia of the particle increases and hence the bouncing distance will shrink.

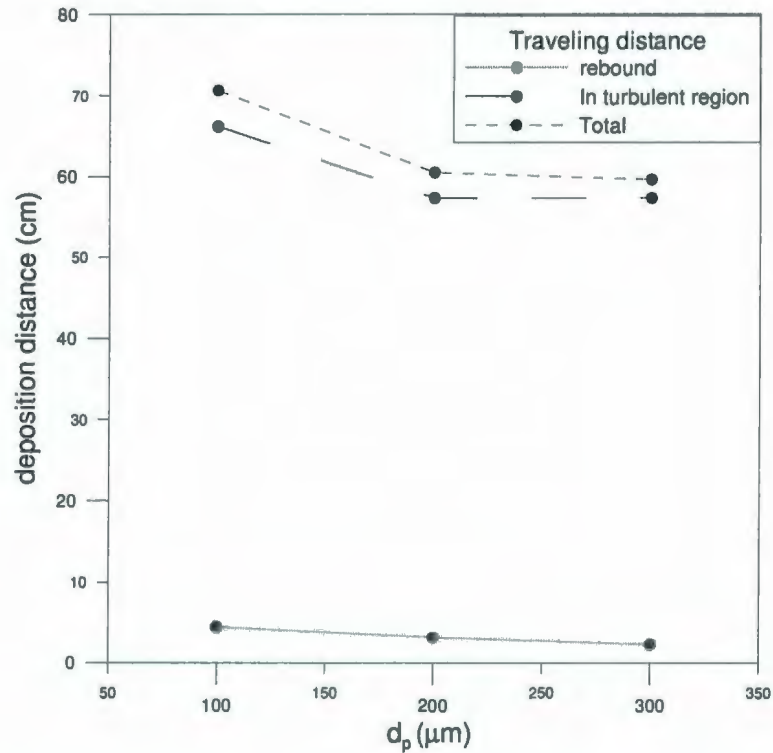


**Figure (8.7)** Deposition distance of particles ( $d_p > \delta$ ) calculated based on influence of flow motion and bouncing

A very important conclusion is shown in Fig. (8.8), which represents a combination of results shown in Figures (8.6) and (8.7). The reduction in the total deposition distance will asymptotically approach a certain value. Hence the conclusion reached from Fig. (8.6), which stated that the deposition distance decreased dramatically following an increase in the particle size, should be corrected as follows: For particles larger than a certain diameter, called hereafter *deposition critical size*, there is no significant influence of the particle size on the deposition

distance. Consequently, particles having sizes greater than the *deposition critical size* will deposit at the same position. In this example, (ice formation studies), particles larger than 200  $\mu\text{m}$  will deposit almost at the same location ( $\sim 0.6$  m). Therefore the deposition critical size for this example is about 200  $\mu\text{m}$ . Therefore deposition will start at about 0.6 m and all smaller particles will travel further until they become large enough to start settling on the wall.

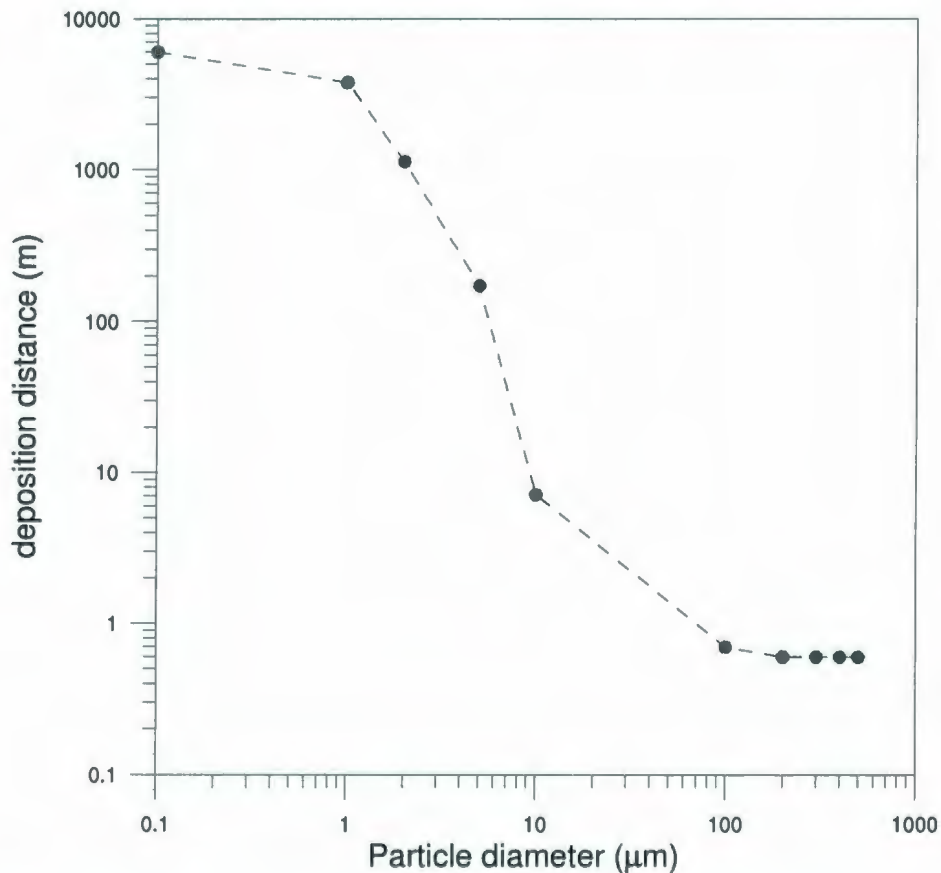


**Figure (8.8)** Deposition distance as a function of particle size initially located at the pipe centerline

The effect of Reynolds number is now discussed to understand how the location of deposition would be affected. Figure (8.9) illustrates the particles deposition spot as a function of particle size for different flow Reynolds numbers for the ice deposition tests. As seen in Figure (8.9), the small particles are influenced by the main fluid velocity. However, such effect diminishes and

even vanishes for relatively large particles due to the high particle inertia. The particles inertia dominates its trajectory and makes it not yield to the drag force.

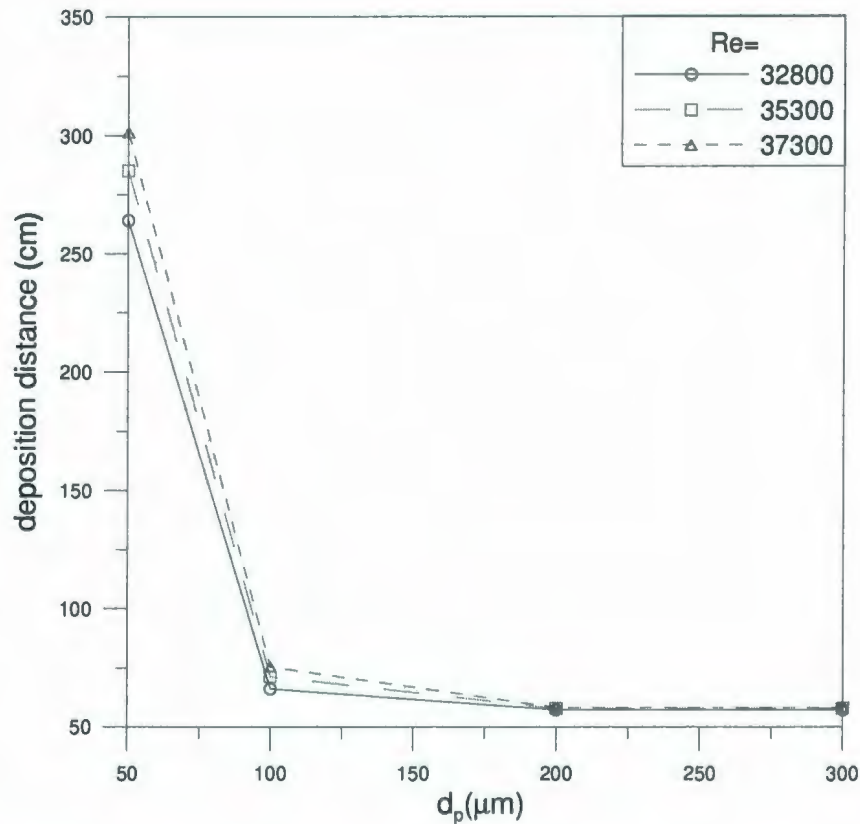


**Figure (8.9)** Influence of Reynolds number on particle deposition location

#### 8.4 Bouncing distance

The distance that the particle moves forward as a result of rebound is affected not only by the particle size but also by the pipe size and flow structure. A graph representing the influence of the pipe size on the rebound distance as a function of particle size can be used to demonstrate this effect. Figure (8.10) illustrates the variation of rebound distance with particle diameter as a function of particle size within a pipe. It can be seen that the bouncing distance reaches a

maximum as the size of the particle increases. This trend is identical for all pipe sizes; however, the vertex could shift to the left as the pipe becomes large.

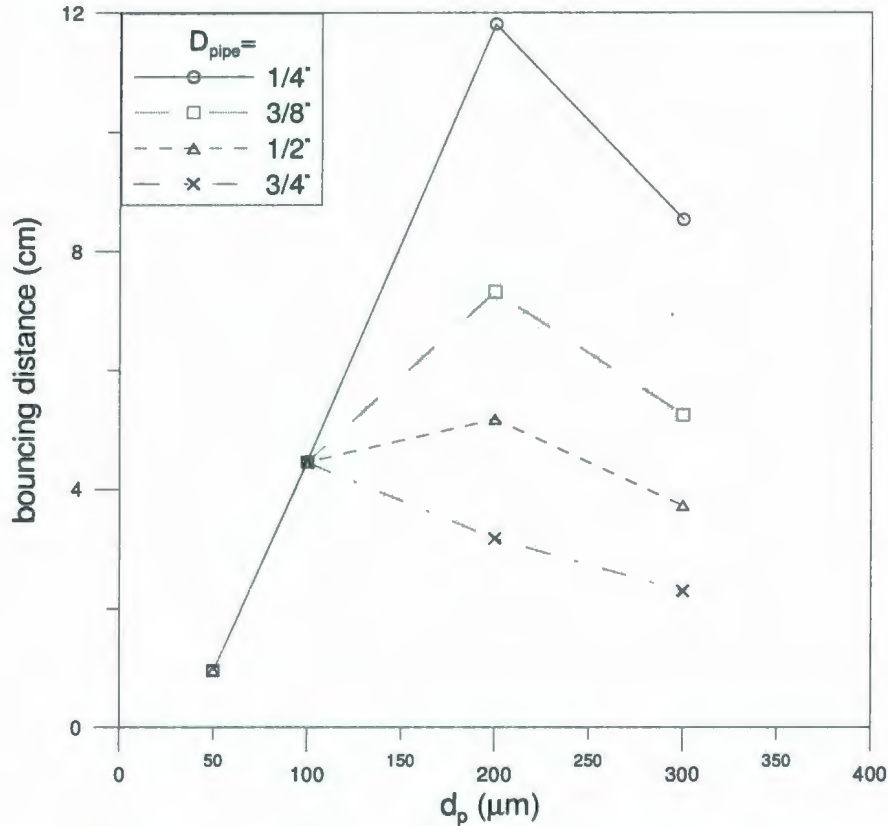


**Figure (8.10)** Distance traveled by ice particles due to bouncing as a function of particle diameter for different pipes

### 8.5 Experimental results and preliminary model validation

Several tests were conducted using four tubes and at different Reynolds numbers. The transparent tubes used for the tests were ~ 1.83m (6ft) in length and their diameters were varied from 1/4 to 3/4 inches. The tests for each tube were conducted using three different flowrates controlled by changing orifice inlet pressure through controlling the air pressure at the

compressor discharge. Position of the first droplets deposit on the wall was observed and the distance from the orifice to that position was measured.

Based on the procedure of the experiments described in Chapter 7 and appendix C, the temperature of the air at the exit of the orifice drops slightly below water freezing point. The temperature right after the orifice starts to increase rapidly and reaches almost the orifice inlet value within a short distance ( $\sim 2\text{cm}$ ). Theory and numerical analysis matched the observations. Both confirmed that the ice particles, if formed in the orifice, thawed out due to either the rapid increase in the pressure and temperature after the orifice or as a result of the heat transfer with the surrounding. The latter means that the ice particles maintained in the solid form during migration in the flow then melted after deposited on the tube wall. In the present analysis both situations are studied by including the bouncing effect for solid particles and ignoring such effect for water droplets.

During the tests the following parameters were recorded: exit air standard volume flow rate  $Q_{st}$ ; inlet  $P_I$  and  $T_I$ ; and system exit conditions  $P_{ex}$  and  $T_{ex}$ . The given data were reported in standard condition (101 325 Pa; 15 °C).

The measured data were compared with the model predictions to find out the level of agreement and to validate the accuracy of the simulations. The model presumed that various sizes of particles, ranging from the critical size ( $r_c = 11.5\text{ nm}$ ) to several hundred microns ( $\sim 200\text{ }\mu\text{m}$ ), are leaving the orifice. It is concluded from Figure (8.8) that particles larger than this range have no influence on the deposition distance. Based on the assumption, the model is designed to predict

the deposition distance of these sizes using the approach discussed earlier in Section 8.3. The typical calculations proposed in Appendix F demonstrate the procedure of the model prediction.

Figure (8.11) illustrates the distance from the orifice to the location of deposition as a function of pipe size when Reynolds number is  $32.8 \times 10^3$ . The figure shows a fair agreement between the experiment and the model prediction; see Table (8.3a). Both Tables (8.3 a) and (8.3b) indicate that the distance of the deposition increases with the pipe size. Poor agreement was found when the influence of Reynolds number was investigated as shown in Fig. (8.12). Experimental results and model predictions conclude that the deposition distance varies linearly with Reynolds number; however, the slope of the trend in the test data is significantly higher; see Table (8.3b).

**Table (8.3a)** Percent error of deposition distance observed in experimental tests and predicted by simulation for  $Re=32\ 800$  (Figure 8.11)

Pipe Diameter (cm)	Model prediction (cm)	Test result (cm)	% discrepancy
6.36	19.1	15	21.5
9.53	28.7	24	16.4
12.70	38.2	40	4.7
19.05	57.3	55	4.0

**Table (8.3b)** Percent error of deposition distance observed in experimental tests and predicted by simulation for 1/4" pipe (Figure 8.12)

Re	Model prediction (cm)	Test result (cm)	% discrepancy
32 800	19.12	15	21.5
35 300	19.3	20	3.5
37 300	19.44	24	19

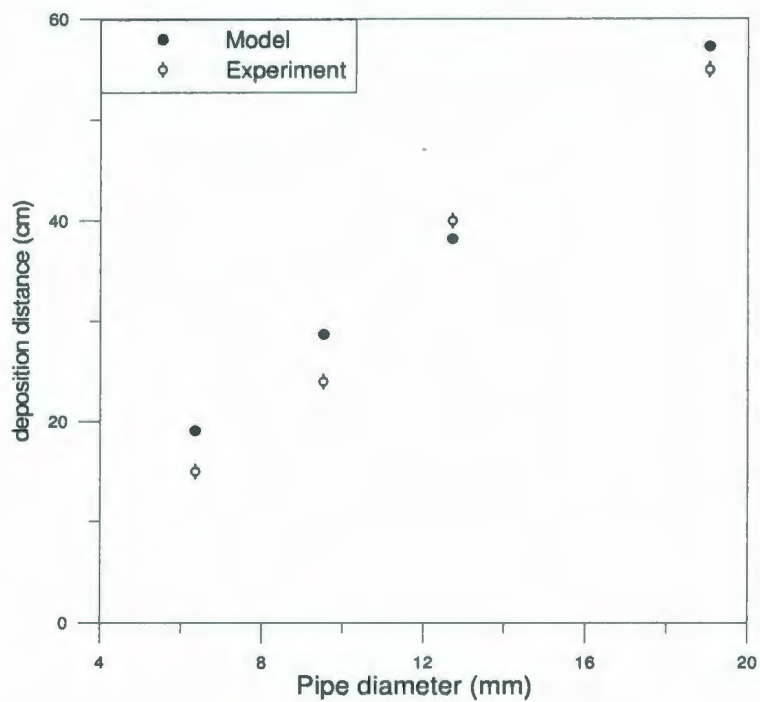


**Figure (8.11)** Deposition distance predicted by simulation and measured during tests as a function of pipe size

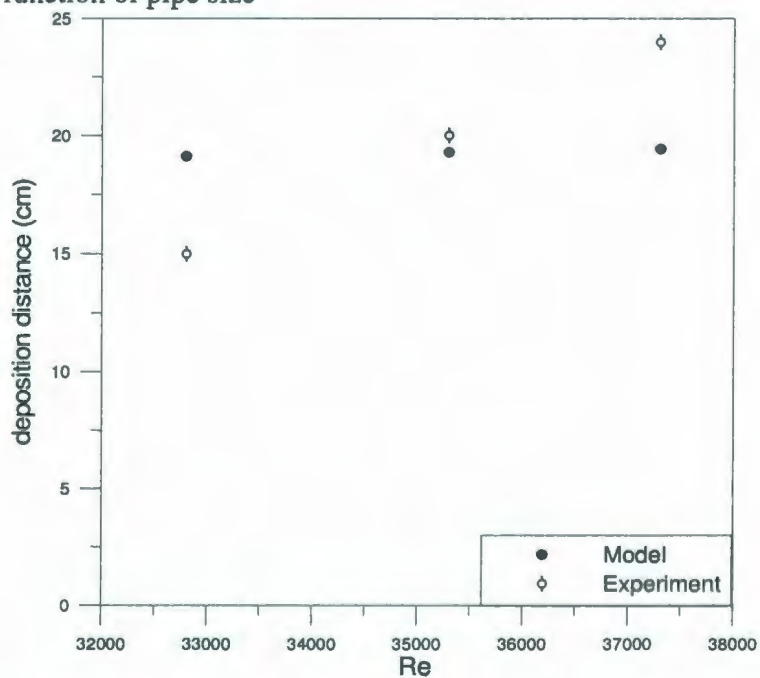


**Fig. (8.12)** Comparison of influence of Reynolds number predicted by proposed model and experimental data on deposition distance

Finally, comparison of the ice particles with water droplets is presented by studying the influence of the bouncing process. Figure (8.13) illustrates the deposition distance as a function of the pipe size with and without bouncing effect, i.e. assumption of particles remaining in the solid or liquid states, respectively. It could be concluded from the figure that the discrepancy of the deposition distance predicted by the simulation for the liquid droplets and solid particles with that observed in the tests is reasonable for all pipes. The percent errors of the droplet and ice with respect to the experimental results are listed in Table (8.4) and shows good agreement between the simulations prediction and the tests observation.

**Table (8.4)** Ice and water comparison of the deposition distance observed in the tests and predicted by the simulation for  $Re= 32\ 800$

$D_{\text{pipe}}$ (mm)	Test result (cm)	Liquid droplet (cm)	Ice particle (cm)	% error of droplet	% error of ice particle
6.35	25	19.12	27.66	23.5	10.64
9.525	30	28.7	33.95	4.33	13.17
12.7	40	38.2	41.93	4.5	4.8
19.05	55	57.3	59.6	4.2	8.4

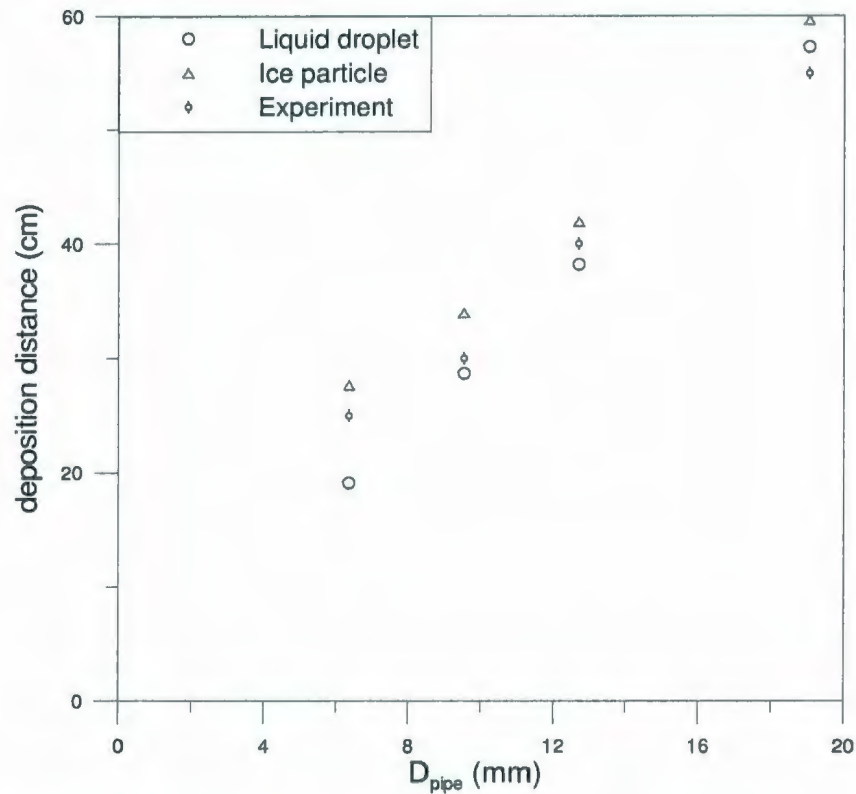


**Fig. (8.13)** Comparison of deposition distance predicted by simulation for different types of particles (assumption of particles remaining in ice or liquid forms when reaching wall) with experimental data as a function of the pipe size

### 8.6 Uncertainty analysis of saturated air experiments

There is a fact that uncertainties exist in virtually all computational, analytical, or experimental engineering endeavour. Fluid mechanics is among those that are heavily dependant on experimentation and the data uncertainty checks are needed since sometimes uncertainty completely changes the viewpoint of the results. Uncertainty of the data is defined as the band within which the experimenter is 95 percent confident that the true value lies (White, 2003). The purpose of this section is to manifest the uncertainty analyses, which was used in the planning of experimental facilities.

The fundamental concept of experimental uncertainty analysis is to compute the experimental results ( $r$ ) using a data-reduction equation and the values of  $J$  basic measurements:

$$r = r(X_1, X_2, \dots, X_J) \quad (8.5)$$

The uncertainty in the results is computed to the first order using a root-sum-square of the product of the uncertainties in the measured variables and the sensitivities of the result to changes in that variable:

$$U_r = \left[ \left( \frac{\partial r}{\partial X_1} U_{x_1} \right)^2 + \left( \frac{\partial r}{\partial X_2} U_{x_2} \right)^2 + \dots + \left( \frac{\partial r}{\partial X_J} U_{x_J} \right)^2 \right]^{1/2} \quad (8.6)$$

Where, the  $U_x$ 's are the uncertainties in each basic measurement and the partial derivatives are the sensitivity coefficients.

Since the target of the experiments that presented in this research is to predict the distance of the particle deposition from the orifice ( $S_d$ ), it is essential to consider this parameter as a dependant variable. The independent variables or the measured parameters were: flow temperature and pressure ( $T, P$ ), standard flowrate ( $Q_0$ ), pipe diameter ( $D$ ), and the standard temperature and pressure ( $T_0, P_0$ ).

Therefore, the uncertainty equations become:

$$S_d = S_d(Q_0, D, T, T_0, P, P_0) \quad (8.7)$$

$$U_{S_d} = \left[ \left( \frac{\partial S_d}{\partial Q_0} \delta Q_0 \right)^2 + \left( \frac{\partial S_d}{\partial D} \delta D \right)^2 + \left( \frac{\partial S_d}{\partial T} \delta T \right)^2 + \left( \frac{\partial S_d}{\partial T_0} \delta T_0 \right)^2 + \left( \frac{\partial S_d}{\partial P} \delta P \right)^2 + \left( \frac{\partial S_d}{\partial P_0} \delta P_0 \right)^2 \right]^{1/2} \quad (8.8)$$

The sensitivity of the flowmeter device used in the experiment is  $\pm 2\%$ , the tolerance error in the size of the pipe is  $\pm 1\%$ , the accuracy of temperature measurement is within  $\pm 1$  K, and that of the pressure measurement is  $\pm 13.79$  KPa ( $\pm 2$  PSI).

The measurement's errors influence the flow Reynolds number according to the following formula:

$$\text{Re} = \frac{U_g D}{\nu_g} = \frac{4Q}{\pi D \nu_g} \quad (8.9)$$

$$\text{Where, } Q = Q_0 \times \frac{P_0}{P} \times \frac{T}{T_0} \quad (8.10)$$

The actual flowrate is sensitive to the error of measurements in the standard flowrate, the system temperature and pressure, and the standard temperature and pressure. Besides, the viscosity of the fluid changes strongly with the temperature (White, 2003). All these parameters will disturb the magnitude of Reynolds number followed by the value of the deposition distance ( $S_d$ ).

The following equation, which represents the variation of kinematics viscosity with temperature for air, was used in the analysis:

$$\nu_g = -1.1555 \times 10^{-14} T^3 + 9.5728 \times 10^{-11} T^2 + 3.7604 \times 10^{-8} T - 3.4484 \times 10^{-6} \quad (8.11)$$

Where,  $T$  is temperature in K and  $\nu_g$  kinematics viscosity in  $\text{m}^2/\text{s}$ . The simulation model was run for data obtained from a typical test by keeping all the parameters but one constant and the results of the deposition distances were compared with the base case (exact values of all parameters) to find out the discrepancy in the deposition distances responding to the error in a certain parameter. Table (8.5) shows such response in the values of Reynolds number and deposition distance.

**Table (8.5)** Sensitivity analysis of parameters measured in experimental tests

Parameter	Change in the parameter	$ \Delta Re $	$ \Delta S_d $ (mm)
Flowrate ( $Q_0$ )	$\pm 2\%$	370.7	1.7
Diameter ( $D$ )	$\pm 1\%$	244.68	1.2
System Temperature ( $T$ )	$\pm 1\text{K}$	66.83	0.3
System Pressure ( $P$ )	$\pm 2\text{PSI}$	2081.09	10.3
Ambient Temperature ( $T_0$ )	$\pm 1\text{K}$	85.51	0.5
Ambient Pressure ( $P_0$ )	$\pm 2\text{PSI}$	3408.68	15.1

Using Eq. (8.8), the total uncertainty in the deposition distance would be:

$$U_{S_d} = 18.41\text{mm} = 1.841\text{ cm}$$

The measured deposition distance of this typical sample test was found to be 55 cm. Therefore, the percent error due to uncertainty is approximately  $\pm 3.3\%$ .

Similar procedure is established for all saturated air tests discussed earlier and the results of the total uncertainty in deposition distance for each tests is calculated using Eq. (8.8). Table (8.6) summarizes the uncertainty value for different pipe size and at various Reynolds number while table (8.7) shows the percent error in the deposition distance due to uncertainty.

**Table (8.6)** Uncertainty values for saturated air tests

$Re$	$U_{S_d}$ (mm)			
	Size (3/4")	Size (1/2")	Size (3/8")	Size (1/4")
32 800	18.41	12.32	9.22	6.14
35 300	18.7	12.44	9.33	6.25
37 300	18.61	12.52	9.42	6.36

**Table (8.7)** Percent of uncertainty error for saturated air tests

<i>Re</i>	% error			
	Size (3/4")	Size (1/2")	Size (3/8")	Size (1/4")
32 800	3.3	3.1	3.8	4.1
35 300	3.4	3	3.5	3.1
37 300	3.1	3	2.5	2.6

## B. Propane-Hydrate Tests

### 8.7 Experiment apparatus

The experience from the preliminary tests with air and water led to the revised design of the experimental set-up. Using the two separated cooling zones with capability for adjusting temperatures in the saturation and hydrate formation zones, the difficulties encountered in water-air tests could be prevented. In the new revised experimental set-up, the coil, the saturator, and the separator were located in the first zone (gas saturation zone, the small chamber). The orifice and the pipe, where the hydrate forms, were placed in the large chamber (hydrate formation zone). The system is presented in Fig. (7.3) of Chapter 7. Propane was used as the working fluid since the propane hydrate can form above water freezing temperature under relatively low pressures.

#### 8.7.1 Test procedure

A compressor was used to circulate the gas within the system. The gas loops were charged with propane and the compressor was started. The maximum pressure recorded in the transparent pipe was around 293 kPa abs (~42.5 psi). Using Fig. (8.14), the hydrate equilibrium temperature ( $t_{eq}$ ) relative to this pressure is ~3°C. The small chamber was adjusted to a temperature slightly higher

than  $t_{eq}$  (5, 6°C) to prevent any hydrate formation in saturation zone. The temperature in the large chamber (hydrate formation zone) was set to a temperature lower than  $t_{eq}$  (-1, -2°C) to induce a driving force large enough to stabilize the nucleation and particle growth stable.

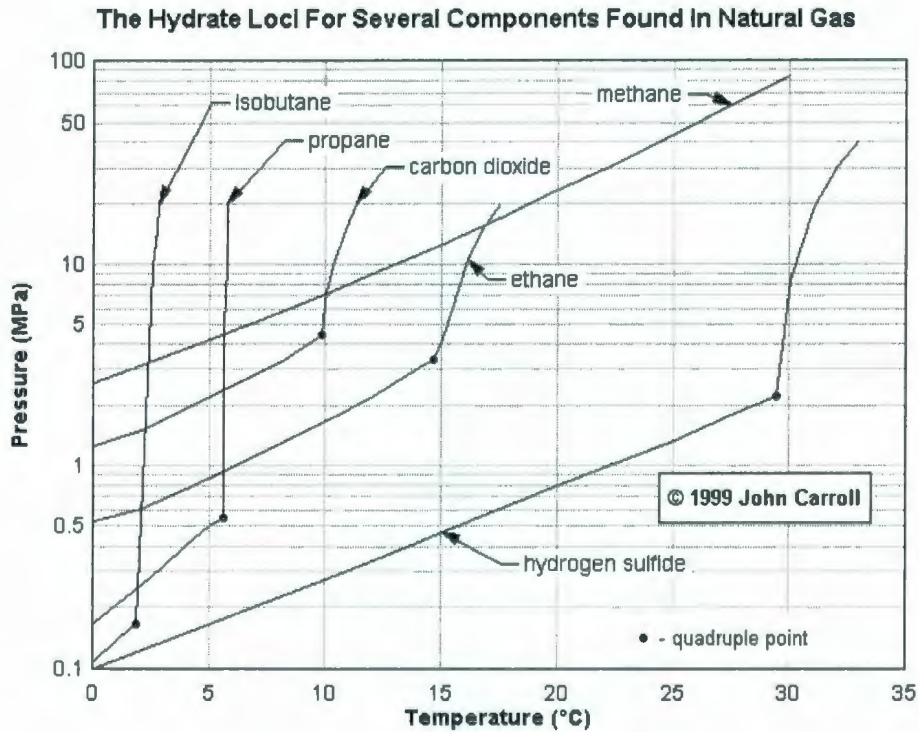


**Fig. (8.14)** Hydrate loci for several components found in natural gas (Carroll J.J., 2003)

The saturator was originally located before the cooling coil outside of the small chamber. However, the temperature of the gas heading to the saturator was observed to be excessively high making the gas oversaturated leading to excessive condensation in the saturation zone. The condensed water overloaded the filter separator and ended up as free liquid in the transparent tube in the hydrate formation zone. Since the purpose of this study was to investigate the hydrate formation in the absence of free water, it was decided to saturate the gas, under low temperature

of saturation zone, by moving the saturator to downstream of the coil inside the small chamber; see Figure (8.15).

The data shown in Table (8.8) were recorded during the tests. The flow rate was corrected using Eq. (C-1) in Appendix (C). Table (8.8) shows the recording data and the corrected flow rate for typical test using the 3/4" pipe. From the table, the following parameters were calculated:

Gas superficial velocity:  $U_g = 15.02$  m/s;

Gas density:  $\rho = 5.6$  kg/m<sup>3</sup>; and

Reynolds number:  $Re = 14\ 560$

**Table (8.8)** Data recorded from a typical propane test

	Suction	Discharge	Point 2	Point 3	Point 4
Temperature (°C)	3	63	60	8.0	5.5
Pressure (KPa)	82.74	455	413.7	193	193
Standard flowrate (m <sup>3</sup> /s)	$13 \times 10^{-3}$				
Corrected flowrate (m <sup>3</sup> /s)	$4.28 \times 10^{-3}$				

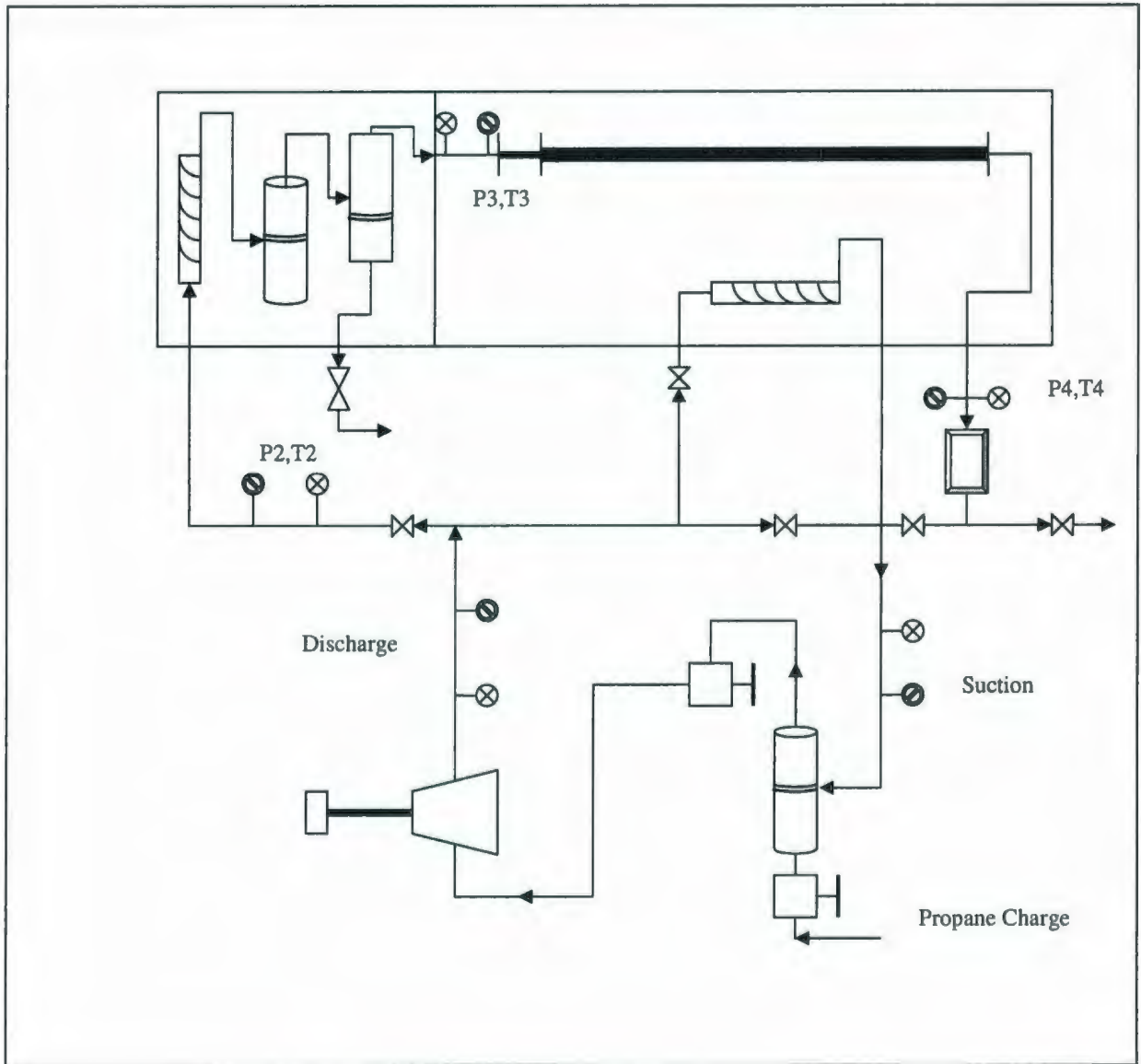


**Figure (8.15)** Location of measuring points in the system

These parameters along with the environmental temperature inside the large chamber were used as the boundary conditions in the simulation model to predict the deposition of the hydrate particles.

### **8.7.2 Observations**

As shown in Fig. (8.16), propane hydrate with different particle sizes was formed. As explained in the first case study, it was presumed that due to the particle-particle attachment (coalescence within the gas and on the tube wall), formation of various critical sizes, and different growth times, a range of particle sizes were formed.

After the completion of the test, the distance from the orifice to the location of the first observable particle was measured. Then the pipe was dismantled and abandoned for a while to assure there were no water droplets remaining in the pipe before doing the next test. This procedure was repeated three times for different flowrates to investigate the influence of the Reynolds number on the deposition distance.

### **8.8 CFD and simulation- results**

The system was simulated by means of the commercial CFD software (FLUENT) using the data of the conditions prevailing the experimental tests. Similar to the saturated air case, the parameters obtained from the FLUENT simulation were used to calculate the deposition distance based on the concept proposed in this study.

The geometry used in this study had the same dimensions as discussed in Fig. (8.1). For the propane case, a grid with 575 340 quadrilateral cells were created in the Gambit software.

The boundary conditions are listed in Table (8.9), which represents the data measured for typical test conditions.



**Figure (8.16)** Hydrate particles deposit on the pipe wall (magnification factor ~2.73)

**Table (8.9)** Boundary conditions for typical saturated propane simulations

	Parameters	Values	Units	Description
Inlet	Pressure	$1.95 \times 10^5$	Pa	gauge
	Total temperature	279	K	
Exit	Pressure	$1.93 \times 10^5$	Pa	gauge
	Total temperature	278	K	
Lateral Wall	temperature	272	K	Isothermal

## 8.9 Nucleation and Growth of Hydrate Particles

The data obtained from FLUENT was used to describe and estimate the process of nucleation and growth of the hydrate particles. It was shown in the analysis discussed in Chapter 4 that mass transfer and hydrate formation reaction kinetics are the dominant processes in the nucleation and growth of the hydrate particles. Parameters used for describing these processes are listed in Table (8.10).

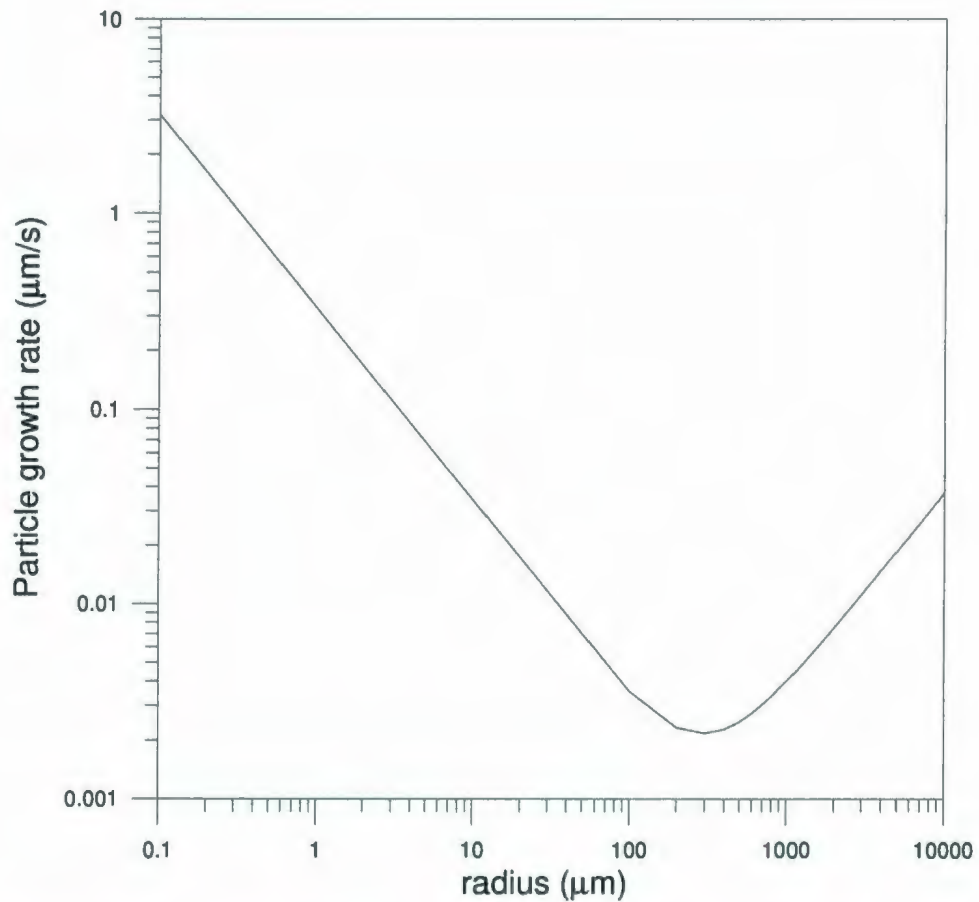
**Table (8.10)** Parameters used in calculating  $\beta_1$ ,  $\beta_2$  and critical radius for propane hydrate

Parameter	Value*
$n_v$	0.13
$Sh$	2.009
$D$	$3.1 \times 10^{-2}$ (cm <sup>2</sup> /s)
$y$	$2.143 \times 10^{-4}$
$y_{eq}$	$1.964 \times 10^{-4}$
$f$	$2.9 \times 10^5$ (Pa)
$f_{eq}$	$1.8 \times 10^5$ (Pa)
$\sigma$	0.022 (N/m)

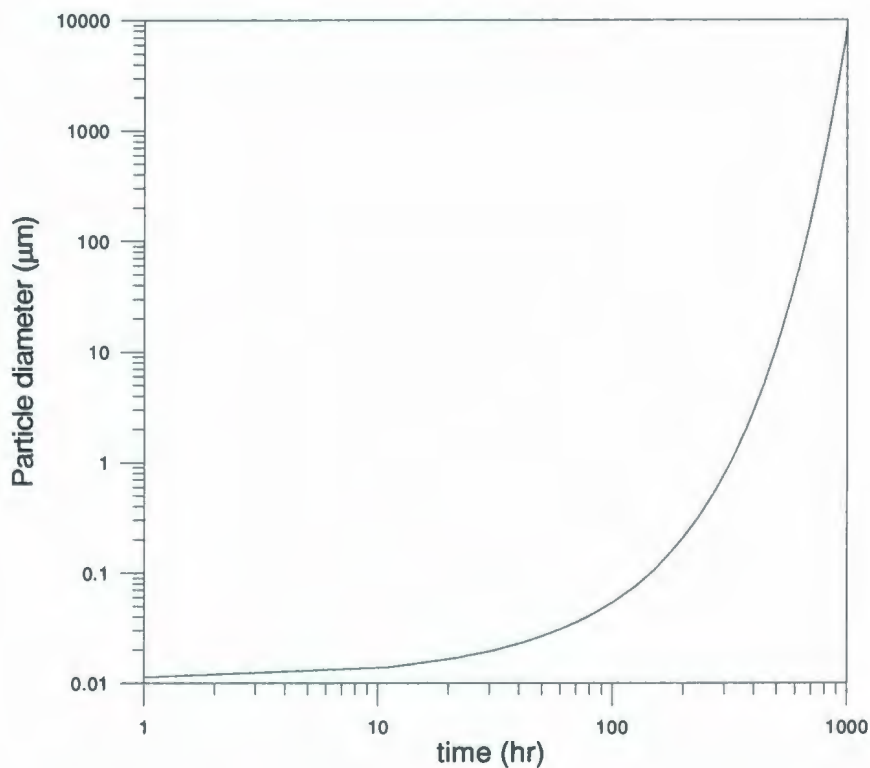
\* See Appendix E for typical calculations

Figure (8.17a) shows the growth rate of hydrate particles in micrometer scale as a function of size (diameter). Since mass transfer is the dominating factor of growth after the hydrate was just nucleated, the rate of growth will decrease as the size of hydrate grows. However, the reaction kinetics will start to be the controlling factor in the growth process as the particle size grows

further. Therefore there is a dip in the growth rate diagram. That means that the elapsed time required for hydrate particles to grow to several hundreds of microns is relatively long but the trend dramatically change as the particle size increase beyond 100 microns and a sharp change of particle diameter is observed; see Figure (8.17b).



**Figure (8. 17a)** Propane hydrate growth rate as a function of particle size



**Figure (8. 17b)** Propane hydrate diameter as a function of time

It is important to note here again that our simulation results are based on the basic assumption that the particles leaving the orifice have different sizes and the approach used to describe the deposition model in this research is based on this fundamental hypothesis.

Figure (8.18) illustrates the number of particles in dimensionless form using Eq. 4.31 as a function of dimensionless particle radius at time equal zero (nucleation time). The graph clearly indicates that there is a distribution of the particles different sizes when hydrate particles are formed; in particular particles with radii greater than the critical radius.

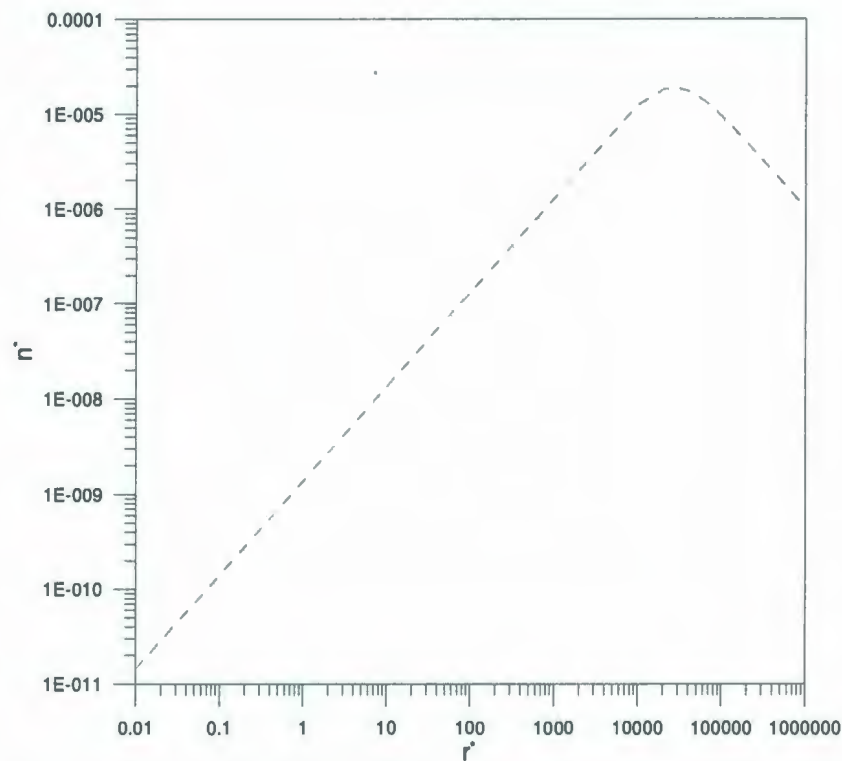


**Figure (8.18)** Propane hydrate particle distribution as a function of size

### 8.10 The deposition distance

The data of the measured deposition distance from the orifice exit to the first deposition spot were recorded with a measurement tape with millimetre precisions. The deposition measurement data were compared with the results obtained from the simulation. Table (8.11) illustrates such comparison of deposition distances with those predicted from the model for three tests performed for a 3/4" pipe under the conditions where Reynolds numbers were 14 500, 8 400, and 4 300, respectively. Figure (8.19) shows the discrepancy of the deposition distance predicted by the theory and the experiment. The model predictions were in a very good agreement with the experiment data. The discrepancy between the model predictions with experimental readings at the low and high Reynolds numbers are due to measurements inaccuracies.

**Table (8.11)** Measured deposition distance and model predictions for various  $Re$

<i>Test #</i>	<i>Re</i>	<i>S<sub>d</sub> theory (cm)</i>	<i>S<sub>d</sub> measured (cm)</i>	<i>Deviation %</i>
1	14 500	89.1	90.5	1.6
2	8 400	82.3	83.7	1.7
3	4 300	74.6	73.5	1.5

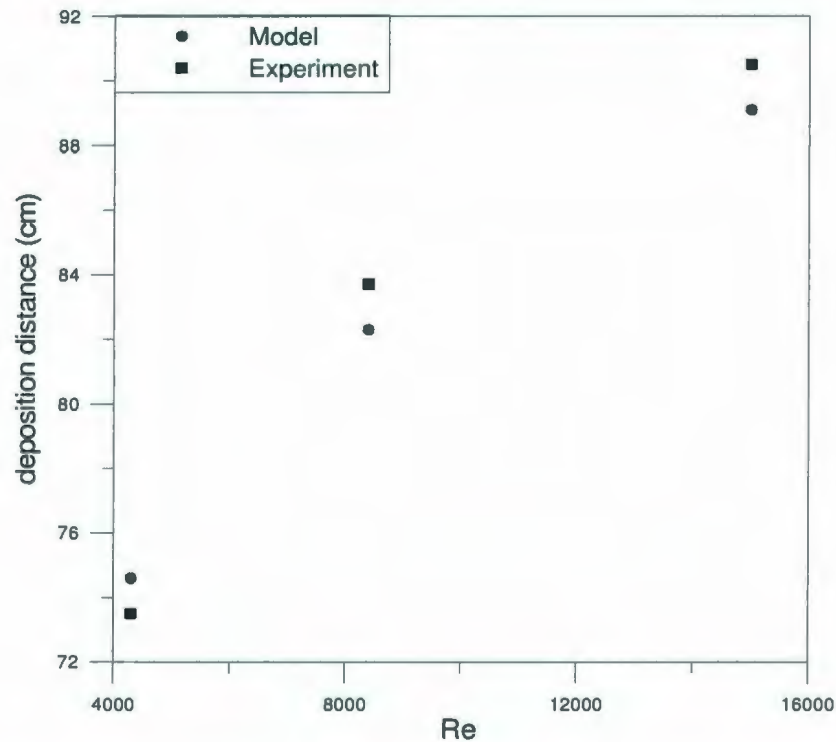


**Figure (8.19)** Comparison of hydrate deposition distance predicted by proposed model and experimental results as a function of Reynolds number

### 8.11 Uncertainty Analysis

As discussed in the first case study, the sensitivity of the flowmeter device used in the experiment is  $\pm 2\%$ , the tolerance error in the size of the pipe is  $\pm 1\%$ , the accuracy of temperature measurement is within  $\pm 1$  K, and that of the pressure measurement is  $\pm 13.80$  kPa ( $\pm 2$  PSI). Following the procedure elaborated for the previous case in this Chapter and using Eq. 8.8, the uncertainty in the deposition distance and the precision of each parameter are calculated. Tables

(8.12) to (8.14) demonstrate the discrepancy in the deposition distance for each measuring parameter and the total uncertainty error for each test.

Table (8.12) Uncertainty in parameters and total uncertainty for test no. (1)

Parameter	Change in the parameter	$ \Delta Re $	$ \Delta S_d $ (mm)
Flowrate ( $Q_0$ )	$\pm 2\%$	306	3
Diameter ( $D$ )	$\pm 1\%$	151	2
System Temperature ( $T$ )	$\pm 1\text{K}$	55	1.3
System Pressure ( $P$ )	$\pm 13.8\text{kPa}$	53	1.3
Ambient Temperature ( $T_0$ )	$\pm 1\text{K}$	720	6.6
Ambient Pressure ( $P_0$ )	$\pm 13.8\text{kPa}$	2109	19
$U_{S_d}$			20.5

Table (8.13) Uncertainty in parameters and total uncertainty for test no. (2)

Parameter	Change in the parameter	$ \Delta Re $	$ \Delta S_d $ (mm)
Flowrate ( $Q_0$ )	$\pm 2\%$	170	2
Diameter ( $D$ )	$\pm 1\%$	84	1
System Temperature ( $T$ )	$\pm 1\text{K}$	30	0.5
System Pressure ( $P$ )	$\pm 13.8\text{kPa}$	30	0.5
Ambient Temperature ( $T_0$ )	$\pm 1\text{K}$	400	5.7
Ambient Pressure ( $P_0$ )	$\pm 13.8\text{kPa}$	1170	17.3
$U_{S_d}$			18.36

Table (8.14) Uncertainty in parameters and total uncertainty for test no. (3)

Parameter	Change in the parameter	$ \Delta Re $	$ \Delta S_d $ (mm)
Flowrate ( $Q_0$ )	$\pm 2\%$	82	1.9
Diameter ( $D$ )	$\pm 1\%$	41	1.4
System Temperature ( $T$ )	$\pm 1\text{K}$	15	0.2
System Pressure ( $P$ )	$\pm 13.8\text{kPa}$	14	0.2
Ambient Temperature ( $T_0$ )	$\pm 1\text{K}$	194	5.1
Ambient Pressure ( $P_0$ )	$\pm 13.8\text{kPa}$	570	16
$U_{S_d}$			16.96

## Chapter 9

### Conclusions and recommendations

The present research examined the growth and deposition of hydrate formed in a gas/vapour mixture. A circular pipe with restriction (orifice in this study) is simulated using new analytical model of hydrate growth and distribution processes.

The model, which satisfies the law of mass action, described the development of hydrate formation and growth through the contribution of two processes, the mass transfer and the reaction kinetics. The former occurs due to the drop in temperature below the equilibrium temperature while the latter is the result of the fugacity difference.

A novel approach to describe the particle traveling and deposition is introduced. The concept of the particle deposition velocity is introduced to help to predict the trajectory of the particle motion in the turbulent region. While the literature reports concerning the hydrate migration and deposition have ignored the wall effect, the model presented in this research proposes a new approach to track the particle motion merged in the sublayer region using the forces acting on the particle. For particles with sizes larger than the sublayer thickness, the model introduces the influence of the bouncing concept to explain the near wall effects.

The main conclusions of the research can be summarized as follows:

1. Analysis of the proposed model showed that the rate of particle growth is inversely proportional to the particle size in the process of mass transfer and linearly related to the process of reaction kinetics.

2. The continuum equations should be corrected when the motion of submicron particles is addressed. Since very tiny particles behave as fluid particles, Brownian effect is taken into account by including the slip correction factor in the continuum equations.
3. The deposition of particles in the turbulent region is mainly dominated by the diffusion process for submicron sizes and by inertia for relatively large sizes. The deposition velocity and collection efficiency follow a V-shape trend in that their values decrease as the particle size increases in the diffusion-controlled regime and increase as the size of particle increases in the inertia-controlled region. The particle size for distinction between the two motions is found to be  $\sim 1 \mu\text{m}$ .
4. The minimum numbers of particles that deposit and reach the boundary layer are those that have sizes of about  $1 \mu\text{m}$ .
5. The very tiny particles tend to deposit whereas the relatively larger particles are probably more susceptible to be entrained from the boundary layer near the wall.
6. The study showed that the distance of deposition decreases as the particle size increases. However, the analysis has introduced a certain size of particle in which further particle growth has no effect on the distance of deposition. Such size was called "deposition critical size".
7. Small particles are influenced by the main fluid velocity but the effect diminishes for relatively large particles as a result of the high particle inertia.
8. The experimental tests are in good agreement with the model predictions in that the deposition distance is linearly proportional to the Reynolds number.

9. Formation of hydrate particles are observed to be poly-dispersed since different sizes of particles are formed. This observation is consistent with the analytical correlation derived based on the law of mass action.
10. The deposition distance is found to be linearly proportional to the Reynolds number and pipe size.

### **Recommendations for future works:**

1. The hydrate formation reaction kinetics process was assumed to be independent on the particle's surface area.

i.e.  $\frac{dr_p}{dt} = \varphi(r_p)$

However, the more precise relation should be  $\frac{dr_p}{dt} = \varphi(r_p^3)$  since as the particle grows the surface area also affects the kinetics of the gas/vapour reaction and the growth rate.

2. The proposed model has ignored the influences of the electrical dipole force, thermophoresis force and coagulation process when the force balance concept is addressed. Therefore it is recommended to consider these forces in the future research.
3. The model ignored the effect of real gas conditions at high pressure conditions and fugacities were simply assumed to be equal to partial pressure of the desired component in the gas mixture. Equation of states should be used to improve the accuracy of the model for high pressure predictions.
4. Using accurate means in the experiment such as high speed camera to observe and follow the particle trajectory will enhance the accuracy of the prediction in terms of particle

growth and distribution, particle entrainment and deposition, and the phenomena of bouncing.

5. Study the sensitivity analysis for other factors that influence the deposition of hydrate; these factor include temperature (temperature of the saturator and the tube), pressure, gas structure, and the concentration in the gas mixture.
6. The model is believed to be comprehensive enough to be employed in addressing deposition of particles of other fields such as respiratory system, fouling in heat exchanger and deposition in combustion chamber.

## REFERENCES

Abraham F.F., "Homogeneous Nucleation Theory", New York: Academic Press Inc., 1974.

Aldaco R., Garea A., Irabien A., "Particle Growth Kinetics of Calcium Fluoride in a Fluidized Bed Reactor", *Chemical Engineering Science*, 62, 2958 – 2966, 2007.

Allen M.D., and Raabe O.G., "Re-Evaluation of Millikan's Oil Drop Data for Motion of Small Particles in Air", *Journal of Aerosol Science*, 6, 537-547, 1982.

Allen M.D., and Raabe O.G., "Slip Correction Measurements of Spherical Solid Aerosol Particles in an Improved Millikan Apparatus", *Aerosol Science Technology*, 4, 269-286, 1985.

Amiri A.E., Hannani S.K., Mashayek F., "large-Eddy Simulation of Heavy-Particle Transport in Turbulent Channel Flow", *Numerical Heat Transfer Part-B*, 50, 285-313, 2006.

Anandarajah A., and Chen J., "Single Correction Function for Retarded van der Waals Attraction." *J Colloid Interface Sci*, 176(2), 293 -300, 1995.

Athanasopoulos I., Makrakis G., Rodrigues J., "Free Boundary Problems", CHAPMAN & HALL/CRC, 1999.

Austvik T., Hustvedt E., Gjertsen L.H., Urdahl O., "Formation and Removal of Hydrate Plugs, Field Trial at Tommeliten", Proc. Gas Processors Association Conference, San Antonio, Texas, March 1997.

Ballard A., and Sloan E.D., "The Next Generation of Hydrate Prediction: An Overview", Proceeding to 4<sup>th</sup> International Conference Gas Hydrates, 2002.

Barkan E.S., and Sheinin D.A., "A General Technique for the Calculation of Formation Conditions of Natural Gas Hydrates", Fluid Phase Equilibria, 86, 111-136, 1993.

Barrer R.M., and Ruzicka D.J., "Non-Stoichiometric Clathrate Compounds of Water", Trans. Faraday Soc., 58, 2239-2271, 1962.

Barrer R.M., and Edge A.V., "Gas Hydrate Containing Argon, Krypton, and Xenon: Kinetics and Energetics of Formation and Equilibria", Proceedings R. Soc. London, A300, 1-24, 1967.

Bassin E.C., "Study of Nuclei Distribution and Vortex Diffusion Influence on Nuclei Capture by a Tip Vortex and Nuclei Capture Noise", Int. Symposium on Cavitations and Multiphase Flow Noise, 45, 53-58, 1986.

Benedict M., Webb G.B., Rubin L.C., "An Empirical Equation for Thermodynamic Properties of Light Hydrocarbons and Their Mixtures", Chem. Eng. Prog. 47(8), 419, 1951.

Berner D., "Marine Transport of Natural Gas in Hydrate Form", Int. Offshore and Polar Engineering Conference, 636-643, 1992.

Bilyushov V.M., Bondarev E.A., Maron V.I., "Hydrate Formation Process with Consideration of Heat and Mass Exchange", 55(2), 870-874, 1988.

Bird R.B., Stewart W.E., Lightfoot E.N., "Transport Phenomena", John Wiley and Sons Inc, 2<sup>nd</sup> Edition, 2002.

Bishnoi P.R., and Dholabhai P.D., "Equilibrium Conditions for Hydrate Formation for a Ternary Mixture of Methane, Propane and Carbon Dioxide, and a Natural Gas Mixture in the Presence of Electrolytes and Methanol", Fluid Phase Equilibria, 158-160, 821-827, 1999.

Bollavaram P., "Hydrate Plug Dissociation in Pipelines by Pressure reduction: Experiment and Modeling", PhD Thesis, Center for Hydrate Research, Colorado School of Mines, 2002.

Bonnefoy O., Gruy F., Herri J.M., "Van der Waals Interactions in Systems Involving Gas Hydrate", Fluid Phase Equilibria, 231, 1767-187, 2005.

Borthne G., berge L., Austvik R., Gjertsen L., "Gas Flow Cooling Effect in Hydrate Plug Experiments", Proceeding 2<sup>nd</sup> International Conference Natural Gas Hydrates, Toulouse, France, 381, 2-6 June 1996.

Brenneke C.E., "Fundamentals of Multiphase Flow", Cambridge University press, 1<sup>st</sup> edn. 2005.

Brewer P.G., "Gas Hydrates and Global Climate Change", Ann NY Acad Sci, 912, 195-199, 2000.

Brill J.P., and Mukherjee H. "Multiphase Flow in Wells", Monograph volume 17, SPE Henry L. Doherty Series, Society of Petroleum Engineers Inc., Richardson, Texas, 1999.

British Petroleum annual energy reports, Statistical Review of World Energy, 2006.

Brock J.R., "New Aspects of Aerosol Growth Processes", Aerosol Science Technology, 2, 109-120, 1983.

Browne L.W.B. "Deposition of particles on rough surfaces during turbulent gas-flow in a pipe", Atmospheric Environment, 8, 801-816, 1973.

Buanes T., Kvamme B., Svandal A., "Computer Simulation of CO<sub>2</sub> Hydrate Growth", J. of Crystal Growth, 287, 491-494, 2006.

Buffett B.A., "Clathrate Hydrates", Earth Planet Science, 28, 477-507, 2000.

Buften S.A., "Ultra Deepwater will Require Less Conservative Flow Assurance Approaches", Oil Gas J. 101(18), 66-77, 2003.

Burry D., and Bergeles G., "Dispersion of Particles in Anisotropic Turbulent Flows", *Int. J. Multiphase Flow*, 29, 651–664, 1993.

Callanan J.E. and Sloan E.D., "Calorimetric Studies of Clathrate Hydrate", *Int. Gas Research Conference*, 1012-1021, 1983.

Cameron I., Handa Y.P., Baker T.H., "Compressive Strength and Creep Behaviour of Hydrate-Consolidated Sand", *Can. Geotech. J.*, 27, 255, 1990.

Campbell J.M., "Gas Conditioning and Processing, 3<sup>rd</sup> Ed. Campbell Petroleum Series", Norman, OK, 1992.

Carroll J.J., "Natural Gas Hydrate: A Guide for Engineers", Gulf Professional Publication, Amsterdam, the Netherlands, 2003.

Chatti I., Delahaye A., Fournaison L., Petitet J.P., "Benefits and Drawback of Clathrate Hydrates: a Review of their Areas of Interest", *Energy Conservation and Management*, 46, 1333-1343, 2005.

Chein R., Liao W., "Analysis of Particle-wall Interaction during Particle Free Fall", *Journal of Colloid and Interface Science*, 288, 104-113, 2005.

Chen J., and Anandarajah A., "Van der Waals Attraction between Spherical Particles", *Journal of Colloid and Interface Science*, 180, 519-523, 1996.

Chen Q., and Ahmadi G., "Deposition of particles in a turbulent pipe flow", *Journal of Aerosol Science*, 28, 789-796, 1997.

Chenoweth J.M., "Turbulent Two-Phase Flow", *Petroleum Refiner*, 34(10), 151-155, 1955.

Cherukat P., McLaughlin J.B., "The Inertial Lift on a Rigid Sphere in a Linear Shear Flow Field Near a Flat Wall", *Journal of Fluid Mechanics*, 263, 1-18, 1994.

Churchill S.W., "Friction Factor Equation Spans All Fluid Regimes", *Chemical Engineering*, 84(24), 91-92, 1977.

Clarke M., and Bishnoi P.R., "Determination of The Intrinsic Rate Constant of Ethane Gas Hydrate Decomposition", *Chemical Engineering Science*, 55, 4869-4883, 2000.

Clarke M., and Bishnoi P.R., "Determination of Tthe Activation Energy and Intrinsic Rate Constant of Methane Gas Hydrate Decomposition", *The Canadian Journal of Chemical Engineering*, 79, 143-147, 2001.

Claussen W.F., "Suggested Structures of Water in Inert Gas Hydrates", *J. Chem. Phys.*, 19, 259-266, 1951.

Cleaver J.W., and Yates B., "A sublayer model for the deposition of particles from a turbulent flow", Chem.Engng Sci. 30, 983-992, 1975.

Collett T.S., and Kuuskraa V.A., "Hydrates Contain Vast Store of World Gas Resources", Oil Gas Journal, 90-95, 11(May), 1998.

Crowe C.T., "Multiphase Flow Handbook", Taylor & Francis Group, 2006.

Crowe C.T., Sommerfeld M., Tsuji Y., "Multiphase Flow with Droplets and Particles", CRC Press, FL, 1998.

Dagan R., Elias E., Wacholder E., Olek S., "Two-Fluid Model for Critical Flashing Flows in Pipes", Int. Journal of Multiphase Flow, 19(1), 15-25, 1993.

Dahneke B., "The Capture of Aerosol Particles by Surfaces", Journal of Colloid Interface Science, 37, 342-353, 1971.

Davalath J., "Methods to Clear Blocked Flow-lines", Mentor Subsea, DeepStar IIA CTR A208-1, 157 pages and appendix, January 1996.

Davidson D.W., El-Defrawy M.K., Fuglem M.O., Judge A.S., "Natural Gas Hydrates in Northern Canada", In: 3<sup>rd</sup> International Conference on Permafrost, 938-943, 1978.

Davidson D.W., Garg S.K., Gough S.R., Handa Y.P., "Some Structural and Thermodynamic Studies of Clathrate Hydrates", *Journal Inclusion Phenomenon*, 2, 231-238, 1984.

Davidson D.W., Handa Y.P., Ripmeester J.A., "Xenon-129 NMR and Thermodynamic Parameters of Xenon Hydrate", *J. Phys. Chem.*, 90, 6549-6552, 1986.

Davies C.N., "Aerosol Science", Academic Press, London, 1966.

Davis R.H., Serayssol J.M., Hinch E.J., "The Elasto-hydrodynamic Collision of Two Spheres", *Journal of Fluid Mechanics*, 163, 479, 1986.

Denbigh K., "The Principles of Chemical Equilibrium", Cambridge University Press. 3rd. edn., 119, 1971.

Denney D., "Enhanced Hydrate Inhibition in an Alberta Gas Field", *Natural Gas Technology*, 74-75, April 2005.

Den Ouden C.J., and Thompson R.W., "Analysis of The Formation of Mono-Disperse Populations by Homogenous Nucleation", *Journal of Colloid Interface Science*, 143(77), 1991.

Derjaguin B.V., Landau L., "Theory of the stability of strongly charged lyophobic sols and of the adhesion of strongly charged particles in solutions of electrolytes", *Acta Physicochim*, 14, 633-662, 1941.

Dholabhai P.D., Kalogerakis N.E., Bishnoi P.R., "Kinetics of Methane Hydrate Formation in Aqueous Electrolyte Solution", *Canadian Journal of Chemistry Engineering*, 71, 68-74, 1993.

Dholabhai P.D., Parent J.S., Bishnoi P.R., "Equilibrium Conditions for Hydrate Formation from binary Mixtures of Methane and Carbon Dioxide in the Presence of Electrolytes, Methanol and Ethylene Glycol", *Fluid Phase Equilibria*, 141, 235-246, 1997.

Duckler A.E., Fabre J.A., McQuillen J. B., Vernon R., "Gas-Liquid Flow at Microgravity Conditions: Flow Pattern and Their Transitions", *Int. Journal of Multiphase Flow*, 14, 389-400, 1988.

Eligibaly A., Elkamel A., "Optimal Hydrate Inhibition Policies with the Aid of Neural Networks", *Energy Fuels*, 13, 105-113, 1999.

Ellenbecker M., Leith D., Price J., "Impaction and Particle Bounce at High Stokes Number", *Journal of Air Pol. Control Assoc.*, 30, 1224-1227, 1980.

Englezos P., and Bishnoi P.R., "Prediction of Gas Hydrate Formation Conditions in Aqueous Electrolyte Solutions", *AIChE Journal*, 34(10), 1718-1721, 1988.

- Englezos P., "Clathrate Hydrates", *Industrial Engineering Chemistry Res.*, 32, 1251-1274, 1993.
- Englezos P., Kalogerakis N.E., Dholabhai P.D., Bishnoi P.R., "Kinetics of Formation of Methane and Ethane Gas Hydrates", *Chem, Eng. Science*, 42(11), 2647-2658, 1987a.
- Englezos P., Kalogerakis, N.E., Dholabhai, P.D., Bishnoi, P.R., "Kinetics of Gas Hydrates Formation from Mixtures of Methane and Ethane", *Chem, Eng. Science*, 42(11), 2659-2666, 1987b.
- Englezos P., and Bishnoi P.R., "Gibbs Free Energy Analysis for the Supersaturation Limits of Methane in Liquid Water and the Hydrate-Gas-Liquid Water Phase Behaviours", *Fluid Phase Equilibria*, 42, 129-140, 1988.
- Ershov E.D., and Yakushev V.S., "Experimental Research on Gas Hydrate Decomposition in Frozen Rocks", *Cold Regions Science and Technology*, 20, 147-156, 1992.
- Fan F-G., and Ahmadi G., "A sublayer model for turbulent deposition of particles in vertical ducts with smooth and rough surfaces", *Journal of Aerosol Science*, 24, 45-64, 1993.
- Fan F-G., and Ahmadi G., "On the sublayer model for turbulent deposition of aerosol particles in the presence of gravity and electric fields", *Aerosol Science Technology*, 21, 49-71, 1994.

Fatykhov M.A., and Bagautdinov N.Y., "Experimental Investigation of Decomposition of Gas Hydrate in a Pipe under The Impact of a Microwave Electromagnetic Field", *High Temperature*, 43 (4), 614-619, 2005.

Felton K., and Loth E., "Spherical Bubble Motion in a Turbulent Boundary Layer", *Phys. Fluids*, 13, 2564-2577, 2001.

Fichman M., Gutfinger C., Pnueli D., "A model for turbulent deposition of aerosols", *Journal of Aerosol Science*, 19, 123-136, 1988.

Fluent User's Manual, Fluent Inc., 2002.

Fournaison L., Delahaye A., Chatti I., Petitet J.P., "CO<sub>2</sub> Hydrates in Refrigeration Processes" *Ind. Eng. Chem. Res.*, 43(20), 6521 -6526, 2004.

Freer E.M., Selim M.S., Sloan E.D., "Methane Hydrate Film Growth Kinetics", *Fluid Phase Equilibria*, 185, 65-75, 2001.

Friedlander S.K., and Johnstone H.F., "Deposition of Suspended Particles from Turbulent Gas Streams", *Industrial Engineering Chemistry*, 49, 1151, 1957.

Fuchs N.A., "The Mechanics of Aerosol", Pergamon, Oxford, 1964.

Gidaspow D., "Multiphase Flow and Fluidization", Academic Press Inc., 1994.

Glasby G.P., "Potential Impact of Climate of the Exploitation of Methane Hydrate Deposits Offshore", *Mar Petrol Geol*, 20, 163-175, 2003.

Glew D.N., and Hagget M.L., "Kinetics of Formation of Ethylene Oxide Hydrate, Part I. Experimental Method and Congruent Solutions", *Can. J. Chem.*, 46, 3857-3865, 1968.

Glew D.N., and Hagget M.L., "Kinetics of Formation of Ethylene Oxide Hydrate, Part II. Incongruent Solutions and Discussion", *Can. J. Chem.*, 46, 3867-3877, 1968.

Gondret P., Lance M., Petit L., "Bouncing Motion of Spherical Particles in Fluids", *Physics of Fluids*, 14(2), 643-652, 2002.

GPSA Engineering Data Book, 11<sup>th</sup> Ed. Gas Processors Suppliers Association, Tulsa, OK, 1998.

Graauw J.D., and Rutten J.J., "The Mechanism and the Rate of Hydrate Formation", *Proceeding Int. Symposium Fresh Water Sea*, 103-116, 1970.

Granasy L., Pusztai T., Toth G., Jurek Z., Conti M., Kvamme B., "Phase Field Theory of Crystal Nucleation in Hard Sphere Liquid", *Journal of Chemical Physics*, 119(19), 10376-10382, 2003.

Gudmundsson J., and Borrehaug A., "Frozen Hydrate for Transport of Natural Gas", in 2<sup>nd</sup> International Conference on Natural gas Hydrates, 415-422, 1996.

Guggenheim E.A., "Thermodynamics", North-Holland, Amsterdam, 1957.

Hammersmidt E.G., "Formation of Gas Hydrates in Natural Gas Transmission Lines", Ind. Eng. Chem, 26(8), 851-855, 1934.

Hall D., "Measurements of the Mean Force on a Particle near a Boundary in Turbulent Flow", Journal of Fluid Mechanics 187, 451-466, 1988.

Handa Y.P., and Tse J.S., "Thermodynamic Properties of Empty Lattices of Structure I and Structure II Clathrate Hydrates", Journal of Physics and Chemistry, 90, 5917-5921, 1986.

Hatton G.J., Barajas A.M., Kuhl C.A., "Hydrate Plug Decomposition Test Program", Final Report, SwRI Project 04-8217, Oct. 1997.

Herri J., Gruy F., Cournil M., "Methane Hydrate Crystallization Mechanism from In-Situ Particle Sizing", AIChE Journal, 45(3), 590-602, 1999.

Hideyuki T., Takehito K., Yamato O., Ryo O., Kenji Y., Yasuhiko M.H., "Thermodynamic Simulations of Isobaric Hydrate-Forming Operations: Formulation of Computational Scheme

and Its Application to Hydrate Formation from a Methane + Ethane + Propane Mixture”, *Energy and Fuels*, 19, 1587-1597, 2005.

Hidy G.M., “Aerosols, an Industrial and Environmental Science”, Academic Press, New York, 1984.

Hinds W.C., “Aerosol Technology: Properties, Behaviour, and Measurement of Airborne Particles”, 2<sup>nd</sup> Edition, Wiley, New York, 1999.

Hinze J.O., “Turbulence”, New York: McGraw-Hill, 2<sup>nd</sup> Edition, 1975.

Holder G.D., and Enick R.M., “Solid Deposition in Hydrocarbon System-Kinetics of Waxes, Asphaltenes and Diamondoids”, Final Report, Gas Research Institute, GRI, 1995.

Holder G.D., Zetts S.P., Pradhan N., “Phase Behaviour in Systems Containing Clathrate Hydrates: A Review”, *Reviews in Chemical Engineering*, 5(1-4), 1-70, 1988.

Holder G.D., and Manganiello D.J., “Hydrate dissociation pressure minima in multicomponent systems”, *Chemical Engineering Science*, 37(1), 9-16, 1982.

Hwang M.J., Wright D.A., Kapur A., Holder G.D., “An Experimental Study of Crystallization and Crystal Growth of Methane Hydrates from Melting Ice”, *J. Inclusion Phenomena. Mol. Recognition Chem.*, 8, 103-116, 1990.

Ilori T.A., "Turbulent «deposition of aerosol particles inside pipes", PhD. thesis, University of Minnesota, 1971.

Imen C., Delaheye A., Fournaison L., and Petitet J.P., "Benefits and drawbacks of clathrate hydrates: a review of their areas of interest", *Energy Conversion and Management*, v 46, n 9-10, June, 2005, p 1333-1343.

Israelachvili J., "Intermolecular and Surface Forces", Academic Press, London, UK, 1992.

Jacobsen R.T., and Stewart R.B., "Thermodynamic Properties of Nitrogen Including Liquid and Vapor Phase From 63K to 2000K With Pressure to 10000 bar", *Phys. Chem. Ref. Data*, 2, 757-922, 1973.

Jadhawar P.S., "Inhibition Methods: Gas Hydrate Problems in Pipelines", *Chemical Engineering World*, 38 (6), 65-68, 2003.

Jager M.D., Peters C.J., Sloan E.D., "Experimental Determination of Methane Hydrate Stability in Methanol and Electrolyte Solutions", *Fluid Phase Equilibria*, 193(1-2), 17-28, 2002.

Jamaluddin A.K.M., Kalogerakis N., Bishnoi P.R., "Hydrate Plugging Problems in Undersea Natural Gas Pipelines Under Shutdown Conditions", *Journal of Petroleum Science and Engineering*, 5(4), 323-335, 1991.

Jassim E., Abedinzadegan Abdi M., Muzychka Y., "Computational Fluid Dynamics Study for Flow of Natural Gas through High Pressure Supersonic Nozzles: Part 1- Real Gas Effects and Shockwave", in press, Journal of Petroleum Science and Technology, PET/06/097, 2006.

Jassim E., Abedinzadegan Abdi M., Muzychka Y., "Computational Fluid Dynamics Study for Flow of Natural Gas through High Pressure Supersonic Nozzles: Part 2- Nozzle Geometry and Vorticity", in press, Journal of Petroleum Science and Technology, PET/06/098, 2006.

Jassim E., Abedinzadegan Abdi M., Muzychka Y., "Simulation of Natural Gas Flow through Complex Geometries Using CFD", the International Oil and Gas CFD Conference (IOCC), London, UK, 30 November – 1 December, 2006c.

Jassim E., Abedinzadegan Abdi M., Muzychka Y., "A CFD-Based Model to Locate Flow Restriction Induced Hydrate Deposition in Pipelines", proceedings in the 2008 Offshore Technology Conference, OTC 08, Houston, USA, May 5-8, 2008.

John J.E. and Keith T.G., "Gas Dynamics", 3<sup>rd</sup> Edition, Pearson Prentice Hall, 2006.

Joseph G.G., Zenit R., Hunt M.L., Rosenwinkel A.M., "Particle-Wall Collision in a Viscous Fluid", Journal of Fluid Mechanics, 433, 329-346, 2001.

Junge C., "Air Chemistry and Radioactivity", New York, Academic Press, 382, 1963.

Karaaslan U., and Parlaktuna M., "PEO-a New Hydrate Inhibitor Polymer", *Energy Fuels*, 16, 1387-1391, 2002.

Kaftori D., Hetsroni G., Banerjee S., "Particle Behavior in the Turbulent Boundary Layer. I: Motion, Deposition and Entrainment", *Physics of Fluids* 7, 1095–1106, 1995.

Kaftori D., Hestroni G., Banerjee S., "Particle Behavior in the Turbulent Boundary Layer. II: Velocity and Distribution Profiles", *Phys. Fluids* 7, 1107–1121, 1995.

Kashchiev D., "Nucleation Basic Theory with Application", Oxford: Butterworth-Heinemann, 2000.

Kawamura T., Komai T., Yamamoto Y., Nagashima K., Ohga K., Higuchi K., "Growth Kinetic of CO<sub>2</sub> Hydrate Just below Melting Point of Ice", *J. of Crystal Growth*, 234, 220-226, 2002.

Kelkar S.K., Selim M.S., Sloan E.D., "Hydrate Dissociation Rates in Pipeline", *Fluid Phase Equilibria*, 150(15), 371-382, 1998.

Kelland M.A., "History of the Development of Low Dosage Hydrate Inhibitors", *Energy and Fuels*, 20 (3), 825-847, 2006.

Kim H.C., Bishnoi P.R., Heidemann R.A., Rizvi S.S.H., "Kinetics of Methane Hydrate Decomposition", *Chemical Engineering Science*, 42(7), 1645–1653, 1987.

Klapproth A., Goreshnik E., Staykova D., Klein H., Kuhs W.F., "Structural Studies of Gas Hydrates", Canadian Journal of Physics, 81, 503-518, 2003.

Knox W.G, Hess M., Jones G.E., Smith H.B., "The Clathrate Process", Chem. Eng. Prog., 57, 66-71, 1961.

Koh C.A., Westacott R.E., Zhang W., Hirachand K., Creek J.L., Soper A.K., "Mechanisms of Gas Hydrate Formation and Inhibition", Fluid Phase Equilibria, 194(197), 143-151, 2002.

Kono H.O., Narasimhan S., Song F., Smith D.H., "Synthesis of Methane Gas Hydrate in Porous Sediments and its Dissociation by Depressurizing", Powder Technology, 122, 239-246, 2002.

Koyama H., and Watanabe K., "Identification of Partial Plugging in a Gas-Transport Pipeline by an Acoustic Method", Applied Acoustics, 40 (1), 1-19, 1993.

Krupp H., "Particle Adhesion Theory and Experiment", Adv. Colloid Interface Sci., 2, 111 1967.

Kulmala M., and Vesala T., "Mass Transfer from a Drop - II. Theoretical Analysis of Temperature Dependent Mass Flux Correlation", Int. J. Heat Mass Transfer, 38, 1705-1708, 1995.

Kvamme B., and Kuznetsova T., "Hydrate Dissociation in Chemical Potential Gradients: Theory and Simulation", *Fluid Phase Equilibria*, 217, 217-226, 2004.

Kvamme B., Kuznetsova T., Aasoldsen K., "Molecular Simulation as a Tool for Selection of Kinetic Hydrate Inhibitors", *Molecular Simulation*, 31(14-15), 1083-1094, 2005.

Kvasnak W., Ahmadi G., Bayer R., Gaynes M., "Experimental Investigation of Dust Particle Deposition in a Turbulent Channel Flow", *Journal of Aerosol Science*, 24 (6), 795-815, 1993.

Kvenvolden K.A., "Methane Hydrate: A Major reservoir of Carbon in the Shallow Geosphere", *Chem Geol*, 71 (1-3), 41-51, 1988.

Kvenvolden K.A., "A Review of the Geochemistry of Methane in Natural Gas Hydrate", *Org Geochemical*, 23(11-12), 997-1008, 1995.

Lahey R.T., and Drew D.A., "The Current State of the ART in the Modeling of the Vapour-Liquid Two Phase Flow", *ASME*, n90-WA/HT-13, 1990.

Larsen R., Wessel-Berg D., Borthne G., Nakamura A., "Simple Modeling of Hydrate Dissociation in Reservoirs Caused by Pressure Drawdown", *Proceedings of the International Symposium on Methane Hydrates Resources in the Near Future*, JNOC, 175-182, 1998.

Lederhos J.P., Long J.P, Sum A., Christiansen R.L., Sloan E.D., "Effective Kinetic Inhibitors For Natural Gas Hydrates", *Chemical Engineering Science*, 51(8), 1221-1229, 1996.

Lee S, Liang L., Riestenberg D., West O.R., Tsouris C., Adams E., "CO<sub>2</sub> Hydrate Composite for Ocean Carbon Sequestration", *Environment Science Technology*, 37, 3701-3708, 2003.

Lee S., McGregor E., Holder G.D., "Experimental Study of Hydrate Crystal Growth from Methane, Carbon Dioxide, and Methane + Propane Mixtures", *Energy and Fuels*, 12, 212-215, 1998.

Legendre D., Zenit R., Daniel C., Guiraud P., "A Note on the Modeling of the Bouncing of Spherical Drops or Solid Spheres on a Wall in Viscous Fluid", *Chemical Engineering Science*, 61, 3543-3549, 2006.

Legendre D., Daniel C., Guiraud P., "Experimental Study of a Drop Bouncing on a Wall in a Liquid", *Physics of Fluids*, 17(1), 1-13, 2005.

Leighton D., and Acrivos A., "The Lift on a Small Sphere Touching a Plane in the Presence of a Simple Shear Flow", *Journal of Applied Mathematics and Physics*, 36, 174-178, 1985.

Li J., Kaihua G., Deqing L., Ruzhu W., "Experiments on Fast Nucleation and Growth of HCFC141b Gas Hydrate in Static Water Columns", *International Journal of Refrigeration*, 27, 932-939, 2004.

Li A., and Ahmadi G., "Dispersion and deposition of spherical particles from point sources in a turbulent channel flow", *Journal of Aerosol Science Technology*, 16, 209-226, 1991.

Li A., and Ahmadi G., "Deposition of aerosols on surfaces in a turbulent channel flow", *International Journal of Engineering Science*, 31, 435-451, 1993.

Li A., Ahmadi G., Bayer R., Gaynes M., "Aerosol particle deposition in an obstructed turbulent duct flow", *Journal of Aerosol Science*, 25, 91-112, 1994.

Liu B.Y.H., and Agarwal J.K., "Experimental observation of aerosol deposition in turbulent flows", *Journal of Aerosol Science*, 5, 145-155, 1974.

Liu X.Y., Du N., Hew C., "Ice Nucleation Inhibition: Mechanism of Antifreeze by Antifreeze Protein", *The Journal of biological chemistry*, 278(38), 36000-36004, 2003.

Long J.P., and Sloan E.D., "Hydrates in the Ocean and Evidence for the Location of Hydrate Formation", *Int. Journal of Thermophysics*, 17(1), 1-13, 1996.

Lysne D., "An Experimental Study of Hydrate Plug Dissociation by Pressure Reduction," Ph.D. Thesis, Norwegian Institute of Technology, University of Trondheim, 1995.

Mahmood A.E, and Bishnoi P.R., "Equilibrium Data for Methane, Ethane, and Propane Incipient Hydrate Formation in Aqueous Solutions of Ethylene Glycol and Diethylene Glycol", *J Chem Eng Data*, 47(2), 278-281, 2002.

Manakov Yu., Goryainov S.V., Kurnosov A.V., Likhacheva Yu., Dyadin Y.A., Larionov E.G., "Clathrate Nature of the High-Pressure Tetrahydrofuran Hydrate Phase and Some New Data on the Phase Diagram of the Tetrahydrofuran-Water System at Pressures up to 3 GPa", *J. Phys. Chem. B*, 107, 7861-7866, 2003.

Marie J.L., Moursali E., Tran-Cong S., "Similarity Law and Turbulence Intensity Profiles in a Bubbly Boundary Layer at Low Void Fractions", *Int. J. Multiphase Flow* 23, 227-247, 1997.

Mahtews M., "Logging Characteristics of Methane Hydrate", *Log Analyst*, 27(3), 26-63, 1986.

Makogon Y.F., "Hydrate of Natural Gas", Penn Well Publishing: Tulsa, OK, (translated by W.J. Cieslewicz), 1981.

Makogon Y.F., "Natural Gas Hydrates: The state of Study in the USSR and Prerspectives for its Use", In: *Third Chemical Congress of North America*, Toronto, Canada, 1988.

Makogon Y.F., "Hydrate of Hydrocarbons", Penn Well Publishing: Tulsa, OK, 1997.

Mann S.L., McClure L.M., Poettmann F.H., and Sloan E.D., "Vapour-Solid Equilibrium Ratios for Structure I and II Natural Gas Hydrates", Proceedings of the 68<sup>th</sup> GPA Annual Convention, 60-74, San Antonio, TX, 1989.

Masoudi R., and Tohidi B., "Gas-Hydrate Production for Natural-Gas Storage and Transportation", J. of Petroleum Technology, 57(11), 73-74, 2005.

Masuda Y., Kurihara M., Ochuchi H., Sato T., "A Field-Scale Simulation Study on Gas Productivity of Formations Containing Gas Hydrates", Proceedings of the Fourth International Conference on Gas Hydrates, Yokohama, Japan, 2002.

Max, M.D. and Pellenbarg, R.E., "Desalination Through Methane Hydrate", U.S. Patent (23 February) No 5,873,262, 1999.

McGlashan M.L., "Chemical Thermodynamics", Academic Press, London, page 176, 1979.

McLaughlin J.B., "The Lift on a Small Sphere in Wall-Bounded Linear Shear Flows", Journal of Fluid Mechanics 246, 249-265, 1993.

McLinden M.O., Gallagher J.S., Weber L.A., Morrison G., Ward D., Goodwin A.R., Moldover M.R., Schmidt J.S., Chae H.B., Bruno T.J., Ely J.F., Huber M.L., "Measurement and Formulation of the Thermodynamic Properties of Refrigerants 134a and 123," ASHRAE Trans., 95(Pt.2):2095, 1988.

Mehta A., Hudson J., Peters D., "Risk of Pipeline Over-Pressurization during Hydrate Remediation by Electrical Heating", Paper presented at the Chevron Deepwater Pipeline and Riser Conference, Houston, TX, 2001.

Miguel A.F., Reis A., Aydin M., "Aerosol particle deposition and distribution in bifurcating ventilation ducts", *Journal of Hazardous Materials*, B116, 249-255, 2004.

Mollinger A.M., Nieuwstadt F.T.M., "Measurement of the Lift Force on a Particle Fixed to the Wall in the Viscous Sublayer of a Fully Developed Turbulent Boundary Layer", *Journal of Fluid Mechanics* 316, 285-306, 1996.

Mokhatab S., Poe W.A., Speight J.G., "Handbook of Natural Gas Transmission and Processing", Elsevier Inc., 1<sup>st</sup> edn. 2006.

Monfort J.P., and Nzihou A., "Light Scattering Kinetics Study of Cyclopropane Hydrate Growth", *J. of Crystal Growth*, 128(1-4), 1182-1186, 1993.

Mshfeghian M., and Maddox R.N., "Method predicts Hydrate for High-Pressure Gas Streams", *Oil and Gas Journal*, 1993.

Nadkarni A.R., and Mahalingam R., "Aerosol Behaviour in Temperature and Concentration Gradient Fields in Nonisothermal Tube Flow", *AIChE Journal*, 31(4), 603-614, 1985.

Natarajan V., and Bishnoi P.R., "Induction Phenomena in Gas Hydrate Nucleation", *Journal of Chemical Engineering Science*, 49, 2075-2081, 1994.

Nerheim A.R., Svartas T.M., Samuelsen E.K., "Investigation of Hydrate Kinetics in the Nucleation and Early Growth Phase by Laser Light", *Proceedings Second International Offshore and Polar Engineering Conference*, San Francisco, 620-627, June 14-19, 1992.

Ng H.J., and Robinson D.B., "Hydrate Formation in Systems Containing Methane, Ethane, Propane, Carbon Dioxide or Hydrogen Sulfide in the Presence of Methanol", *Fluid Phase Equilibria*, 21(1-2), 145-155, 1985.

Osegovic J.P., Tatro S.R., Holman S.A., Hearts A.L., Max M.D., "Growth Kinetics of Ethane Hydrate From a seawater Solution at an Ethane Gas Interface", *Division of Petroleum Chemistry*, 50(1), 87-89, 2005.

Palin D.E., and Powell H.M., "Hydrogen Bond Linking of Quinol Molecules", *Nature*, 156, 334-335, 1945.

Pangborn J.B., and Barduhn A.J., "The Kinetics of Methyl Bromide Hydrate Formation", *Desalination*, 8, 35-68, 1970.

Papavergos P.G., and Hedley A.B., "Particle deposition behavior from turbulent flow", *Chemical Engineering Research and Design*, 62, 275-295, 1984.

Parameswaran V.R., Paradis M., Handa Y.P., "Strength of Frozen Sand Containing Tetrahydrofuran Hydrate." *Canadian Geotechnical Journal*, 26, 479-483, 1989.

Patankar, S. V., "Numerical heat transfer and fluid flow." McGraw-Hill, New York, 1980.

Pauling L., and Marsh R.E., "The Structure of Chlorine Hydrate", *Proceedings Natl. Acad. Science, USA*, 38, 112-118, 1952.

Peng D.Y., and Robinson D.B., "A New two-Constant Equation of State," *Ind. Eng. Chem. Fundam.*, 15:59, 1976.

Peters D.J., Selim M.S., Sloan E.D., "Hydrate Dissociation in Pipelines by Two-Sided Depressurization: Experiment and Model", DEEPStar final report, 1999.

Peters D.J., Mehta A., Walsh J., "The Physics of Hydrate Plug Dissociation: A Comprehensive Model Based upon Facts, Conjecture, and Field Experience", *Proceedings 4<sup>th</sup> International Conference on Natural Gas Hydrates, Yokohama, 952, May 2002.*

Pinder K.L., "Time Dependent Rheology of the Tetrahydrofuran Hydrogen Sulfide Gas Hydrate Slurry", *Can. J. Chem. Eng.*, 132-138, 1964.

Pope S.B., "Turbulent Flows", Cambridge University Press, 2000.

Prigogine I., and Defay R., "Chemical Thermodynamics", transl. D.H.Everett, Longmans Green, London, 145, 1954.

Rashidi M., Hetsroni G., Banerjee S., "Particle-Turbulence Interaction in a Boundary Layer", International Journal of Multiphase Flow, 16(6), 935-949, 1990.

Redlich O., and Kwong J.N., "On the Thermodynamics of Solutions. V. An Equation of State. Fugacities of Gaseous Solutions," Chem. Rev., 44:233, 1949.

Richard D., and Quéré D., "Bouncing Water Drops", Europhysics Letter, 50 (6), 769-775, 2000.

Ripmeester J.A., Tse J.S., Ratcliffe C.I., Powell B.M., "A New Clathrate Hydrate Structure", Nature, 325, 135-136, 1987.

Ripmeester J.A., and Ratcliffe C.I., "Xe-129 NMR Studies of Clathrate Hydrates: New Guests for Structure II and Structure H", Journal of Phys. Chem., 94, 8773-8776, 1990.

Robinson D.B., and Peng D.Y., "The characterization of the Heptanes and Heavier Fractions for the GPA Peng-Robinson Programs", GPA research Report, 28, Tulsa, 1978.

Ropelato K., Meier H., Cremasco M.A., "A Renewed CFD Model for Prediction of Gas-Solid Flow in Downer Reactor", Pressure Vessel and Piping Conference, 491 (1), 235-241, 2004.

Rowlinson J.S., "Liquids and Liquid Mixtures", Butterworths, London, 2nd edn., 66, 1969.

Saffman P.G., "The Lift on a Small Sphere in a Slow Shear Flow", J. Fluid Mech., 31, 264, 1968.

Sakrani S., JIE L.Q., WAHAB Y., "The Formation of Nanoscale Clusters-Nanofilms/Quantum Dots Predicted Using a Capillary Model of Nucleation", Journal of Fundamental Science, 1, 23-33, 2005.

Salim P.H., and Trebble M.A., "A modified Trebble-Bishnoi equation of state: thermodynamic consistency revisited", Fluid Phase Equilibria, 65, 59-71, 1991.

Savandal A., Kvamme B., Granasy L., Pusztai T., Buanes T., Hove J., "The Phase-Field Theory Applied to CO<sub>2</sub> and CH<sub>4</sub> Hydrate", Journal of Crystal Growth, 287, 486-490, 2006(a).

Savandal A., Kuznetsova T., Kvamme B., "Thermodynamic Properties and Phase Transitions in the H<sub>2</sub>O/CO<sub>2</sub>/CH<sub>4</sub> System", Fluid Phase Equilibria, 246, 177-184, 2006(b).

Scanlon W.J., and Fennema O., "Gas Hydrate in Aquous Organic Systems VII; Linear Crystallization Velocities of the Hydrate of Ethylene Oxide and Tetrahydrofuran", *Cryobiology*, 8, 249-254, 1972.

Schwendiman L.C., and Postma A.K., "Hanford Laboratory Report HW-SA-2236", Richland, Washington, U.S.A., 1961.

Sehmel G.A., "Aerosol deposition from turbulent airstreams in vertical conduits", Batelle Northwest Laboratory Report BNWL-578, Richland, Washington, U.S.A., 1968.

Shams M., Ahmadi G., Rahimzadah, H., "A sublayer model for deposition of nano- and micro-particles in turbulent flows", *Chemical Engineering Science*, 55, 6097-6107, 2000.

Shimada W., Shimada W., Ebinuma T., Oyama H., Kamata Y., Narita H., "Free-Growth Forms and Growth Kinetics of Tetra-n-Butylammonium Bromide Semi-Clathrate Hydrate Crystals", *Journal of Crystal Growth*, 274, 246-250, 2005.

Sira J.H., Patil S.L., Kamath V.A., "Study of Hydrate Dissociation by Methanol and Glycol Injection", *SPE Annual Technical Conference and Exhibition*, 977-984, 1990.

Siriwardane J.H., and Smith H.D., "Synthesis of Methane Hydrate in an Unconsolidated Medium", *J. of Testing and Evaluation*, 30(1), 1-7, 2002.

Skovborg P., Ng H.J., Rasmussen P., Mohen U., "Measurement of Induction Times for the Formation of Methane and Ethane Gas Hydrates", *Chemical Engineering Science*, 48(3), 445-453, Feb.1993.

Sosnowski T.R., Moskal A., Gradon L., "Mechanism of aerosol particle deposition in the Oropharynx under non-steady airflow", *Annals of Occupational Hygiene*, 51, 19-25, 2007.

Sloan E.D., "Clathrate Hydrate of Natural Gases", 2<sup>nd</sup> edn., Cap. 2, Marcel Dekker, New York, 455-464, 1998.

Sloan E.D., "Clathrate Hydrates: The Other Common Solid Water Phase", *Ind. Eng. Chem Res*, 39, 3123-3129, 2000.

Sloan E.D., "Fundamental principles and applications of Natural Gas Hydrates", *Nature Publication Group*, 426, 353-359, Nov. 2003.

Stoll R.D., and Bryan G.M., "Physical-Properties of Sediments Containing Gas Hydrate", *Journal of Geophysical Research*, 84 (4), 1629-1634, 1979.

Sun C., "Induction Period of Hydrate Formation in a Flow System", *Chinese Journal of Chemical Engineering*, 12(4), 527-531, 2004.

Sun X., and Mohanty K.K., "Kinetic Simulation of Methane Hydrate Formation and Dissociation in Porous Media", *Chemical Engineering Science* 61, 3476 – 3495, 2006.

Sun Z.G., Fan S.S., Shi L., Guo Y.K., Guo K.H., "Equilibrium Conditions for Hydrate Dissociation for a Ternary Mixture of Methane, Ethane, and Propane in Aqueous Solutions of Ethylene Glycol and Electrolytes", *J Chem Eng Data*, 46(4), 927-929, 2001.

Svandal A., Kvamme B., Grønås L., Pusztai T., "The Influence of Diffusion on Hydrate Growth", *J. of Phase Equilibrium and Diffusion*", 26(5), 534-538, 2005.

Takeya S., Kida M., Minami H., Sakagami H., Hachikubo A., Takahashi N., Shoji H., Soloviev V., Wallmann K., Biebow N., Obzhairov A., Salomatin A., Poort J., "Structure and Thermal Expansion of Natural gas Clathrate Hydrates", *Chemical Engineering Science*, 61(8), 2670-2674, 2006.

Tanaka H., Tamai Y., Koga K., "Large Thermal Expansivity of Clathrate Hydrates", *Journal of Physics and Chemistry*, 101 (33), 1997.

Tanasawa I., and Takao S., "Low-Temperature Storage Using Clathrate Hydrate Slurries of Tetra-n-Butylammonium Bromide: Thermo-physical Properties and Morphology of Clathrate Hydrate Crystals", In: *Fourth International Conference on Gas Hydrates*, Yokohama, Japan, 963-967, 2002.

Tandon P., and Rosner D.E., "Co-Deposition on Hot CVD Surfaces: Particles Dynamics and Deposit Roughness Interaction", *AIChE Journal*, 42(6), 1673-1684, 1996.

Taniere A., Oesterle B., Monnier J.C., "On the Behaviour of Solid Particles in a Horizontal Boundary Layer with Turbulence and Saltation Effects", *Exp. Fluids*, 23, 463-471, 1997.

Tegze G., Pusztai T., Toth G., Granasy L., Svandal A., Buanes T., Kuznetsova T., Kvamme B., "Multiscale Approach to CO<sub>2</sub> Hydrate Formation in Aqueous Solution: Phase Field Theory and Molecular Dynamics. Nucleation and Growth", *The Journal of Chemical Physics*, 124, 1-12, 2006.

Terenzi A., "Influence of Real-Fluid Properties in Modeling Decompression Wave Interacting with Ductile Fracture Propagation", *Oil and Gas Science and Technology*, 60(4), 2005.

Thomas S., and Dawe R.A., "Review of Ways to Transport Natural Gas Energy from Countries which do not Need the Gas for Domestic Use", *Energy*, 28, 1461-1477, 2003.

Tian, L., and Ahmadi G., "Particle deposition in turbulent duct flow-comparisons of different model predictions", *Journal of Aerosol Science*, 38, 377-397, 2007.

Tohidi B., Ostergaard K.K., Danesh A., Todd A.C., Burgass R.W., "Structure-H Gas Hydrates in Petroleum Reservoir Fluids", *Can. J. of Chem. Eng.*, 79(3), 384-391, 2001.

Tohidi B., "Can 2-Propanol Form Clathrate Hydrate?", *Ind. Eng. Chem. Res.*, 41, 2064-2068, 2002.

Towler B.F., and Mokhatab S., "Quickly Estimate Hydrate Formation Conditions in Natural Gases", *Hydrocarb. Proc.* 84(4), 61-62, 2005.

Twu C.H., Coon J.E., Cunningham J.R., "A New Generalized Alpha Function for a Cubic Equation of State", *Fluid phase equilibria*, , 105(1), 49-59, 1995.

Van der Walls J.H. and Platteeuw J.C., "Clathrate Solutions", *Advanced Chemistry Physics* 2, 1-58, 1959.

Verwey E.J., Overbeek J.T.G, *Theory of the Stability of Lyophobic Colloids*, Elsevier, Amsterdam, 1948.

Vincent J.H., "Aerosol Science for Industrial Hygienists", 1<sup>st</sup> Edition, Elsevier Science Inc., New York, 1995.

von Stackelberg M., "Feste Gashydrate, Naturwissenschaften", 327-333, 1949a.

von Stackelberg M., "Feste Gashydrate, Naturwissenschaften", 359-363, 1949b.

von Stackelberg M., and Muller H.R., "On the Structure of Gas Hydrates", J. Chem. Phys, 1319-1320., 1951.

Vyhnalikova J., Taniere A., Huilier D., "Numerical Simulation of the Dispersion of Heavy Particles in a Turbulent Boundary Layer", Proceedings of FEDSm\_98, 1998 ASME Fluids Engineering Division Summer Meeting, 21-25 June 1998.

Vysniauskas A., and Bishnoi P.R., "Thermodynamics and Kinetics of Gas Hydrate Formation, In Natural Gas Hydrates: Properties, Occurrence and Recovery", Cox, J.L., Ed., Butterworth: Woburn, Ma, 35-48, 1983.

Vysniauskas A., and Bishnoi P.R., "A Kinetic Study of Methane Hydrate Formation", Chem. Eng. Science, 38, 1061-1072, 1983.

Wachi S., and Jones A.G., "Mass Transfer with Chemical Reaction and Precipitation", Chemical Engineering Science, 46, 1027, 1991.

Wang J., and Levy E.K., "Particle Motions and Distributions in Turbulent Boundary Layer of Air-Particle Flow Past a Vertical Flat Plate", Experimental Thermal and Fluid Science, 27, 845-853, 2003.

Wark K. Jr., "Advanced Thermodynamics for Engineers", McGraw-Hill series, 1995.

Wataru S., and Takeo H., "In Situ Observation of the Transformation from Air Bubbles to Air Clathrate Hydrate Crystals Using a Mizuho Ice Core", *J. of Crystal Growth*, 265, 309-317, 2004.

Wells A.C., and Chamberlain A.C., "Transport of Small Particles to Vertical Surfaces", *Brit. J. Appl. Phys.*, 18, 1793, 1967.

Wells A.C., and Chamberlain A.C., "Deposition of dust from turbulent gas streams", *Atmos. Envir.* 3, 494-496, 1969.

Werezak G.N., "Unusual Methods of Separation", *AIChE Symposium Ser.*, 65(91), 6-18, 1969.

Whitaker S., "Improved Constraints for the Principle of Local Thermal Equilibrium", *Industrial Engineering Chemistry Res.*, 30, 983-997, 1991.

White F.M., "Fluid Mechanics", 5<sup>th</sup> ed., McGraw-Hill Inc., New York, 2003.

Wilkens R.J., "Flow Assurance". In *Fluid Flow Handbook*, (J. Saleh, ed.), Chapter 29. McGraw-Hill, New York, 2002.

Wood N.B., "The mass transfer of particles and acid vapour to cooled surfaces" *J. Inst. Energy* 76, 76-93, 1981.

Wuebbles D.J, Hayhoe K., "Atmospheric Methane and Global Change", *Earth-Sci Rev*, 57, 177-210, 2002.

Xu Z., Matthews P., Talley L., Turner D., Yang S., Boxall J., Kleehamer D., Koh C., Miller K., Sloan E.D., "Development of a Hydrate Kinetic Model and its Incorporation into the OLGA2000<sup>R</sup> Transient Multi-phase Flow Simulator", Proceedings in international Conference on Gas Hydrate ICGH, Trondheim, Norway, 2005.

Yang C., Dabros T., Li D., Czarnecki J., Masliyah J.H, J., "Kinetics of particle transport to a solid surface from an impinging jet under surface and external force fields." *Journal Colloid and Interface Science*, 208, 226-240, 1998.

Yang J.L., "Condensational Growth of Atmospheric Aerosol Particles in an Expanding Water Saturated Air Flow: Numerical Optimization and Experiment", PhD Thesis, Mainz, 1999.

Yingming X., Kaihua G., Deqing L., Shuanshi F., Jianming G., "Steady Gas Hydrate Growth along Vertical Heat Transfer Tube without Stirring", *Chemical Engineering Science*, 60(3), 777-786, 2005(a).

Yingming X., Kaihua G., Deqing L., Shuanshi F., Jianming G., Jinggu C., "Gas Hydrate Fast Nucleation from Melting Ice and Quiescent Growth along Vertical Heat Transfer Tube", *Science in China. Chemistry. Series B*, 48 (1), 75-82, 2005(b).

Yokozeiki A., "Methane Gas Hydrate Viewed through Unified Solid-Liquid-Vapour Equation of State", *Int. Journal of Thermodynamics*, 26 (3), 2005.

Young J.B., and Hanratty T.J., "Optical Studies on the Turbulent Motion of Solid particles in a pipe flow", *J. Fluid Mech.* 231, 665–688, 1991.

Young J., and Leeming A., "A Theory of Particle Deposition in Turbulent Pipe Flow", *J. Fluid Mech.* 340, 129–159, 1997.

Younglove B.A., and McLinden M.O., "An international standard equation-of-state formulation of the thermodynamic properties of refrigerant 123 (2,2-dichloro-1,1,1-trifluoroethane)", *J. Phys. Chem. Ref. Data*, 23(5), 731-779, 1994.

Yousif M.H., Abass H.H., Selim M.S., Sloan E.D., "Experimental and Theoretical Investigation of Methane-Gas-Hydrate Dissociation in Porous Media", *SPE Reservoir Engineering*, 6, 69–76, 1991.

Yung B.P.K., Merry H., Bott T.R., "The Role of Turbulent Brusters in Particle Re-Entrainment in Aqueous Systems", *Chem. Engng Science*, 44, 873-882, 1989.

Zettlemoyer, "Nucleation", MARCEL DEKKER INC., New York, 1969.

Zhao Y., GUO K., Liang D., Fan S., Liu X., Shu B., Ge X., Liu Y., "Formation Process and Fractal Growth Model of HCFC-141b Refrigerant Gas Hydrate", *Science in China. Chemistry*, 45(2), 216-224, 2002.

Zivi S.M., "Estimation of Steady-State Void Fraction by Means of the Principle of Minimum energy Production", *J. of Heat Transfer*, 86, 247-252, 1964.

Zun I., Kljenak I., Moze S., "Space-Time Evolution of the Non-Homogeneous Bubble Distribution in Upward Flow", *International Journal of Multiphase Flow*, 19(1), 151-172, 1993.

## Appendix-A

### Solution of Eq. 4.22

The general Partial Differential Equation of the Particle Distribution Function is:

$$\frac{\partial n}{\partial t} + \frac{\beta_1}{r_p} \frac{\partial n}{\partial r_p} - \frac{\beta_1 n}{r_p^2} = 0 \quad \text{A-1}$$

The method of separation of variables may be used by assuming that the product solution of the form:

$$n(t, r) = T(t).R(r) \quad \text{A-2}$$

By differentiating Eq. (A-2) and substituting into A-1 yield the following expression:

$$R \cdot \frac{\partial T}{\partial t} + \frac{\beta_1}{r} T \cdot \frac{\partial R}{\partial r} - \frac{\beta_1}{r^2} T \cdot R = 0 \quad \text{A-3}$$

Dividing A-3 by A-2:

$$\frac{\frac{\partial T}{\partial t}}{T(t)} = \frac{\beta_1}{r^2} - \frac{\beta_1}{r} \frac{\frac{\partial R}{\partial r}}{R(r)} \quad \text{A-4}$$

Eq. (A-4) can only be satisfied if the left hand side and the right hand side are equal a constant ( $\lambda$ ) which should be equal to any real number including zero. In other words:

$$\frac{\frac{\partial T}{\partial t}}{T(t)} = \frac{\beta_1}{r^2} - \frac{\beta_1}{r} \frac{\frac{\partial R}{\partial r}}{R(r)} = 0, c_1 \quad \text{A-5}$$

Examination of the case equal zero leads to the fact that no time dependant exists and this violates the original assumption, which says the size distribution is function of time and growth.

However, for the other case we obtain the following expressions:

$$T(t) = \exp(c_1 t) \quad \text{A-6}$$

$$R(r) = Ar \exp\left(\frac{-c_1 r^2}{2\beta_1}\right) \quad \text{A-7}$$

$$n(t, r) = Ar \exp\left(c_1 \left(t - \frac{r^2}{2\beta_1}\right)\right) \quad \text{A-8}$$

Where,  $A$  and  $c_1$  are constants

The constants in Eq. (A-8) can be estimated using initial and boundary conditions. We consider that the first nucleation occurs with the concentration of sites in the system, on which the clusters of the new phase can form, is denoted by  $n_0$  (particle per  $\text{m}^3$ ). Hence the initial condition would be the condition that all the particles have sizes of critical radius:

$$n(0, r_c) = n_0 = \text{constant} \quad \text{A-9}$$

And the boundary condition is:  $\frac{\partial n}{\partial r}\bigg|_{r_c, t} = 0$  A-10

Substituting the boundary condition leads to:

$$c_1 = \frac{\beta_1}{r_c^2}; \quad \text{A-11}$$

now equation(A-8) reduced to:

$$n(t, r) = Ar \exp\left(\frac{1}{r_c^2} (\beta_1 t - \frac{r^2}{2})\right) \quad \text{A-12}$$

Then from the initial condition, the constant  $A$  can be estimated as:

$$A = 1.65 \frac{n_0}{r_c}$$

The hydrate size distribution function due to mass transfer would be:

$$n(t, r) = 1.65 n_0 \frac{r}{r_c} \exp\left(\frac{1}{2r_c^2} (2\beta_1 t - r^2)\right) \quad \text{A-13}$$

Introducing the Fourier number  $Fo = \frac{\beta_1 t}{r_c^2}$ , the reduced radius  $r^* = \frac{r}{r_c}$ , and a dimensionless

parameter  $n^* = \frac{n}{n_0}$ , Eq. (23) becomes:

$$n^*(t, r) = 1.65 r^* \exp\left( Fo - \frac{r^{*2}}{2} \right) \quad \text{A-14}$$

## Appendix-B

### Solution of Eq. 4.29

The general Partial Differential Equation of the Particle Distribution Function (PDF) is:

$$\frac{\partial n}{\partial t} + \left( \beta_2 r + \frac{\beta_1}{r} \right) \frac{\partial n}{\partial r} + \left( \beta_2 - \frac{\beta_1}{r^2} \right) n = 0 \quad \text{B-1}$$

The method of separation of variables may be used by assuming that the product solution of the form:

$$n(t, r) = T(t).R(r) \quad \text{B-2}$$

By differentiating Eq. (B-2) and substituting into B-1 yield the following expression:

$$R. \frac{\partial T}{\partial t} + \left( \beta_2 r + \frac{\beta_1}{r} \right).T. \frac{\partial R}{\partial r} + \left( \beta_2 - \frac{\beta_1}{r^2} \right).T.R = 0 \quad \text{B-3}$$

Dividing B-3 by B-2:

$$\frac{\frac{\partial T}{\partial t}}{T(t)} = - \left( \beta_2 r + \frac{\beta_1}{r} \right) \frac{\frac{\partial R}{\partial r}}{R(r)} - \left( \beta_2 - \frac{\beta_1}{r^2} \right) \quad \text{B-4}$$

Eq. (B-4) can only be satisfied if the left hand side and the right hand side are equal a constant

( $\lambda$ ) which should be equal to any real number including zero. In other words:

$$\frac{\frac{\partial T}{\partial t}}{T(t)} = - \left( \beta_2 r + \frac{\beta_1}{r} \right) \frac{\frac{\partial R}{\partial r}}{R(r)} - \left( \beta_2 - \frac{\beta_1}{r^2} \right) = 0, \lambda \quad \text{B-5}$$

Examination of the case equal zero leads to the fact that no time dependant exists and this

violates the original assumption, which says the size distribution is function of time and growth.

However, for the other case we obtain the following expressions:

$$T(t) = \exp(\lambda t) \quad \text{B-5a}$$

$$R(r) = \frac{Ar}{(\beta_2 r^2 + \beta_1)^{(1 + \frac{\lambda}{2\beta_2})}} \quad \text{B-5b}$$

Hence:

$$n(t, r) = \frac{Ar \exp(\lambda t)}{(\beta_2 r^2 + \beta_1)^{(1 + \frac{\lambda}{2\beta_2})}} \quad \text{B-6}$$

where  $A$  and  $\lambda$  are the arbitrary constants and can be found from initial and boundary conditions.

Now our initial condition assumes that the time begins after the particles reach its critical size because unlike critical particles, any particle with a size less than the critical value will be vanished if the driving force is eliminated.

We consider that the first nucleation occurs with the concentration of sites in the system, on which the clusters of the new phase can form, is denoted by  $n_0$  (particle per  $m^3$ ). Hence the initial condition would be the condition that all the particles have sizes of critical radius:

$$n(0, r_c) = n_0 = \text{constant}$$

And the boundary condition is:  $\left. \frac{\partial n}{\partial r} \right|_{r_c} = 0$

Substituting the boundary conditions leads to the value of the constant  $\lambda$ :

$$\lambda = \frac{\beta_1}{r_c^2} - \beta_2 \quad \text{B-7}$$

since  $r_c \sim o(10^{-9})$ ;  $\beta_2 \sim o(10^{-5})$ ;  $\beta_1 \sim o(10^{-12})$ , the more significant term of Eq. B-7 is the first term. Thus:

$$\lambda \approx \frac{\beta_1}{r_c^2} \quad \text{B-8}$$

Then from the initial condition, the constant  $A$  can be estimated as:

$$A = n_0 \left( r_c \beta_2 + \frac{\beta_1}{r_c} \right) (\beta_2 r_c^2 + \beta_1)^{\frac{\beta_1}{2\beta_2 r_c^2}} \quad \text{B-9}$$

Again as  $r_c \sim o(10^{-9})$ ;  $\beta_2 \sim o(10^{-5})$ ;  $\beta_1 \sim o(10^{-12})$ , the term  $(r_c \beta_2)$  is  $o(10^{-14})$  while the term  $(\frac{\beta_1}{r_c})$  is  $o(10^{-3})$ , in which is the dominated term.

The final form of the hydrate size distribution function would be:

$$n(t, r) = n_0 \frac{\beta_1}{r_c} \frac{r \exp(\frac{\beta_1}{r_c^2} t)}{\beta_2 r^2 + \beta_1} \underbrace{\left( \frac{\beta_2 r_c^2 + \beta_1}{\beta_2 r^2 + \beta_1} \right)^{\frac{\beta_1}{2\beta_2 r_c^2}}}_I$$

or:

B-10

$$n(t, r) = n_0 \frac{\beta_1}{r_c} \frac{r \exp(\frac{\beta_1}{r_c^2} t)}{\beta_2 r^2 + \beta_1} \underbrace{\left( \frac{\frac{\beta_2 r_c^2}{\beta_1} + 1}{\frac{\beta_2 r^2}{\beta_1} + 1} \right)^{\frac{\beta_1}{2\beta_2 r_c^2}}}_I$$

Now the term  $I$  in Eq. (B-10) approaches one since:  $\frac{\beta_2 r_c^2}{\beta_1}$  and  $\frac{\beta_2 r^2}{\beta_1} \ll 1$ .

Therefore the approximated final form of the hydrate size distribution function due to mass transfer and hydrate reaction would be:

$$n(t, r) = n_0 \frac{\beta_1}{r_c} \frac{r \exp(\frac{\beta_1}{r_c^2} t)}{\beta_2 r^2 + \beta_1} \quad \text{B-11}$$

Introducing the Fourier number  $Fo = \frac{\beta_1 t}{r_c^2}$ , and the reduced radius  $r^* = \frac{r}{r_c}$ ,

$$n(t, r) = n_0 \frac{\beta_1}{\beta_2 r_c^2} \frac{r^* \exp(Fo)}{(r^{*2} + \beta_1 / \beta_2 r_c^2)} \quad \text{B-12}$$

Define a dimensionless parameter  $n^* \approx \frac{n}{n_0}$ ,

$$n^*(Fo, r^*) = \frac{\beta_1}{\beta_2 r_c^2} \frac{r^* \exp(Fo)}{(r^{*2} + \beta_1 / \beta_2 r_c^2)}$$

B-13

## Appendix-C

### Calculation procedure of temperature after the orifice

The target of the following analysis is the temperature at orifice exit ( $T_2$ ), Fig.(C1).

- Determining actual mass flow:

Using the ideal gas relation:

$$Q_a = Q_{st} \left( \frac{P_{st}}{P_{ex}} \right) \left( \frac{T_{ex}}{T_{st}} \right) \quad \text{C-1}$$

$$\rho_{ex} = \left( \frac{P_{ex}}{RT_{ex}} \right) \quad \text{C-2}$$

$$\dot{m}_a = \rho_{ex} Q_a \quad \text{C-3}$$

Where:

$\dot{m}_a$ : Actual mass flow (kg/s);  $Q_a$  actual volume flow rate;  $\rho_{ex}$ : density at system exit;  $R$  gas constant

- Stagnation properties:

From mass flow rate, the velocity at orifice inlet ( $V_1$ ), Point 1 in Figure C1, can be determined as follows:

$$\rho_1 = \left( \frac{P_1}{RT_1} \right) \quad \text{C-4}$$

$$V_1 = \left( \frac{\dot{m}_a}{\rho_1 A_1} \right) \quad \text{C-5}$$

Then stagnation pressure and temperature at Point 1 can be calculated using:

$$T_{01} = T_1 + \frac{V_1^2}{2C_p} \quad \text{C-6}$$

$$P_{01} = P_1 + \frac{\rho_1 V_1^2}{2} \quad \text{C-7}$$

- Assuming adiabatic reversible process through the orifice, the mass flow rate formula listed below was used to find out the pressure at Point 2 (John and Keith, 2006)

$$\dot{m}_a = \frac{\sqrt{\frac{2\gamma}{RT_0(\gamma-1)} \left(\frac{P_2}{P_0}\right)^{2/\gamma} \left[ \left(\frac{P_0}{P_2}\right)^{(\gamma-1)/\gamma} - 1 \right]}}{1 + \frac{2}{\pi} \left(\frac{P_2}{P_0}\right)^{1/\gamma}} P_0 A_f \quad \text{C-8}$$

Where,  $P_0 = P_{01} = P_{02}$ ;  $T_0 = T_{01} = T_{02}$ ;  $\gamma$ : specific heat ratio; and  $A_f$ : orifice area

The Newton-Raphson method can be used in calculating the pressure at the orifice exit.

- The orifice exit temperature now can be found using the isotropic formula:

$$T_2 = T_1 \left(\frac{P_2}{P_1}\right)^{(\gamma-1)/\gamma} \quad \text{C-9}$$

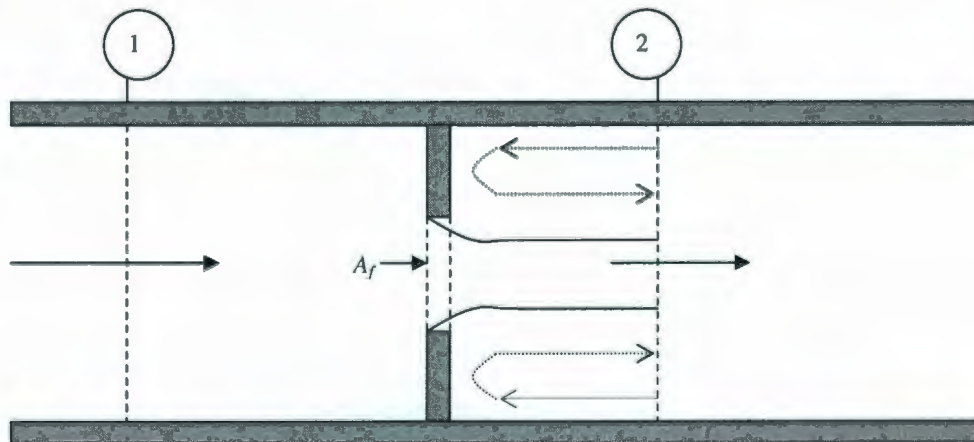


**Figure C1.** Flow through an orifice Plate

## Appendix-D

### Running typical FLUENT simulation

#### D1 Design the system using GAMBIT

Gambit is AutoCAD-like software since it uses vertices, lines, shapes, and volumes to build any complex structure. The following steps have been used to construct our system.

##### D1.1 Constructing the System in GAMBIT

- Vertices are first appointed
- Using **LINE** icon, lines are generated and the shape should be enclosed.
- By selecting all the lines, the system has to define as a surface using **FACE** icon.

##### D1.2 Mesh the Face

- In the **Mesh edges** Select the edge and click apply
- In the **Mesh Faces** form, select the face for **Faces** and Tri for **Elements**.
- Retain the default values for the other parameters and lick **Apply**.

##### D1.3 Identify the boundaries

- Select the boundary
- Define the boundary using define form

##### D1.4 Save the file

- Select **Export** in the **File** menu
- Save the file as **mesh** extension

#### D2 Simulation in FLUENT

The file is ready now to handle by FLUENT software. Start the 2D version in FLUENT then follow the following steps

##### D2.1 Grid

- Read the grid file "name.msh"
- Check the grid for confirming non-negative cell area
- To ensure the best possible grid quality for the calculation, it is good practice to smooth a triangular grid after reading it into FLUENT by using **Smooth/Swap** icon.
- Scale the grid using **Units Conversion** then click **Change Length Units**.

##### D2.2 Models

- In the **Solver**, select **Coupled** and keep the rest default.
- Turn on the standard  $k-\epsilon$  turbulence model and keep the default standard model by clicking **OK**
- Enable heat transfer by activating the energy equation.

### D2.3 Materials

- Define water vapour from the material database so that it can be used as a secondary phase.

### D2.4 Phases

- Specify air as a primary phase and click the Set... button
- In the Primary Phase Panel, select air from the Phase Material drop down list.
- Specify water-vapour as a secondary phase using same procedure of the primary phase.

### D2.5 Boundary Condition

- The boundary conditions for typical saturated air case are listed in table (D1), which represent the measuring data gained from the experiment conditions.

Table (D1) Boundary conditions (saturated air) simulation

	Parameter	Value	Unit	
Inlet	Pressure	$8.96 \times 10^4$	Pa	gauge
	total temperature	273	K	
Exit	Pressure	$2.35 \times 10^3$	Pa	gauge
	Total temperature	300	K	
Lateral Wall	temperature	270		Isothermal

## Appendix-E

### Calculation of parameters in table (8.3)

$$n_v = \frac{P}{RT} = \frac{150}{8.314 \times 272} = 0.067 \text{ kg-mole/m}^3$$

#### Diffusion Coefficient (Eq. 4.12)

Critical temperature and pressure for:

Air: 133K; 39 atm

Water: 647.1K; 217.75 atm

$$D_{AB} = \frac{3.64 \times 10^{-4}}{1.5} \times \left( \frac{272}{\sqrt{133 \times 647.1}} \right)^{2.334} \times (39 \times 217.75)^{1/3} \times (133 \times 647.1)^{5/12} \times \left( \frac{1}{29} + \frac{1}{18} \right)^{1/2}$$

$$D_{AB} = 0.16366 \text{ cm}^2/\text{s}$$

**Sherwood Number:** assumed to be  $Sh = 2.0$

#### Equilibrium water content ( $y_{eq}$ ):

Using the diagram (E1), the water content at 0C and 1.5 bar is:  $-0.002 \text{ kg/m}^3$  air. The water content in molar unit can be calculated as follows:

1 gr-mole of a gas = 22.4 L at atmospheric pressure and 0C temperature

$$y_{eq} = \frac{0.002 \times 10^3 \times 22.4 \times 10^{-3}}{18} = 2.49 \times 10^{-3} \text{ gr-mole of water/gr-air}$$

#### Saturation Ratio ( $S$ ) and actual molar fraction ( $y$ ):

From Eq. 4.9:

$$S = 1 + \frac{46.7 \times 10^{-3} \times 1}{8.314 \times 272^2} = 1.076$$

and Eq. 4.8:

$$y = 2.68 \times 10^{-3} \text{ gr-mole of water/gr-air}$$

#### Critical radius ( $r_c$ ):

The range of flow temperature inside the orifice is 235-272K. Based on that the range of the critical radius would be:

$$r_c = \frac{2 \times 0.033}{1000 \times \frac{8314}{29} \times T \times \ln(1.076)} = (11.5 - 13.37) \text{ nm}$$

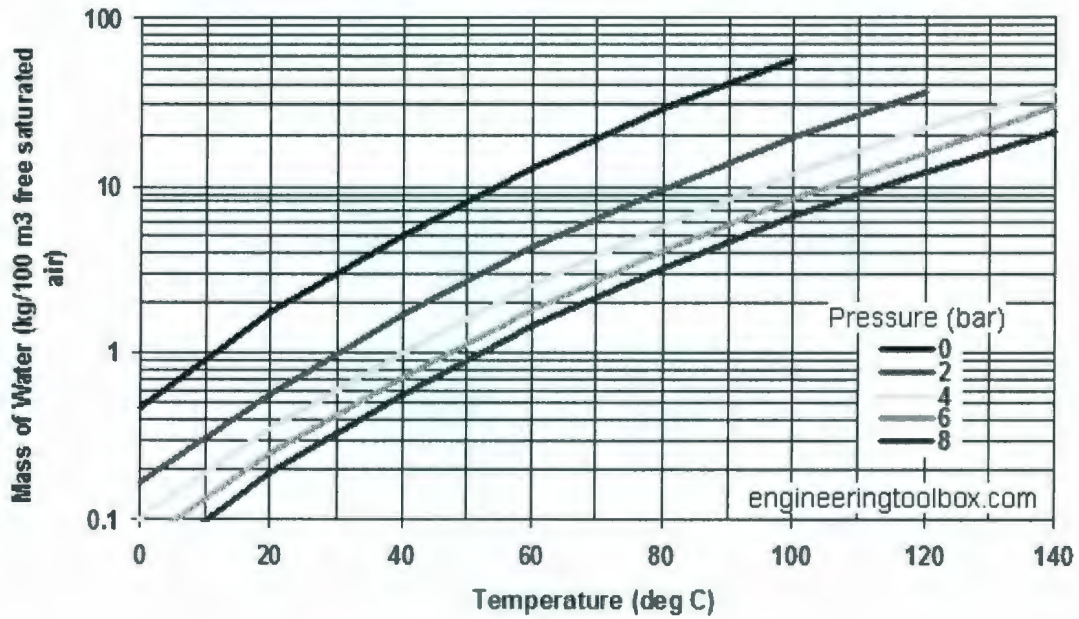


Figure (E1) water content of saturated air

## Appendix-F

### Typical calculation of deposition distance

Assume a hydrate particle with diameter  $50\mu\text{m}$  moves in a gas flow. According to the CFD simulation results,  $U_g \sim 14.4\text{ m/s}$  at the centerline. Hence  $Re = 14\,500$  for  $D_{\text{pipe}} = 19.05\text{ mm}$ .

The deposition velocity, using the model of Friedlander and Wells, would be:

$$V_d = 1.247 \times 10^{-2} \text{ m/s}$$

The elapsed time for this particle to reach the wall is:

$$t = \frac{Y_l}{V_d} = 0.764 \text{ s}$$

Within this time, the hydrate particle grows from the original size  $r_{p0} = 25\mu\text{m}$  to a new size  $r_p$ . According to the solution of Eq. 4.17, the correlation of particle radius as a function of time becomes:

$$r_p^n = \sqrt{e^{2\beta_2 t} r_{p0}^2 + \frac{\beta_1}{\beta_2} (e^{2\beta_2 t} - 1)}$$

For  $\beta_1 = 3.19 \times 10^{-13} \text{ m}^2/\text{s}$ ;  $\beta_2 = 3.7 \times 10^{-6} \text{ s}^{-1}$ ; and  $t = 0.764 \text{ s}$ , the new size of the particle would be:

$$d_p = 50.02 \mu\text{m}$$

Now, launching from rest, the particle velocity can be determined using the following formula, which analytically derived from the equation of motion (Jassim *et al.*, 2008):

$$u_p = (U_g - g\tau_v) \times (1 - e^{-t/\tau_v}) = 14.39 \text{ m/s}$$

The deposition distance  $X_l$  would be:

$$X_l = u_p \times t = 11 \text{ m}$$

The particle reaches the wall region. Thus, the code will direct the process of the particle motion near the wall based on the comparison of the particle diameter with the boundary layer thickness.

$$\delta = 14.1 \times \frac{D_{\text{pipe}}}{Re \times \sqrt{f}} \approx 105 \mu\text{m}$$

As:  $d_p < \delta$ , the particle will merge into the boundary layer and the balance of the forces applied to the particle will track the trajectory of the particle. Hence, the code will evaluate all the external forces, which are lift, drag, adhesive and gravity forces.

Using the correlations 6.25 to 6.29, the magnitude of the forces would be:

Force	Value in (nano-Newton)
Lift	12.12
Adhesive	$6.6 \times 10^{-9}$
Drag	44.26
Gravity	0.6

$$F_{net} = \text{Lift} - (\text{Adhesive} + \text{Gravity}) = 11.5 \text{ (nN)}$$

Since the net force applied on the particle is positive, the particle will entrain at this moment with an angle:

$$\theta = \tan^{-1} \left( \frac{F_{net}}{F_{Drag}} \right) = 14.56^\circ$$

The extended distance due to this process will be:

$$X_2 = X_{2(0)} + Y_0 / \tan(\theta),$$

$$\text{Where : } X_{2(0)} = \begin{cases} 0 \\ X_2 \end{cases} \quad \text{and} \quad \begin{cases} Y_0 = \delta \\ Y_0 = Y \end{cases} \quad \text{for } \begin{cases} t = 0 \\ t > 0 \end{cases}$$

$$X_2 = 0 + 105 \times 10^{-6} / \tan(14.56) = 4.04 \times 10^{-4} \text{ m},$$

Repeating the steps in the boundary layer region and for each step,  $X_2$  should be estimated till  $Y \leq 0$ , which at this point the particle attached the wall.

## Appendix G

### List of research papers

Papers published in peer-review journal, refereed conferences and non-refereed conferences are listed below:

#### CFD Application

1. **Jassim E.**, Abedinzadegan Abdi M., and Muzychka Y., "Computational Fluid Dynamics Study for Flow of Natural Gas through High Pressure Supersonic Nozzles: Part 1- Real Gas Effects and Shockwave", *Journal of Petroleum Science and Technology*, 26(15), 1757-1772.
2. **Jassim E.**, Abedinzadegan Abdi M., and Muzychka Y., "Computational Fluid Dynamics Study for Flow of Natural Gas through High Pressure Supersonic Nozzles: Part 2- Nozzle Geometry and Vorticity", *Journal of Petroleum Science and Technology*, 26(15), 1773-1785.
3. **Jassim, E.**, Abdi M., and Muzychka Y., "Simulation of Natural Gas Flow through Complex Geometries Using Computational Fluid Dynamics", the *International Oil and Gas CFD Conference (IOCC)*, London, UK, 30 November – 1 December, 2006.
4. **Jassim, E.**, Abdi M., and Muzychka Y., "Thermal Effects of Cold Jet on Pressure Vessels and Surrounding Equipment", proceedings of the *2006 International Marine CNG Standard Forum*, St. John's, NL, Canada, November 7-9, 2006.

#### Nucleation and Hydrate growth

1. **Esam Jassim**, Abedinzadegan Abdi M., and Muzychka Y., "Modeling Hydrate Nucleation and Growth and Predicting Particles Size Distribution in Gas Flow Regimes", Submitted to the *Journal of Canadian Petroleum Technology*, Jan. 2008.
2. **Esam Jassim**, Abedinzadegan Abdi M., and Muzychka Y., "Nucleation and Accumulation Phenomena of Hydrate in Oil and Gas Pipelines", proceedings in the 1<sup>st</sup> Saudi Arabia Oil and Gas Exhibition (SAOGE), Damman, Saudi Arabia, Nov. 15-17, 2008.

#### Deposition

1. **Jassim E.**, Abedinzadegan Abdi M., and Muzychka Y., "Model Predicts Hydrate Deposition Location", *Exploration and Production – The Oil and Gas Review, OTC Edition*, 6(1), 112-113, 2008.
2. **Jassim, E.**, Abdi M., and Muzychka Y., "Locating Hydrate Deposition in Multiphase Compressed Natural Gas Flow Lines", proceedings of the *2007 International Marine CNG Standard Forum*, St. John's, NL, Canada October 30-31, 2007.
3. **Jassim E.**, Abedinzadegan Abdi M., Muzychka Y., "A CFD-Based Model to Locate Flow Restriction Induced Hydrate Deposition in Pipelines", proceedings in the *2008 Offshore Technology Conference, OTC 08*, Houston, USA, May 5-8, 2008.

## Appendix H

```
*****
*****
*   THIS PROGRAM IS CREATED FOR MODELLING THE DEPOSITION PHENOMENA OF FLUID/PARTICLE MOTION. IT
*   CONSISTS OF NUCLEATION AND GROWTH MODELS,
*   DEPOSITION EFFECIENCY AND AMOUNT OF PARTICLE DEPOSIT IN FULLY TURBULENT REGIME, SUBLAYER
*   FORCE BALANCE AND BROWANAIN MOTION
*****
```

```
*****
C      S          SATURATION RATIO
C      Rv         SPECIFIC GAS CONSTANT
C      NUE       KINEMATIC VISCOSITY OF GAS
C      Rp        RAIDUS OF PARTICLE
C      RC        CRITICAL RAIDUS
C      SQMA      SURFACE TENSION          (0.02 N/m)
C      ROWL      DENSITY OF WATER (1000 kg/m3)
C      ROWP      DENSITY OF HYDRATE PARTICLE (960 kg/m3)
C      MWA,MWB   Molecular weight of water and Gas
C      MUE       Dynamic VISCOSITY OF GAS
C      Vr        RELATIVE VELOCITY (Vp-Vg)
C      TCA       CRITICAL TEMPERATURE OF SUBSTANCE A
C      TCB       CRITICAL TEMPERATURE OF SUBSTANCE B
C      PCA       CRITICAL PRESSURE OF SUBSTANCE A
C      PCB       CRITICAL PRESSURE OF SUBSTANCE B
C      P         PRESSURE (atm)
C      T         TEMPERATURE (K)
C      Ug        AVERAGE GAS VELOCITY (m/s)
C      KB        BOLTZMAN CONSTANT
```

```
REAL L,MUE,MWA,MWB,NUE,KB,Rn(1000000)
OPEN(33,FILE='DATA')
OPEN(2,FILE='PARTICLEDIA')
OPEN(3,FILE='PARTICLEDIFF')
OPEN(4,FILE='DEPOSITION')
OPEN(5,FILE='ANGLE')
OPEN(6,FILE='FORCE')
OPEN(7,FILE='POSITION')
OPEN(8,FILE='BOUNDARY-LAYER')
OPEN(9,FILE='BOUNCING')
PI=3.1428
Rv=8314/44
f=0.02804
61  READ(33,61)
    FORMAT(/,/,/,/,/,/,/,/,/,/,/,/,/,/,/,/,/)
    READ(33,*)SQMA,ROWL,ROWP,MWA,MWB,MUE,Vr
    READ(33,*)TCA,TCB,PCA,PCB,T,P,Ug,KB
    READ(33,*)Dpipe,L
    Yi=0.5*Dpipe
    Pa=P*101.325
    S=1+(13.26e3*(276-T)/(8.314*T*T))

    YEQ=160e-3*0.2367/MWB
    RC=2*SQMA/(ROWL*Rv*T*LOG(S))
    Rp=RC
    ROWG=Pa*MWA/(T*8.314)

    NUE=MUE/ROWG
    CALL FLOW(f,Dpipe,Ug,NUE,BL,Usub,SRV,RE)
    CALL OUTPUT1(Dpipe,Ug,f,RE,Usub,BL)
        Rp=25.0e-6

C      CALL NUCL(Pa,T,S,DRDTNUC)
time=0.0
    NTIME=1000

    TOTALN=1
```

```

Y=BL
hm=Y
REp=2*Rp*Vr/NUE
CALL DIFFCOF(TCA,TCB,PCA,PCB,T,P,MWA,MWB,Diff)

```

```
DO 10 I=1,NTIME
```

```
CALL SHROOD(REp,NUE,Diff,Sh)
```

```
CALL PENT(f,Dpipe,2*Rp,L,ROWP,ROWG,MUE,T,Usub,Ug,Vdr,Us,Cc,tau)
```

```
CALL MODELS(K,ROWP/ROWG,Usub,NUE,Diff,2*Rp,tau,Re,Vpln)
```

```
Vd=Vpln*Usub
```

```
time=Yi/Vd
```

```
+ CALL GROWTH(SQMA,ROWG,ROWL,ROWP,MWA,MWB,S,YEQ,
KB,T,Pa,RC,Rp,Sh,D,time,Rn(I),DRDTM,DRDTR,DRDT,DNDT)
```

```
uy=Ug-2.5*Usub*ALOG(0.5*Dpipe/Yi)
```

```
uyp=(uy-9.81*tau)*(1-exp(-time/tau))
```

```
X1=uyp*Yi/Vd
```

```
write(*,*)X1,uyp,time,Vpln,Vd,2*Rp,4*Rp*Rp*Cc*ROWP/(18*MUE)
```

```
pause
```

```
Pmass=4*PI*ROWP*Rp**3/3
```

```
c IF(2*Rp.GE.BL)THEN
WRITE(*,*)BL*1E6,2E6*Rp,Us
```

```
CALL BOUNCEF(1,2*Rp,ROWG,Ug,Vd,pmass)
```

```
GO TO 20
```

```
ENDIF
```

```
CALL DEPO(I,TOTALN,time,Dpipe,BL,Vd,DEPN,DEPNT)
```

```
IF(hm.GE.BL)THEN
```

```
hm=BL
```

```
ELSE
```

```
hm=BL-Y
```

```
ENDIF
```

```
c SRV=SRV*Y/BL
IF(SRV.GE.1E-15)THEN
```

```
ENDIF
```

```
+ CALL FORCES(J,Cc,ROWG,ROWP,MUE,2*Rp,SRV,Ug,hm,BL,FL,
Fg,Fwall,FDy,Fbalance)
```

```
CALL DRAG(2*Rp,MUE,SRV*Ug,Cc,FD)
```

```
THETA=ATAN(Fbalance/FD)*180/PI
```

```
CALL BLAYER(I,J,BL,THETA,Us,Rp,time,X,Y)
```

```
c write(*,*)'X1=',X1,X1+X,Y,2e6*Rp
PAUSE
```

```
20 CALL OUTPUT2(2*Rp,time,X,Y,BL,DEPN,DEPNT,TOTALN,THETA,FL,
+ Fg,Fwall,FDy,FD,Fbalance,PB)
```

```
10 CONTINUE
```

```
write(*,*)'end'
```

```
STOP
```

```
END
```

```

SUBROUTINE BOUNCEF(I,Dp,ROWG,Ug,Ub,pmass)

write(15,*)'-----I=',I,'----Dp=',Dp*1e6,'-----'
XX=0
tt=0
nb=0
V1p=Ub
st=(926+0.5*ROWG)*Ug*Dp/(9*1.027e-5)

ep=0.91*exp(-35/st)
Energy=4.8647e-20*Dp/(12*4e-10)

V1c=SQRT((2*Energy/pmass)*(1-ep*ep)/(ep*ep))
23 if(V1p.le.V1c)then
  write(*,*)'Particle adhere'

  Return
else
  write(*,*)'Particle rebound'
  V2p=V1p*SQRT(ep*ep-(2*Energy*(1-ep*ep)/(pmass*V1p*V1p)))

  nb=nb+1
  VR=V1p/V2p
  sinphi=SQRT(ABS(1-(VR*ep)**2)/(VR*VR*(1-ep*ep)))
  phi1=ASIN(sinphi)
  IF(sinphi*VR.LE.1)then
    phi2=ASIN(VR*sinphi)
  else
    phi2=3.14*0.5
  write(*,*)'nb=',nb,V1p,V2p,phi1*180/3.1,phi2*180/3.14
  write(*,*)'Particle adhere'

  stop
  Return
endif

c write(*,*)'nb=',nb,ep,V1p,V2p,phi1*180/3.1,phi2*180/3.14
V1p=V2p
YY=(V2p*COS(phi2))**2/(2*9.81)
tt=V2p*COS(phi2)/9.81+tt
XX=V2p*SIN(phi2)**2*tt+XX
write(15,*)nb,tt,XX,YY

c pause
go to 23
endif
RETURN
END

```

```

SUBROUTINE DIFFCOF(TCA,TCB,PCA,PCB,T,P,MWA,MWB,DAB)

C TCA,TCB CRITICAL TEMP.OF GASES A&B [K]
C PCA, PCB CRITICAL PRESS.OF GASES A&B [atm]
C P SYSTEM PRESSURE [atm]
C a,b DIMENSIONLESS CONST.(a=3.640E-4; b=2.334)
C MWA,MWBM MOLECULER WEIGHT OF SUBSTANCE A&B

REAL MWA,MWB
a=3.64e-04
b=2.334

TERM1=(T/SQRT(TCA*TCB))**b
TERM2=SQRT(((1/MWA)+(1/MWB)))
TERM3=(PCA*PCB)**(1/3.0)
TERM4=(TCA*TCB)**(5/12.0)

DAB=a*TERM1*TERM2*TERM3*TERM4/P
C write(*,*)TERM1,TERM2,TERM3,TERM4,P,T,DAB
C PAUSE

```

RETURN  
END

SUBROUTINE FLOW(f,Dpipe,Ug,VISKO,BL,Usub,SRV,Reg)

Reg=Ug\*Dpipe/VISKO  
BL=14.1\*Dpipe/(Reg\*SQRT(f))  
Usub=5\*VISKO/BL  
SRV=Usub/Ug  
write(\*,\*)Reg,BL,Ug,Usub  
pause  
RETURN

END

+ SUBROUTINE GROWTH(SQMA,ROWG,ROWL,ROWP,MWA,MWB,S,YEQ,KB,T,Pa  
,RC,Rp,Sh,DAB,time,Rpn,DRDTM,DRDTR,DRDT,DNDT)

REAL Mv,Nv,MWA,MWB,KB,LNPEQ  
PI=3.14159  
AVOGADRO=6.022E+23

Nv=ROWG/MWA  
Mv=MWB/AVOGADRO

Y=S\*YEQ  
TAU=SQMA\*(36\*PI)\*\*(0.333)\*(Mv/ROWL)\*\*(0.66667)/(KB\*T)  
TERMM=4\*TAU\*TAU\*TAU/(27\*LOG(S)\*LOG(S))

BETA1=0.5\*(Nv/ROWL)\*(Sh\*DAB\*1E-4\*MWA)\*(Y-YEQ)  
Rpmass=SQRT(2\*BETA1\*time+RC\*RC)  
c DNDT=(1/S)\*(Mv/ROWL)\*SQRT(2\*SQMA/(Mv\*PI))\*(ROWG/Mv)\*\*2\*  
c + EXP(TAU-TERMM)

C REACTION KINETIC COEFFECIENT-----

LNPEQ=0.116\*T-30.778  
PEQ=1E6\*EXP(LNPEQ)  
FUGEQ=(1-Y)\*PEQ  
FUG=1E3\*(1-Y)\*Pa

BETA2=0.5875E-11\*3.75E5\*MWA\*(FUG-FUGEQ)/(3000\*ROWP)

C GROWTH RATE  
DRDTM=BETA1/Rp  
DRDTR=BETA2\*Rp  
DRDT=DRDTM+DRDTR

Rpn=SQRT(EXP(2\*BETA2\*time)\*(RC\*RC+(BETA1/BETA2))-(BETA1/BETA2))

c  
108 write(2,108)time,2\*Rpmass\*1e6,2\*Rpn\*1e6,DRDT  
FORMAT(2X,(4E12.4,2X))

RETURN  
END

SUBROUTINE NUCL(Pa,T,S,DRDTNUC)

A=7.262E-21  
DELTAH=13.26E3  
DELTAT=8.314\*(S-1)\*T\*DELTAH  
DT=(DELTAT)\*\*2.411

DRDTNUC=A\*EXP(-106.20E3/(8.314\*T))\*EXP(-0.0778/DT)\*

```

+ (Pa/1E3)**2.986
WRITE(*,*)DELTAT,DT,T,DRDTNUC
PAUSE

RETURN
END

+ SUBROUTINE PENT(f,D,Dp,L,ROWP,ROWG,VISGAS,T,Usub,Ug,Vdr,
  Us,Cc,TAUV)
  REAL lambda,L,NUE
  lambda=48E-9
  SR=ROWP/ROWG
  Re=ROWG*Ug*D/VISGAS
  NUE=VISGAS/ROWG
C   WRITE(12,*) Dp Cc us DIFF Scp
C +RELAX. Time'

  CALL SLIPCORR(lambda,Dp,Cc)

  CALL SETTLEVELOC(ROWP,Dp,VISGAS,Cc,Us)

  CALL DIFFPART(T,Dp,Cc,VISGAS,DIFFP)

  CALL SCPARTICLE(ROWG,VISGAS,DIFFP,SCP)

  CALL RELAXATION(ROWP,Dp,VISGAS,Cc,RTIME)
  WRITE(3,15)Dp*1.0E6,Cc,Us,DIFFP,SCP,RTIME
15  FORMAT(2x,F8.3,2X,F7.3,2X,4(E9.4,2X))

C*****
C   ----ESTIMATING DEPOSITION VELOCITY RATIO-----
C*****
  SL=ROWG*ROWP*Ug*Ug*(f/2)*Dp*Dp/(18*VISGAS*VISGAS)
  TAUV=SR*Dp*Dp*Usub*Usub/Cc/(18*NUE*NUE)

  IF(TAUV.LE.0.3)THEN
C   WRITE(*,*)SCP,Re,'DIFFUSION'
  Vdr=0.039*SCP**(-0.667)*Re**(-0.25)

  ELSEIF(SL.LT.5.0)THEN
  DEMO=SQRT(f/2)*(1525/(SL*SL)-50.6)
  Vdr=(Ug/Usub)*0.5*f/(1+DEMO)
  ELSEIF(SL.GT.30)THEN
  Vdr=0.5*f*(Ug/Usub)

  ELSE
  DEMO=SQRT(f/2)*(5*ALOG(5.04/((SL/5)-0.959))+13.73)
  Vdr=(Ug/Usub)*0.5*f/(1+DEMO)

  ENDIF

  fp=EXP(-4*Vdr*Usub*L/(Ug*D))
  fc=1-fp
C   WRITE(13,*)Dp*1E6,DEMO,Vdr,TAUV
  WRITE(14,*)Dp*1E6,TAUV,fc*100
c   pause
  RETURN
  END

SUBROUTINE SLIPCORR(lambda,Dp,Cc)
  REAL lambda
  Cc=1+(lambda/Dp)*(1.05*EXP(-0.39*lambda/Dp)+2.34)

  RETURN
  END

```

```

SUBROUTINE SETTLELOC(ROWP,Dp,VISGAS,Cc,Us)
GRAV=9.81
Us=ROWP*Dp*Dp*GRAV*Cc/(18*VISGAS)

RETURN
END

SUBROUTINE DIFFPART(T,Dp,Cc,VISGAS,DIFFP)
BOLTZ=1.381E-23
PI=3.14159
DIFFP=BOLTZ*T*Cc/(3*PI*VISGAS*Dp)

RETURN
END

SUBROUTINE SCPARTICLE(ROWG,VISGAS,DIFFP,SCP)
SCP=VISGAS/(ROWG*DIFFP)

RETURN
END

SUBROUTINE RELAXATION(ROWP,Dp,VISGAS,Cc,RTIME)
RTIME=ROWP*Dp*Dp*Cc/(18*VISGAS)

RETURN
END

SUBROUTINE DEPO(I,TOTALN,time,Dpipe,BL,Vd,DEPN,DEPNT)
IF(I.LE.2)THEN
CT=time
ENDIF

DEPN=TOTALN*(1-EXP(-2*Vd*(CT)/(Dpipe-BL)))
DEPNT=DEPNT+DEPN
TOTALN=TOTALN-DEPN

RETURN
END

SUBROUTINE SHROOD(REp,NUE,D,Sh)
REAL NUE

Sc=NUE/D
Sh=2.009+0.514*SQRT(REp)*Sc**(1/3)

RETURN
END

SUBROUTINE FORCES(J,Cc,ROWG,ROWP,VISGAS,Dp,SRV,Ug,hh,BL,FLCA,
+ Fg,Fwall,FD1,Fbalance)
REAL hh,rp

```

```

A=4.59c-12

VISK=VISGAS/ROWG
C hh=Dp/2+100e-6
c hh=163e-6
IF(hh.LE.Dp/2)THEN
WRITE(*,*)'ATTACHED TO WALL'
STOP
ENDIF
rp=Dp/2

CALL DRAG(Dp,VISGAS,SRV*Ug,Cc,FD1)
CALL LIFTFORCE(Dp,hh,ROWG,VISK,SRV,Ug,Fplus,BL,FLC)

CALL ADHESIONWALL(A,hh*1e9,rp*1e9,Fwall)

CALL GRAVITY(ROWP,Dp,Fg)
FLCA=FLC*(1-J)
Fbalance=FLC*(1-J)-Fwall-Fg
c WRITE(*,*)Dp*1e6,FLC*1E9,Fwall*1E9,Fg*1E9
c WRITE(*,*)(hh-Dp/2)*1E6,FLC*1E9,Fbalance*1E9

C PAUSE

RETURN
END

SUBROUTINE LIFTFORCE(Dp,h,ROWG,VISK,SRV,Ug,Fplus,delta,FLC)

Dplus=Dp*(0.06*Ug)/VISK

IF(Dplus.LT.0.15)THEN
Fplus=0.567*Dplus
ELSEIF(Dplus.LT.1.5)THEN
Fplus=15.57*(Dplus)**1.87
ELSE
Fplus=4.21*(Dplus)**2.31
ENDIF

CALL LIFTC(Dp,h,ROWG,VISK,SRV,Ug,delta,FLC)
FL=ROWG*VISK*VISK*Fplus
C WRITE(*,*)'LIFT',Dp*1E6,FL,FLC
C PAUSE
RETURN
END

SUBROUTINE LIFTC(Dp,h,ROWG,VISK,SRV,Ug,delta,FLC)

Vr=(0.9*SRV*Ug-SRV*Ug)*h/delta
HR=Dp/(2*h)
S=Dp*(SRV*Ug)**2/(2*VISK*Vr)
AI=1.7716+0.216*HR-0.7292*HR*HR+0.4854*HR**3
+ -(3.2397/HR+1.145+2.084*HR-0.9059*HR*HR)*S
+ +(2.0069+1.0575*HR-2.4007*HR*HR+1.3174*HR**3)*S*S
FLC=ROWG*Vr*Vr*Dp*Dp*AI/4
RETURN
END

SUBROUTINE GRAVITY(ROWP,Dp,Fg)
PI=3.1416
Fg=9.81*PI*ROWP*Dp**3/6
RETURN
END

```

```
SUBROUTINE ADHESIONWALL(A,h,r,Fwall)
```

```
CALL F0WALL(h,r,F0)
```

```
CALL F1WALL(h,r,F1)
```

```
Fwall=ABS(A*(F0+0*F1))
```

```
RETURN
```

```
END
```

```
SUBROUTINE F0WALL(h,r,F0)
```

```
F0=(2/(3*r))*(1/((h/r)**2-1))
```

```
RETURN
```

```
END
```

```
SUBROUTINE F1WALL(h,r,F1)
```

```
b=3.1
```

```
ambdaw=100
```

```
PI=3.1416
```

```
c=-b*ambdaw/(2*PI)
```

```
TERM1=2*(h+c-2*r)*(h+c+r)**2*ALOG(abs(h+r+c))/(3*c**4)
```

```
TERM2=2*(h+c+2*r)*(h+c-r)**2*ALOG(abs(h-r+c))/(3*c**4)
```

```
TERM3=(2*(h+2*r)*(h-r)**2/(3*c**4)  
+ (2*(h+r)*(h-r)/c**3)+(2*h/c**2)+2/(3*c)
```

```
TERM4=(2*(h-2*r)*(h+r)**2/(3*c**4)  
+ (2*(h-r)*(h+r)/c**3)+(2*h/c**2)+2/(3*c)
```

```
TERM5=4*h*r/(3*c**3)+(8*r/(3*c*c))+(4*h*r/(3*c*(h-r)*(h+r)))
```

```
F1=-TERM1+TERM2-TERM3*ALOG(h-r)+TERM4*ALOG(h+r)-TERM5
```

```
RETURN
```

```
END
```

```
SUBROUTINE DRAG(Dp,VISGAS,Up,Cc,FDD)
```

```
PI=3.1416
```

```
FDD=3*PI*Dp*VISGAS*Up/Cc
```

```
RETURN
```

```
END
```

```
SUBROUTINE BLAYER(I,J,BL,THETA,Us,Rp,time,X,Y)
```

```
PI=3.1428
```

```
IF(THETA.LE.0)THEN
```

```
Y=Y-Us*time/(I-1)
```

```
IF(Y.LE.0)THEN
```

```
WRITE(*,*)2*Rp*1e6,'PARTICLE DEPOSIT'
```

```
Y=BL
```

```
STOP
```

```
ELSE
```

```
X=X+Y/ABS(TAN(THETA*PI/180))
```

```
J=0
```

```
ENDIF
```

```
ELSE
```

```
Y=Y+Us*time/(I-1)
```

```
IF(Y.GT.BL)THEN
```

```
WRITE(*,*)2*Rp,'ENTRAIN'
```

```
J=1
```

```
Y=BL
```

```
STOP
```

```
ELSE
```

```
C
```

```

X=X+Y/ABS(TAN(THETA*PI/180))
J=0
ENDIF
ENDIF

RETURN
END

SUBROUTINE MODELS(K,SR,Usub,NUE,DIFF,Dp,tau,Re,Vpln)
REAL L1,K,NUE,kpl
PI=3.1415926

dpl=Dp*Usub/NUE
kpl=K*Usub/NUE
gpl=9.81*NUE/(Usub**3)

L1=3.08/(SR*dpl)

Sc=NUE/DIFF
term1=1+8*exp(-(tau-10)**2/32)
term2=abs(1-tau*tau*L1)
Vpl1=0.5*((0.64*kpl+0.5*dpl)**2/3.42)**(1/(1+L1*tau*tau))
+
*0.037*(term1/term2)+tau*gpl+0.084*Sc**(-2/3)
IF(Vpl1.GE.0.14)THEN
Vpl1=0.14
ENDIF
Vpl2=0.057*Sc**(-2/3)+4.5e-4*tau*tau+tau*gpl
Vpln=0.5*((0.64*kpl+0.5*dpl)**2/3.42)**(1/(1+L1*tau*tau))
+*0.037*(term1/term2)+tau*gpl+0.039*Sc**(-0.667)*Re**(-0.25)
IF(Vpln.GE.0.14)THEN
Vpln=0.14
ENDIF
RETURN
end

```







